Report for

International Fine Particle Research Institute

Horizons in Dry Granular Modeling: beyond DEM

Farhang Radjai

May 15, 2023

SAR-115-01

Executive Summary

Discrete Element Method (DEM) consists in solving the equations of motion of a collection of rigid particles by accounting for their contact interactions [32, 137, 60, 29, 120]. Over the last 40 years, DEM has matured into a general-purpose tool for the simulation of industry-related particulate processes and for the investigation of the complex behavior of granular materials. With rising computational power and inclusion of realistic particle characteristics, both the accuracy and the computational efficiency of DEM simulations have continuously increased, but the level of expectations of DEM has considerably grown at the same time.

This report attempts to outline the horizons of granular modeling beyond the current practice of DEM. It is not meant to be a review of DEM and its recent numerous achievements or alternative methods to DEM, but to serve as an objective description of the issues and new resources that may lead to a paradigm shift in near future. The seminal report of P. W. Cleary for IFPRI, entitled “Review of DEM for Industrial Applications", in 2010 provides a clear and rich background of DEM together with the breadth of industrial applications that are possible with DEM [29]. Despite huge progress accomplished during the last decade, most themes and issues developed and exemplified in that report about discrete modeling and its applications are still relevant. The present report may be considered as a complement to that one, with the somewhat different goal of highlighting the shortcomings of the current practice of DEM and the novel trends that can allow us to identify the most promising future developments. Several examples of coupled DEM-CFD (Computational Fluid Dynamics) simulations are cited in this report, but the focus will be on the particles and their interactions in DEM.

In section 1, we discuss the role of DEM as an original approach for gaining knowledge on particulate systems alongside theory and experiment. We argue that DEM is an inherently bottom-up approach and the adequate definition of numerical material is as much important as the mathematical algorithm used for the prediction of cooperative dynamics. We also describe the three levels of DEM with increasing complexity of the numerical material and the scope of a data-driven approach with the potential power of providing tools to improve accuracy and efficiency. We underline the interpretive use of DEM in connection with theory and the origins of its general trustworthiness in connection with experiment.

In section 2, we highlight the role of contact interactions and their implementation in DEM. The focus will be on several ambiguities and shortcomings which need to be resolved, such as normal force positivity and memory of tangential displacements. We develop the difference between force laws and contact laws and the prospect of a shift from the hard-particle soft-contact approach to a soft-particle hard-contact approach. We also consider different models of adhesion and recent models of elastoplastic contacts and discuss their applicability and consequences for granular dynamics. Finally, we focus on parametric randomness and more specifically polydisperse input parameters as a major ingredient of physics fidelity that has been so far ignored in DEM simulations.

Section 3 is devoted to the representation and implementation of particle shape with its variants as a key input of DEM. In particular, we discuss arbitrary particle shapes and their extraction from image data as a step towards data-driven DEM and the contact detection issues. We underline the role of shape polydispersity and discuss the issue of reducing particle shape to a small number of descriptors or through its effect in connection with dissipation.

In section 4 we describe different modeling strategies for particle breakage at the sub-particle and particle levels. The realism and efficiency of sub-particle methods are discussed, such as breakage criteria with regard to fracture mechanics, finite size effects, shapes of the generated fragments, and

recently developed hybrid methods. We discuss how the higher physics-fidelity of sub-particle models can be combined with the computational efficiency of particle level models.

Section 5 is devoted to DEM models of soft particles, i.e. particles undergoing large deformations without breakage. We briefly present the surface deformation methods based on material points or nodes at the particle surface, and volume deformation methods based on continuum field description of the particle behavior.

In section 6 we discuss several computational issues. The important role of parallel computing, specially on General-Purpose GPUs, for the applicability of new models of high physics fidelity and for speedup of simulations is underlined. The limits of particle coarsening are discussed. We also recall new developments in original multiscale hybrid models and the benefits of concurrent use of discrete and continuum simulations of granular materials. Finally, we discuss the ways Machine Learning models can be used with DEM simulations and a data-driven approach allowing expensive calculations of contacts, forces and velocities in DEM algorithms to be replaced by a Machine Learning-enabled framework.

In section 7 we consider the issues of verification and validation, and discuss the methods of uncertainty quantification as an asset to reinforce the reliability of DEM in application to real-world processes. We use examples of rigorous uncertainty quantification to illustrate the treatment of uncertainties related to the input data and model approximation. We also present the concept of validation metric for optimal use of experimental data for the evaluation of model form errors.

Finally, we present an outlook of future directions around and beyond DEM in section 8. Recent algorithmic developments are qualified according to their contributions to physics fidelity, data fidelity, computational efficiency, and game-changing nature. We discuss the developments beyond the hard-particle approximation and the scope of a data-driven DEM.

Contents

1 DEM: between theory and experiment

We are interested in this section in the role of discrete-element modeling with respect to theoretical modeling and experimental approach in the field of granular materials.

1.1 The three levels of DEM

Computer simulation is highly valued in science because of its essential role in the epistemic process along with theory and experiment [5]. This role is quite well appreciated in the case of granular materials. The common understanding of discrete modeling is that granular materials are composed of 'simple' grains that give rise to 'complex' behavior as a consequence of their cooperative dynamics. This is exactly what a DEM code is expected to do for us by solving the equations of dynamics for a large number of interacting particles. This viewpoint is supported by the fact that DEM simulation of a collection of spherical particles is able to reproduce major (and sometimes counter-intuitive) granular phenomena such as sandpile shapes, Janssen effect, dilatancy, inelastic collapse, size segregation, etc. This is the view that prevailed for two decades. We will refer to this level of DEM as *basic DEM*, which involves simple spherical particles and simple interactions such as elastic repulsion, Coulomb friction, and viscous damping.

Basic DEM corresponds to the hard-sphere model in physics [142]. In this respect, it can also be coined *Hard-Sphere (HS) DEM*. Despite its elementary setting, HS-DEM represents a powerful demonstration of the added value of DEM and underlies its high scientific attraction. Over the years, HS-DEM has been abundantly used to investigate packing properties, jamming transition, order-disorder transition, inertial flows, granular gases, force chains, hopper flow, fluidized beds, size segregation, pattern formation, and many industry-related granular processes. These applications have also offered opportunities for validation by comparing simulation results with the experiments carried out by using particles tailored to represent ideal spherical grains and well-controlled properties such as interparticle friction coefficient and normal restitution coefficient [12, 89, 91, 124, 76]. Experimental HS models were actually among the first to have been quantitatively and successfully compared with DEM simulations.

It is often stated that DEM is similar to the Molecular Dynamics (MD) method: Both of them are Lagrangian methods that track the particles by integrating the classical laws of motion. However, this similarity is minor compared to fundamental differences arising from the *nature of interactions*. Not only the contact interactions dissipate energy, but they also strongly constrain particle motions. For this reason, through DEM simulations we solve a problem of *constrained dynamics* or *nonsmooth dynamical system* in which the particle velocities can undergo discontinuous changes or percussions due to multicontact collisions or exchange of impulsions [96, 119, 18, 121]. In other words, in the limit of perfectly rigid particles, the velocity function is not derivable every where and therefore acceleration is not defined. 'Nonsmoothness' refers to this property, which represents an extreme nonlinearity. Hence, the contact laws are not actually 'simple' laws, but represent rather highly nonlinear interactions that are at the origin of the rich dynamic and static behaviors of granular materials even for simple particle shapes.

It is also useful to compare DEM with cellular automata (CA), which preluded lattice-based computational methods [130]. A cellular automaton is a regular grid of cells, which can be in a finite number of predefined states. An initial state is assigned to all cells and they are updated step by step according to rules that define the new state of each cell as a function of its current state and those of neighboring cells. Conway's Game of Life is an example of a 2D cellular automaton. Interestingly,

even with very simple rules, a cellular automaton generates complex features such as long-lived dynamical structures and amazingly rich cyclic patterns. This implies that discrete systems governed by simple rules can generate complex phenomena. CA has also been applied to model granular flows [10]. There is, however, an essential difference between DEM and CA: the cells on a grid do not move whereas particles move. We still can conceive a cellular automaton in which each particle is attributed to a cell and the states are the particle positions and velocities. These states change in each time step according to Newton-Euler's laws of motion and force laws. The criterion for two cells to be neighbors is the presence of a geometrical contact between their corresponding particles. Therefore, the neighboring cells on the grid do not necessarily correspond to neighboring particles in physical space. This is a fundamental difference between lattice-based methods and DEM.

We may also compare DEM with continuum models. DEM is a Lagrangian *object-based* method in which the mass centers of the particles carry vectorial information (positions and velocities). Obviously, at a mesoscopic scale for a representative volume containing a large enough number of particles we may define an equivalent continuum with dynamical variables defined from the underlying particles and their interactions. The mechanical deformations of such a continuum can then be formulated either in a Lagrangian or Eulerian framework. The computational approaches developed for continuum are equation-based discretized models such as the Finite Element Method (FEM). HS-DEM simulations have provided high fidelity data that have been used to develop new rheological models of granular materials [51, 68]. These models can be applied within a continuum framework to solve boundary-value problems. Such models describe only bulk flow in particular regimes, but they can be used concurrently with DEM within a hybrid multiscale approach [25, 153, 24].

These differences between DEM and other methods (MD, CA, continuum PDEs) highlight the *unique status of DEM as a generic computational method for constrained particle dynamics*. It is common to distinguish purely collisional dynamics from multiscontact dynamics. Dense granular flows and packings exemplify this latter regime, but clustering and multicontact collisions occur also in dilute granular gases due to inelastic collapse [95]. An event-driven DEM algorithm is computationally more efficient in the collisional regime, but the general implementation of DEM does not distinguish between these two regimes. In fact, most industrial processes involve simultaneously the solid-like, liquid-like and gas-like states of granular materials. It seems therefore relevant to represent a granular system as an evolving graph of particles that transport momenta by both moving and propagating through the contact network. This analogy with a Graph Neural Network (GNN) is a useful analogy that can be exploited for the calculation of forces and velocities [149].

There are features in basic DEM that make it inappropriate for the simulation of real-world granular materials. Real particles are not spherical, they can have a rough surface, they can break or deform, they can obey complex interactions, and they have polydisperse input parameters. Nevertheless, without significant computational effort, it is possible to model arbitrary particle shapes as clumps of spherical particles. In the same way, within available computational power, size polydisperse assemblies of particles can be simulated. For cohesive materials simple laws of adhesion between particles can be added to elastic repulsion (Hertz or linear) and Coulomb friction. Particle breakage can also be modeled by representing the particles as clusters of bonded spherical particles that fail beyond a force or displacement threshold. Plastic behavior can be introduced by distinguishing loading and unloading paths at the contact points. Finally, rolling and twisting resistance can be implemented to allow the particles to resist relative rotations at their contact points. These simple add-ons and tricks added to the numerical material extend the applicability of HS-DEM to a broader class of materials thereby opening the way to a more general quantitative calibration and experimental validation. We refer to this level of sophistication of DEM as *extended DEM*.

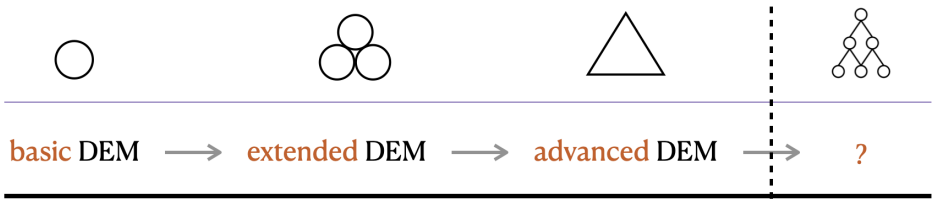

Figure 1: *The three levels of DEM with possible enhancement to a higher level in near future.*

Most reported work on numerical simulations of granular materials during the last two decades is based on the extended DEM together with significant effort for enhancing computational efficiency to increase the number of particles or speed up simulations for industry-related processes. However, as the expectations of DEM have turned to realistic simulations and quantitative validation, the attention has also been increasingly focussed on more realistic models of particles. Different particle shapes (elongated, polyhedral, super-quadrics…) and algorithms for shape representation and contact detection have been developed. New models of soft particles and particle breakage based on fracture mechanics have been proposed. Realistic models of adhesive elasto-plastic contacts have been developed and validated for binary collisions. Cemented granular materials with solid bonds have been modeled. Moreover, parallel computing and the GPU technology have been exploited to speed up simulations. All these new developments beyond extended DEM are more technical in nature and not yet quite popular in the community of potential users. We refer to these new developments as *advanced DEM*; see Fig. 1.

It is clear that most of the progress made from basic DEM towards advanced DEM has been driven by industrial need. Although the basic simple-to-complex upscaling paradigm is an attractive and minimally technical setting, with increasing complexity of the numerical material and technicality in DEM algorithms, the focus has moved from collective dynamics to the model material and influential parameters at the contact and particle scales. The underlying numerical material is therefore richer and closer to real-world materials. However, the interplay between this richer local physics and the collective dynamics of particles raises new challenges that will need to be addressed. Furthermore, the underlying models of particles and force laws are still based on a compromise between algorithmic tractability and physics fidelity. In this report, we will present some of the short-comings and pitfalls of DEM in its current state together with recent advances and new promising resources that can push its limits.

1.2 Nature of DEM simulations

We often tend to consider DEM simulations as ‘numerical experiments’. Von Neumann had noted that many difficult experiments had to be conducted merely to determine facts that ought, in principle, to be derivable from theory and he advocated for the use of simulations to replace experiments for this purpose. In other words, when analytical solutions of a model are not available, experiments that would be carried out to check the model behavior can be replaced by simulations [148]. Such simulations, when they are accurate, provide a wealth of information about particle motions, internal structures, and interactions forces, which are virtually impossible to gain from experiments. Furthermore, simulations can be designed to learn what happens to a system as a result of possible variations of the input parameters of the model. This is precisely what is needed when using simulations to search for innovative engineering solutions, and which best corresponds to the idea of *in silico* experiments or

digital twins with the aim of replicating the behavior of a physical system.

This viewpoint does not, however, reflect what DEM simulations offer in practice. First, there is no general theory of granular materials and DEM does not represent a discrete model of an existing upscaling theory. Secondly, the underlying physical model of DEM involves a number of more or less physically justified assumptions. The particles are assumed to be perfectly rigid and the force laws are treated by allowing small overlaps. The overlap is generally unphysical and it can represent an elastic or plastic deflection only for the Hertz solution between spherical particles. Moreover, energy dissipation is modeled by simple viscous or plastic terms, not reflecting the details of the contact interface. Finally, granular materials involve a high degree of randomness in shape, size and mechanical properties from particle to particle and in surface roughness and properties from point to point on the particle surface while DEM algorithms generally assume monodisperse (single-valued) input parameters. For all these reasons, the DEM results are the consequences of a model which does not exactly represent the real-world material under experimental investigation.

The point is that DEM is not just a mathematical algorithm for solving equations (equation-based view), but a combination of three ingredients:

1. numerical model of a granular material,
2. mathematical algorithm to solve particle interactions and predict the evolution of the system,
3. specification of the process or system with its boundary and initial conditions.

We will refer to this triplet as *DEM-based model*. It needs input data at all levels: material parameters, system parameters, and numerical algorithmic parameters. The algorithm may have different implementations, which involve a computational technology and a data structure. Figure 2 shows the elementary ingredients of a DEM-based model. In the following, by 'DEM' we generally mean 'DEM-based model'.

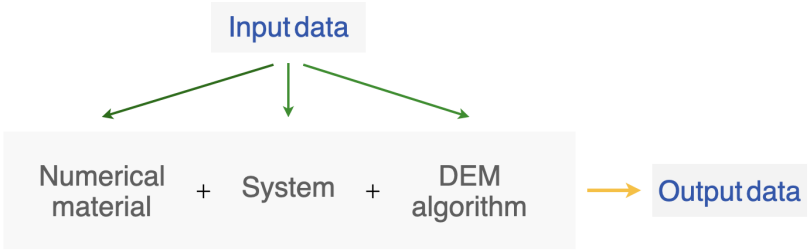

Figure 2: *DEM-based model.*

It is important at this point to carefully distinguish numerical material (or the numerical model of the granular material) from real material. Real material is characterized by experimental methods and tools developed for the chemo-physics and mechanics of granular materials. From these characterizations, a theoretical *model material* can be defined. This is a physical model that contains the geometrical (shapes, sizes), mechanical (elastic moduli, yield stress, toughness...), chemo-physical (surface energy, surface, roughness, heat capacity...), and statistical (variability) properties of the particles and their interactions (friction coefficient, restitution coefficient, rolling resistance...). The *numerical material* is then built from the model material by taking into account the constraints imposed by the algorithm; see Fig. 3. The numerical material is a constitutive ingredient of DEM. It is

Figure 3: *From real material to the numerical model simulated by DEM.*

necessarily simpler than model material but its realistic ingredients and technicality have considerably increased in gradual transition from basic DEM to advanced DEM.

The highest expectation of DEM is the idea that numerical simulation can be a substitute for experiment. Intuitively, using DEM for real systems means high-fidelity simulations that can replace experiments. This is an extreme viewpoint since it assumes that the real granular process (the one that is manipulated in the real world) can be fully described by a physical model of the material with a finite number of parameters and the algorithm can be tuned to calculate the evolution of the system with high precision while avoiding numerical instability at all scales, round-off errors, numerical dissipation, etc. This viewpoint is most valued and adopted by engineers and practitioners in industry. In the following, we will refer to it as viewpoint A; see Fig. 4.

The opposite viewpoint, to which we will refer as viewpoint B, is the expectation that DEM simulations serve as a substitute for theory. This viewpoint implies that the knowledge gained by DEM simulations is strictly equivalent to what can be gained from a theory of granular matter. By 'theory' we mean here an upscaling model which must be capable of predicting the macroscopic behavior from the underlying model material. This approach is sometimes called 'numerical homogenization' (replacing a 'theoretical' homogenization) and may involve a two-level upscaling: 1) from particle scale to an intermediate scale corresponding to a Representative Volume Element (RVE), and 2) from intermediate scale to process scale by means of an allied continuum method such as FEM. In this viewpoint, DEM is adopted as an alternative approach only in the absence of a theoretical (analytic) model based on a small number of (thermo)dynamic variables.

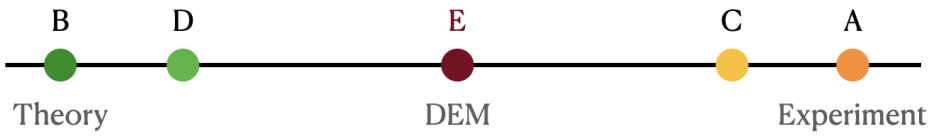

Figure 4: *Various possible epistemic positions of DEM with respect to theory and experiment.*

The two viewpoints A and B deny DEM as a stand-alone method for scientific discovery. They count on DEM as a replacement in the absence of a viable theory of granular matter or available experiments. In a slightly different viewpoint, DEM simulations are considered not as substitutes but as complements to either experiment (viewpoint C) or to theory (viewpoint D); see Fig. 4. It is argued that the underlying numerical model can never fully capture all the details of a real process. It should therefore be considered as an approximation which can be used in complement to experiments for a better understanding of the real process (viewpoint C) or as a complement to capture the physical mechanisms and microstructure at intermediate scales with the goal of elaborating a theory (viewpoint D).

Although the viewpoint C is common in research, it carries an inherent doubt about the trustworthiness of simulation results. For instance, when simulation results only partially match experimental tests, there is a trend to resort to unrealistic values of input parameters such as friction coefficient or

particle stiffness to re-match the simulation results to experimental data. This duality may lead to the uncomfortable situation where the simulation output data are credited for some tests and discredited for others. Obviously, the calibration of material parameters in such cases should not be falsified to reproduce experimental results. Instead, the shortcomings of the underlying numerical material must be examined in the framework of a rigorous uncertainty quantification. The viewpoint D leads to similar judgements. When the simulation results do not match a theoretical model such as the rheology of dense granular flows, there is a trend either to doubt simulation input parameters or to rely only on qualitative features of the simulation results with the motive that DEM is based on simplified assumptions.

The closest viewpoint to the effective role of DEM simulations in research and engineering is the *qualification of DEM as a peer method with theory and experiment*. We refer to this epistemic viewpoint as viewpoint E. This status of DEM means that *DEM simulations can be used to produce new knowledge independently of theory and experiment*. Much as theory, DEM provides a methodology to approach real granular processes when the core model (numerical material) reflects elements of a process that can be calibrated by means of experimental measurements. However, the core model should not be restricted to real materials, and the particles can be both conceptual or approximating real particles depending on the aims of the simulation. In this sense, DEM bears some analogy to Agent-Based Methods (ABM) [39]. The latter is a computational model for simulating the actions of autonomous agents to understand their cooperative behavior and the structures that they generate. Despite its simple discrete rules, ABM is broadly applied to economy, biological systems, epidemiology, and urban traffics. The specificity of DEM is that the particles are Lagrangian and governed by the Newton-Euler equations of motion. They transport momentum and kinetic energy, but they can also transport other scalar or vectorial information such as heat and electric charge which can be exchanged with other particles.

In viewpoint E, DEM is valued as a method for discovery. It can be employed in close connection with experiments but not as a replacement and its use is not warranted only by full validation, which is desirable but not currently accessible. Furthermore, the knowledge produced by simulation cannot be entirely compared with observation when the available data are sparse. Simulations are quite often used when experiments are hard to perform or out of reach for practical reasons, for example when dealing with radioactive powders in the manufacture of nuclear fuel. In such circumstances, DEM is a valuable approach although full validation is not available or requires a complex validation strategy.

This is an important point to consider since excessive emphasis on validation is generally motivated by the expectation that DEM must be capable of replacing experiment (viewpoint A). This may lead to unphysical calibration or inconsistencies in the choices of input parameters. For example, a large value of the adhesion force for the simulation of cohesive granular flows is sometimes adopted to compensate for a high value of contact stiffness as they are both involved in the effective cohesive stress of the material [94]. In a similar vein, rolling friction coefficient or increased sliding friction coefficient are sometimes used in dense granular flows to compensate for unrealistic particle shape [41, 114]. Therefore, DEM must be trusted and used with the same level of imagination as in experiments and theoretical modeling. A general reason we should trust simulations is because of the interpretive work of researchers who employ their skills to interpret simulation outputs. Furthermore, the quantification of uncertainty due to numerical approximations and inaccurate input data, verification (with theory) and validation (with experiments) must be applied with the goal of clearly quantifying the level of confidence in the results rather than simply sanctioning an implementation of the numerical model. In fact, the trustworthiness of DEM and its implementations arises exactly in the same process as in experiments and theory, i.e. from general consistency of the results and their scientific interpretations

on the one hand, and accurate identification of the model form errors that prompt further research and algorithmic developments, on the other hand.

In the following, we will consider several algorithmic ingredients of DEM to highlight both significant recent progress and new challenges and perspectives in each case. The goal is to provide an objective understanding of the key issues and resources that will drive future developments of granular modeling within and beyond DEM.

2 Contact interactions

In this section, we discuss the role of contact interactions and their implementation in DEM. These interactions are central to the mechanical behavior of the 'numerical material' but involve several ambiguities that have not been resolved or properly analyzed in the past. Herein, we briefly present each aspect and suggest further investigations that will be necessary to clarify its consequences for granular dynamics.

2.1 Normal force positivity

The normal contact interactions in granular materials are *unilateral* because of the impenetrability of particles. Hence, the relative normal velocity u_n at the contact point between two particles must be zero or positive. We assume the sign convention that the relative normal displacement is positive for increasing gap δ_n and negative for decreasing gap. Correspondingly, for cohesionless particles the normal force f_n must be positive or zero with the sign convention that repulsive forces are positive and attractive forces are negative. These two conditions are complementary in the sense of the graph shown in Fig. 5, known as Signorini's graph [97, 98, 64, 121]. It shows that either $f_n = 0$ with $u_n \geq 0$ or $u_n = 0$ with $f_n \geq 0$. This is the most general *contact law* as it applies to the contact point between two particles irrespective of whether the particles are undeformable (hard) or deformable (soft). Note also that Signorini's condition is not a *force law* in the sense that f_n is not a single-valued function of u_n and vice versa. It is simply the expression of a *unilateral constraint*.

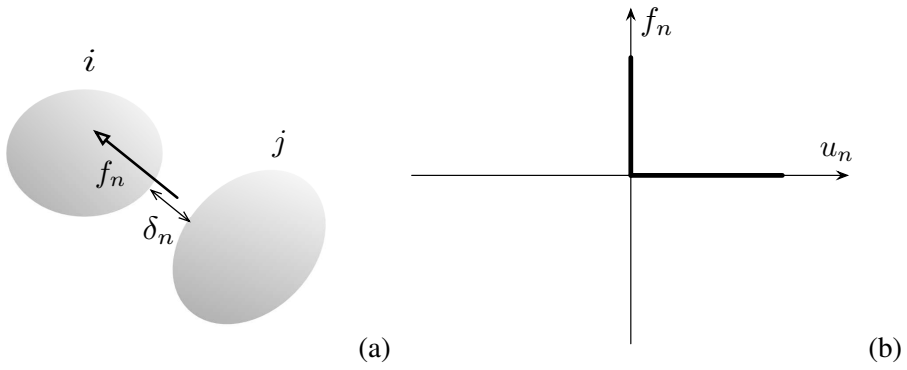

Figure 5: *(a) Geometry of a gap between two particles. (b) Signorini's graph relating normal relative velocity and normal force between two cohesionless particles.*

Signorini's condition is not exactly implemented in the framework of the conventional DEM algorithm. Instead, although the particles are assumed to be perfectly rigid, they are allowed to overlap (when the gap becomes negative) and the overlap δ_n is penalized by a repulsive elastic force f_n. In other words, the contact is soft with a finite stiffness k_n: $f_n = -k_n\delta_n$. This regularization or softening of Signorini's conditions transforms the contact law into a force law provided the maximum overlap δ_{max} is small compared to particle size d. For example, for a head-on collision between two particles of reduced mass m and impact velocity u_n^-, the kinetic energy in the center of mass is fully transformed into elastic potential energy (assuming zero energy dissipation) when the maximum overlap δ_{max} is reached, so that $m(u_n^-)^2 = k_n(\delta_{max})^2$. Hence, $\delta_{max} = -u_n^-(m/k_n)^{1/2}$ and the condition $\delta_{max} \ll d$ implies that the particle velocities in a granular material must be $\ll (d/2)(k_n/m)^{1/2}$. In the same way, in a static granular material subjected to a confining stress σ, the order of magnitude of normal forces

is σd^2 and the condition $\delta_{max} \ll d$ implies $\sigma \ll k_n/d$. Note that k_n/d is the order of magnitude of the bulk elastic modulus of a static packing.

For smooth particle surfaces with well-defined curvatures at the contact point, the overlap coincides with an approximate value of elastic displacement (Hertz law) and k_n is a function of δ_n ($k_n \propto (-\delta_n)^{1/2}$) and the elastic moduli and sizes of the two particles. In all other cases, the relationship between δ_n and k_n is more complex. However, for practical reasons, in most DEM simulations a linear elastic law with a constant value of k_n is used. It is equivalent to a linear unilateral spring acting at the contact point.

To account for contact inelasticity, a viscous damping term is often added to the normal elastic repulsion force:

$$f_n = -k_n\delta_n - 2\alpha\sqrt{k_n m}\,\dot{\delta}_n. \tag{1}$$

The damping coefficient is scaled by $\sqrt{k_n m}$, which is homogeneous to a viscosity, and the dimensionless number α can take a value between 0 and 1. This viscous damping term accounts for normal energy dissipation although energy is generally dissipated by plastic deformation of the particles or plastic deformation and damage in the contact zone. The restitution coefficient $e_n = -u_n^+/u_n^-$, defined as the ratio of relative velocity u_n^+ after a collision and the relative impact velocity u_n^-, is a physical quantity that can be experimentally measured and is a function of α:

$$e_n = e^{-\pi\alpha/\sqrt{1-\alpha^2}}. \tag{2}$$

For $\alpha = 0$, the contact is is fully elastic with $e_n = 1$ whereas for $\alpha = 1$ the contact is fully inelastic with $e_n = 0$. Therefore, the viscous term with its parameter α is accepted as an internal numerical variable of the algorithm whose main function is to dissipate energy and can be calibrated with the experimentally measurable quantity e_n from binary collisions [85, 16].

Although this force model is commonly used in most implementations of DEM, it has two major side effects:

1. One side effect of the viscous term is that the positivity of the total contact force f_n is not ensured. Indeed, the value of the damping term in equation (1) can be negative with an absolute value larger than the elastic force $f_n^e = -k_n\delta_n$. This is more likely to happen for small values of the overlap. For example, in a normal collision between two particles, the total force just before separation (where $\delta_n = 0$) is $f_n = 2\alpha\sqrt{k_n m}\; e_n u_n^-$, which has a negative value. More generally, in a granular flow the relative velocity $u_n = \dot{\delta}_n$ between two particles depends on the collective dynamics of neighboring particles so that v_n can take large values. One example is sketched in Fig. 6 where a particle hits another particle which is in contact with a third particle. The collision tends to separate the two last particles with a relative velocity induced by that of the first particle, leading to negative force f_n if the velocity is sufficiently high.

2. Another side effect is that the negative force is set to zero at the moment the contact disappears. Such a discontinuous change of the force leads to strong fluctuations in the neighborhood of the particles.

Different solutions have been devised to avoid negative forces induced by the viscous damping term. One solution consists in keeping the viscous term but simply considering the elastic force f_n^e as the 'real' contact force. In other words, not only the output normal forces are the elastic forces (and not the total force), but the friction force $f_t = \mu f_n$, where μ is the friction coefficient, is also calculated by setting $f_n = f_n^e$. This is the solution adopted by most commercial softwares. This approach is not

physically acceptable as the dissipative force can not be artificially distinguished from the conservative forces. Furthermore, this approach keeps discontinuous force change upon contact opening.

Another possible solution consists in activating the damping term only when the relative normal velocity is negative. This amounts to multiplying the damping term by a Heaviside function $H(-\dot{\delta}_n)$:

$$f_n = -k_n\delta_n - 2\alpha\sqrt{k_n m}\, H(-\dot{\delta}_n)\dot{\delta}_n. \tag{3}$$

For example, in normal collision between two particles the damping term is inactive during their separation. As a result, the new coefficient of restitution e_n' is higher than e_n. It can be shown that

$$e_n' = \frac{1}{\sqrt{2}}\sqrt{1+e_n^2}. \tag{4}$$

In the example of Fig. 6, this method will lead to a positive value (repulsion) of the normal force f_n. In this approach, the force is a continuous function of time. However, e_n' has a lower bound $\sqrt{2}/2$, which is rather high.

Another possible solution consists in setting the total force to zero whenever the total force is negative [129]:

$$f_n = -(k_n\delta_n + 2\alpha\sqrt{k_n m}\ \dot{\delta}_n)H(-k_n\delta_n - 2\alpha\sqrt{k_n m}\ \dot{\delta}_n). \tag{5}$$

The corresponding restitution coefficient e_n' can be analytically calculated and, as expected, its value tends asymptotically to zero for large values of α (the latter taking values above 1 in this case); see Fig. 7. This approach ensures force continuity. However, the normal force vanishes most of time for a nonzero overlap.

The two last solutions solve the problems of positivity and force continuity. However, when using them in DEM, the calibration must be based on the modified analytical expression e_n' of the restitution coefficient. Otherwise, by reducing dissipation, they can lead to excessive fluidization or reduced clustering due to inelastic collisions. The challenge is mainly about the consequences of each approach for multiple collisions or multicontact systems. Most past investigations are limited to free collisions between particles. It is therefore necessary to compare the three methods for benchmark tests involving dense granular flows at high shear rates where the restitution coefficient plays an effective role. Clustering in granular gases and fluidization in the dilute regime can also be sensitive to the adopted approach. Note that similar effects occur also for nonlinear force laws.

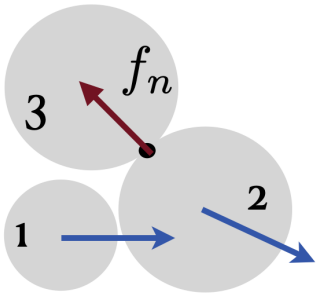

Figure 6: Collision between particles 1 and 2 leads to an attractive force f_n at the contact between particles 2 and 3.

Let us also remind that other normal force laws involving no damping term have been proposed. For example, plastic dissipation is introduced by means of a contact stiffness for loading ($\dot{\delta}_n < 0$)

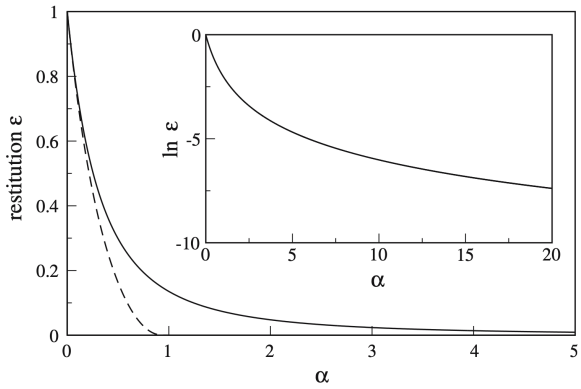

Figure 7: Original (dashed line) and modified (solid line) normal restitution coefficients as a function of parameter α in equations (1) and (5), respectively [129].

and a higher stiffness for unloading ($\dot{\delta}_n < 0$) [136, 110, 138]. The loading-unloading process leads to a residual overlap when the normal force vanishes upon unloading. This overlap is equivalent to a plastic deformation and must be kept in memory for subsequent relative displacements for the same pair of particles. The memory of a plastic deformation due to a loading-unloading history is a property of a small zone at the surface of each particle around their contact point. Even if the contact persists, its position on the surface of each particle moves by the relative of the two particles. In other words, this memory can be used only if the positions of successive contacts are tracked on the particle surface or if rolling is frozen The same criticism holds also for tangential elastic strains used for the implementation of the Coulomb friction law; see section 2.2.

Another approach used for energy dissipation consists in applying the damping viscous force at the particle centers of mass in analogy to drag forces in a viscous fluid. This approach has the obvious advantage of strongly damping long-wavelength oscillations, but it cannot be mapped into an intrinsic property of the particles. Furthermore, as the damping force depends on the absolute value of particle velocities, it makes depend the dynamics of the material on the reference frame.

We briefly mentioned the calibration of the damping coefficient α from experimental measurements of the restitution coefficient. It is worth reminding here that the effectiveness of this calibration depends on the numerical precision with which the particle displacements are calculated. The intrinsic time scale (independent of external loading) of granular flows is $(m/k_n)^{1/2}$. For example, the duration t_c of a head-on collision between two particles interacting according to equation (1) is

$$t_c = \pi(1-\alpha^2)^{-1/2}\left(\frac{m}{k_n}\right)^{1/2} \tag{6}$$

To ensure smooth motion, this characteristic time should be well resolved, i.e. the time step τ must be well below t_c. It has been shown that an accurate simulation, reproducing the analytic value of e_n with relative error of the order of 10^{-4}, requires a time step $\tau \sim t_c/100$ [128]. For cohesive contacts, it was found that the prediction of the critical velocity for rebound in a binary collision requires $\tau < t_c/50$ [73].

2.2 Friction law

The Coulomb friction law is a fundamental ingredient of granular materials. In its theoretical formulation, it can be represented as a graph relating the sliding velocity u_t at a contact point and the tangential force f_t. It states that either $u_t > 0$ and $f_t = -\mu f_n$ or $u_t < 0$ and $f_t = \mu f_n$ or $u_t = 0$ with $-\mu f_n < f_t < \mu f_n$ [98, 64, 121]. As the Signorini condition, this is a contact law which can not be reduced to a single-valued function. The value of the friction force is basically indeterminate when there is no sliding. In this sense, it is not a force law but a constraint on the relative tangential motion of two particles. Its value is determined by the equations of dynamics and dynamic state of the system (typically, all other forces and velocities acting on the two particles).

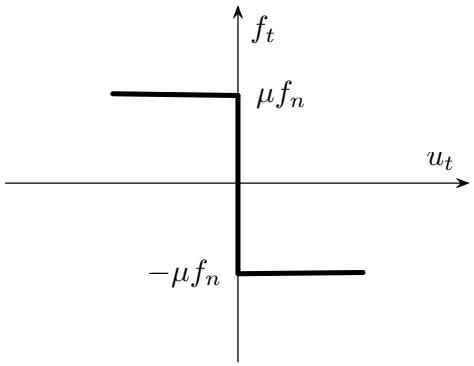

Figure 8: *Coulomb graph representing the relationship between friction force f_t and sliding velocity u_t at a contact point.*

Two methods have been used to approximate the Coulomb friction law by a force law for its implementation in DEM [138]:

1. *Viscous regularization* consists in replacing the vertical branch of the Coulomb graph by a line of finite slope, so that the friction force in the range $[-\mu f_n, \mu f_n]$ is given by $f_t = -\eta u_t$. The negative sign means opposite to the direction of sliding. The value of the artificial viscosity η must be high enough to keep the sliding velocity as small as possible while the friction force is not fully mobilized (i.e. when $f_t \in [-\mu f_n, \mu f_n]$).

2. *Elastic regularization* consists in replacing the Coulomb graph by its integrated form over time. Then, the velocity u_t is replaced by a tangential displacement δ_t and the vertical branch by a linear relation between δ_t and f_t with a stiffness k_t: $f_t = -k_t \delta_t$. This has the advantage of introducing a tangential stiffness k_t, which can be determined as a function of the elastic moduli of the particles. Its implementation requires cumulating the tangential displacement and keeping its value in memory. Elastic regularization is more widely used in DEM codes than viscous regularization. Generally, a tangential damping term is also added to the tangential force to account for tangential restitution coefficient e_t much in the same spirit as the normal restitution coefficient.

Viscous regularization has two obvious problems:

1. It does not reproduce all features of oblique collisions between two particles as a result of the absence of tangential elastic rebound [138].

2. At static equilibrium, i.e. in the limit where all particle velocities (including their rotations) vanish, the tangential forces vanish, too.

Elastic regularization is also problematic in three respects:

1. It requires the cumulative tangential elastic displacement δ_t while the location of contact on the particle surface may move by rolling, implying therefore the unphysical assumption that the tangential elastic energy (elongation of the fictitious spring) is transported with rolling at the surface of each particle.

2. In 3D, the cumulative displacement in the contact plane is a vector that is expected to rotate if both particles rotate around the contact normal (torsion) while the relative tangential velocity depends on the velocities of the particle centers of mass and rotations in the orthogonal direction. For this reason, the cumulative elastic displacement at the contact point is not an objective quantity.

3. The cumulative tangential displacement or elastic energy depends on the past states of the system, making therefore depend the current forces on the memory of past displacements and not only on the current dynamic state. However, the existence of such a 'tangential memory' has not been proved in sheared granular materials. If such a memory is an important effect, then the tangential forces have to be specified at the initial state of the system in addition to the positions and velocities of the particles.

The vanishing of tangential forces in the case of viscous regularization may appear as a serious pitfall. However, in a simulated granular material based on viscous regularization of the friction law, the tangential velocities never vanish! In fact, the static equilibrium is established when all forces are determined with a 'residual' relative tangential velocity, which is negligibly small if the viscosity η is high. For example, if a granular packing is subjected to a confining pressure p and if we assume that the system is stable for an observation time τ, then for $\eta \gg pd\tau$ the equilibrium is reached with residual velocities $u_n \ll d/\tau$. This means that the particles are virtually in equilibrium with a small creep motion. The observation time is a sufficiently long time for all velocities to reach their residual or creep values. Note also that the stability of the time-stepping process is independent of the value of η.

These two implementations of the Coulomb friction law have not been compared for their influence on the dynamics of a granular material. As in the case of normal interactions laws, the tangential force laws are implemented within the constraints imposed by the DEM algorithm. Hence, we need to understand quantitatively the influence of different implementations on the granular dynamics in multicontact states, i.e. with multiple contacts and collisions. As far as different implementations satisfy the general requirement of *constrained dynamics*, i.e. particle motions according to the equations of dynamics and constrained by unilateral contact and Coulomb friction, their differences reflect mainly the dissipation parameters, which influence the dynamics via the mechanisms that they activate. In particular, collective dissipation involves preferential activation of physical mechanisms that require lowest energy cost. This is reflected, for example, in the organization of particle rotations across the system [118]. When the rolling friction coefficient is lower than the sliding friction coefficient, particle displacements occur mostly by rolling, and vice versa [42]. In dense granular materials subjected to quasi-static shearing, localized deformation (shear bands) occurs despite homogeneous loading [43, 71]. Dilatancy is another mechanism which is not activated when dissipation by shear deformation is low [112].

Contact stiffness is often physically ineffective in most simulations of cohesionless granular materials since the restitution coefficient is independent of stiffness [151]. If the contact stiffness explicitly enters the expression of the restitution coefficient based on a different interaction model, then the stiffness will impact the behavior. Another example is the shear strength (or internal friction angle) of granular flows, which is not sensitive to the value of the particle-particle friction coefficient μ when the latter is above 0.5 [133]. In the same way, the rheology of granular materials in the dense regime is practically independent of restitution coefficient when the latter is not too close to 1 [33]. This is because high-frequency elastic waves and frictional slips efficiently dissipate energy in dense granular flows. Nevertheless, although this behavior seems to be quite robust, the number of sliding contacts may well depend on the implementation [122, 132]. In other words, the same macroscopic quantity such as shear strength may be obtained for different organizations of the contact network. This 'self-organization' of the microstructure is similar to the self-averaging property of molecular systems, both tending to screen the effect of some local parameters. For this reason, the validation of a DEM implementation should not be solely based on the macroscopic variables.

2.3 Contact dynamics

We mentioned different implementations of the normal and tangential force laws in the conventional DEM algorithm and discussed their possible consequences through a few examples. Another interesting approach consists in using the contact laws as sketched in Figs. 5(b) and 8 without regularization. This is not just another implementation, but a different algorithm called Contact Dynamics Method (CDM), which, as previously mentioned, can be qualified as *nonsmooth DEM*. We briefly describe its major traits (here for a 2D system) as we believe that this method may play an important role in future developments for soft particles. A more detailed introduction to this method and its mathematical foundations can be found elsewhere [98, 121].

Signorini's condition and Coulomb's friction law are inequalities that express constraints on the contact velocities u_n and u_t (relative velocities at the contact points) and the corresponding normal and tangential forces f_n and f_t. They apply to the geometrical contacts, implying that, at the beginning of a time step the contact network must be explicitly identified. Then, the velocities and contact forces can be calculated by using the contact laws and equations of dynamics. The contact network is set up from the positions of the particles, and the positions are updated simply by using the current positions and the computed velocities: $\delta_n(t+\tau) = \delta_n(t) + u_n(t+\tau)\tau$ and $\delta_t(t+\tau) = \delta_t(t) + u_t(t+\tau)\tau$, where τ is the time step. Note that implicit time stepping is assumed since, according to Signorini's condition, all relative normal velocities must be positive definite and computed such that the update of positions would not lead to an overlap, and the tangential forces should remain inside the Coulomb cone. This is known as the *prospective feature* of contact dynamics. Either the contact is persistent (i.e. $u_n(t+\tau) = 0$) or opening ($u_n(t+\tau) > 0$). It is clear that, within the finite precision of the calculations, small overlaps occur, but in CDM they do not represent an elastic displacement.

Since the contact laws are expressed in terms of the contact variables u_n, f_n, u_t, and f_t, we transform the equations of dynamics written for particles variables $\boldsymbol{U}$ and $\boldsymbol{F}$ into equations for contact variables. The equations of dynamics can be written in a compact form for a set of N_p particles in matrix representation. The particles are labelled with integers $i \in [1, N_p]$. The forces and force moments $F_x^i, F_y^i, \mathscr{M}^i$ acting on the particles i are arranged in a single high-dimensional column vector $\boldsymbol{F}$ belonging to $\mathbb{R}^{3N_p}$. In the same way, the external bulk forces $F_{ext,x}, F_{ext,y}, \mathscr{M}_{ext}$ applied on the particles and the particle velocity components U_x^i, U_y^i, ω^i are represented by column vectors $\boldsymbol{F}_{ext}$ and $\boldsymbol{U}$, respectively. The particle masses and moments of inertia define a diagonal $3N_p \times 3N_p$ matrix denoted by $\boldsymbol{M}$.

With these notations, the equations of dynamics are cast into a single matrix equation:

$$\boldsymbol{M}(\boldsymbol{U}^{+}-\boldsymbol{U}^{-})=\tau(\boldsymbol{F}+\boldsymbol{F}_{ext}) \tag{7}$$

The contacts are labelled with integers $\alpha \in [1,N_c]$, where N_c is the total number of contacts identified from the current positions of the particles. Like particle velocities, the contact velocities u_n^α and u_t^α can be collected in a column vector $\boldsymbol{u} \in \mathbb{R}^{2N_c}$. In the same way, the contact forces f_n^α and f_t^α are represented by a vector $\boldsymbol{f} \in \mathbb{R}^{2N_c}$. We would like to express the equations of dynamics from for the contact variables.

The formal transformation of matrix equations (7) is straightforward. Since the contact velocities $\boldsymbol{u}(u_n,u_t)$ are linear in particle velocities $\boldsymbol{U}$, the transformation of the velocities is an affine application:

$$\boldsymbol{u}=\boldsymbol{G}\,\boldsymbol{U} \tag{8}$$

where $\boldsymbol{G}$ is a $2N_c \times 3N_p$ matrix containing basically information about the geometry of the contact network. A similar linear application relates $\boldsymbol{f}$ to $\boldsymbol{F}$:

$$\boldsymbol{F}=\boldsymbol{H}\,\boldsymbol{f} \tag{9}$$

where $\boldsymbol{H}$ is a $3N_p \times 2N_c$ matrix. We will refer to $\boldsymbol{H}$ as *contact matrix*. It contains the same information as $\boldsymbol{G}$ in a dual or symmetric manner. It can easily be shown that

$$\boldsymbol{H}=\boldsymbol{G}^T \tag{10}$$

where $\boldsymbol{G}^T$ is the transpose of $\boldsymbol{G}$. This property can be inferred from the equivalence between the power $\boldsymbol{F}\cdot\boldsymbol{U}$ developed by the 'generalized' forces $\boldsymbol{F}$ and the power $\boldsymbol{f}\cdot\boldsymbol{u}$ developed by the bond forces $\boldsymbol{f}$. In general, the matrix $\boldsymbol{H}$ is singular and, by definition, its null space has a dimension at least equal to $2N_c-3N_p$. A schema of this transformation from particle dynamics to contact dynamics equations is displayed in Fig. 9.

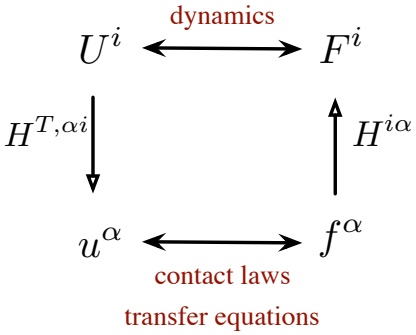

Figure 9: *Matrix transformation between the particle and contact variables.*

The matrix $H^{i\alpha}$ can be decomposed into two matrices $H_n^{i\alpha}$ and $H_t^{i\alpha}$ such that

$$\begin{aligned} u_n^\alpha &= \sum_i H_n^{T,\alpha i}\,U^i \\ u_t^\alpha &= \sum_i H_t^{T,\alpha i}\,U^i \end{aligned} \tag{11}$$

and

$$F^i=\sum_\alpha (H_n^{i\alpha}\,f_n^\alpha + H_t^{i\alpha}\,f_t^\alpha) \tag{12}$$

Using these relations, Eqs. (7) can be transformed into two equations for each contact α:

$$\begin{aligned} u_n^{\alpha+} - u_n^{\alpha-} &= \tau \sum_{i,j} H_n^{T,\alpha i}\, M^{-1,ij}\, \{\sum_{\beta} (H_n^{j\beta} f_n^{\beta} + H_t^{j\beta} f_t^{\beta}) + F_{ext}^{j}\} \\ u_t^{\alpha+} - u_t^{\alpha-} &= \tau \sum_{i,j} H_t^{T,\alpha i}\, M^{-1,ij}\, \{\sum_{\beta} (H_n^{j\beta} f_n^{\beta} + H_t^{j\beta} f_t^{\beta}) + F_{ext}^{j}\} \end{aligned} \tag{13}$$

These equations involve the velocities u_n^+ and u_t^+ at the end of a time step and the velocities u_n^- and u_t^- at the beginning of the time step. However, Signorini's condition and Coulomb's friction law involve the velocities u_n and u_t without specifying the time. Therefore a weighted mean of the velocities at the beginning and at the end of the time step is considered. This formal intermediate velocity can also be calibrated such that over a simple binary collision, the ratio is the restitution coefficient:

$$u_n = \frac{u_n^+ + e_n\, u_n^-}{1+e_n}. \tag{14}$$

and

$$u_t = \frac{u_t^+ + e_t\, u_t^-}{1+e_t}. \tag{15}$$

We now can make appear explicitly linear relations between the contact variables from Eqs. (13). We set

$$\mathscr{W}_{k_1k_2}^{\alpha\beta} = \sum_{i,j} H_{k_1}^{T,\alpha i} M^{-1,ij} H_{k_2}^{j\beta}, \tag{16}$$

where k_1 and k_2 stand for n or t. With this notation, Eqs. (13) can be rewritten as

$$\begin{aligned} \frac{1+e_n}{\tau}\,(u_n^{\alpha} - u_n^{\alpha-}) &= \mathscr{W}_{nn}^{\alpha\alpha} f_n^{\alpha} + \mathscr{W}_{nt}^{\alpha\alpha} f_t^{\alpha} \\ &+ \sum_{\beta(\neq\alpha)} \{\mathscr{W}_{nn}^{\alpha\beta} f_n^{\beta} + \mathscr{W}_{nt}^{\alpha\beta} f_t^{\beta}\} + \sum_{i,j} H_n^{T,\alpha i} M^{-1,ij} F_{ext}^{j} \end{aligned} \tag{17}$$

$$\begin{aligned} \frac{1+e_t}{\tau}\,(u_t^{\alpha} - u_t^{\alpha-}) &= \mathscr{W}_{tn}^{\alpha\alpha} f_n^{\alpha} + \mathscr{W}_{tt}^{\alpha\alpha} f_t^{\alpha} \\ &+ \sum_{\beta(\neq\alpha)} \{\mathscr{W}_{tn}^{\alpha\beta} f_n^{\beta} + \mathscr{W}_{nt}^{\alpha\beta} f_t^{\beta}\} + \sum_{i,j} H_t^{T,\alpha i} M^{-1,ij} F_{ext}^{j} \end{aligned} \tag{18}$$

The coefficients $\mathscr{W}_{k_1k_2}^{\alpha\alpha}$ for each contact α can be calculated as a function of the contact geometry and inertia parameters of the two partners 1_α and 2_α of the contact α. Let $\vec{c}_i^{\,\alpha}$ be the contact vector joining the center of mass of particle i to the contact α. The following expressions are easily established:

$$\begin{aligned} \mathscr{W}_{nn}^{\alpha\alpha} &= \frac{1}{m_{1_\alpha}} + \frac{1}{m_{2_\alpha}} + \frac{(c_{1t}^{\alpha})^2}{I_{1_\alpha}} + \frac{(c_{2t}^{\alpha})^2}{I_{2_\alpha}}, \\ \mathscr{W}_{tt}^{\alpha\alpha} &= \frac{1}{m_{1_\alpha}} + \frac{1}{m_{2_\alpha}} + \frac{(c_{1n}^{\alpha})^2}{I_{1_\alpha}} + \frac{(c_{2n}^{\alpha})^2}{I_{2_\alpha}}, \\ \mathscr{W}_{nt}^{\alpha\alpha} &= \mathscr{W}_{tn}^{\alpha\alpha} = \frac{c_{1n}^{\alpha} c_{1t}^{\alpha}}{I_{1_\alpha}} + \frac{c_{2n}^{\alpha} c_{2t}^{\alpha}}{I_{2_\alpha}}, \end{aligned} \tag{19}$$

where $c_{in}^{\alpha} = \vec{c}_i^{\,\alpha} \cdot \vec{n}^{\alpha}$ and $c_{it}^{\alpha} = \vec{c}_i^{\,\alpha} \cdot \vec{t}^{\alpha}$ are the components of the contact vectors in the contact frame. Note that the coefficients $\mathscr{W}_{k_1k_2}^{\alpha\alpha}$ are generalized inverse reduced inertia.

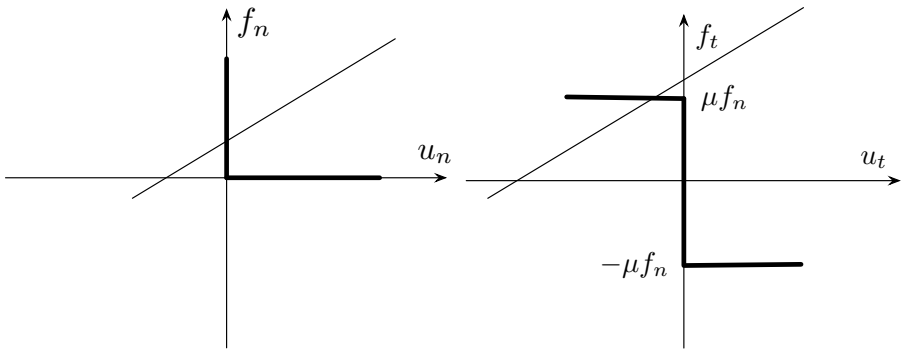

Figure 10: Contact laws (graphs) and lines representing the equations of dynamics expressed in the contact frame (contact dynamics equations).

An alternative representation of Eqs. (17) and (18) is

$$\mathscr{W}_{nn}^{\alpha\alpha} f_n^\alpha + \mathscr{W}_{nt}^{\alpha\alpha} f_t^\alpha = \frac{1}{\tau}(1+e_n)\, u_n^\alpha + a_n^\alpha, \tag{20}$$

$$\mathscr{W}_{tt}^{\alpha\alpha} f_t^\alpha + \mathscr{W}_{tn}^{\alpha\alpha} f_n^\alpha = \frac{1}{\tau}(1+e_t)\, u_t^\alpha + a_t^\alpha. \tag{21}$$

The two offsets a_n^α and a_t^α can easily be expressed from the equations (17) and (18). We refer to Eqs. (20) and (21) or Eqs. (17) and (18) as *contact dynamics equations*.

The equations (20) and (21) define a system of two linear equations between the contact variables at each contact point. The solution is given by the intersections of the lines representing contact dynamics equations with Signorini's and Coulomb's graphs; see Fig. 10. The intersection occurs at a unique point due to the positivity of the coefficients $\mathscr{W}_{k_1k_2}^{\alpha\alpha}$ (positive slope). The offsets a_n^α and a_t^α depend on the forces and velocities at contacts $\beta \neq \alpha$; Hence, the solution for each contact depends on all other contacts of the system and it must be determined simultaneously for all contacts.

In order to solve the system of $2N_c$ contact dynamics equations with the corresponding contact laws, one proceeds by an iterative method converging to the solution simultaneously for all contact forces and velocities. For each contact α, the variables f_n^α, f_t^α, u_n^α and u_t^α are determined given the values of the offsets a_n^α and a_t^α. An intuitive and robust method to solve the global SC problem is to search the solution as the limit of a sequence $\{f_n^\alpha(k), f_t^\alpha(k), u_n^\alpha(k), u_t^\alpha(k)\}$ with $\alpha \in [1, N_c]$. Let us assume that the transient set of contact forces $\{f_n^\alpha(k), f_t^\alpha(k)\}$ at the iteration step k is given. From this set, the offsets $\{a_n^\alpha(k), a_t^\alpha(k)\}$ for all contacts can be calculated. The contact forces and velocities are calculated for each contact α given the values of the offsets, yielding an updated set of contact forces $\{f_n^\alpha(k+1), f_t^\alpha(k+1)\}$. Remark that this force update procedure does not require the contact velocities $u_n^\alpha(k+1), u_t^\alpha(k+1)\}$ to be calculated as the offsets depend only on the contact forces. The set $\{f_n^\alpha(k), f_t^\alpha(k)\}$ evolves with k by successive corrections and it converges to a solution satisfying contact dynamics equations and contact laws at all contacts.

The iteration can be stopped when the set $\{f_n^\alpha(k), f_t^\alpha(k)\}$ is stable with regard to the force update procedure within a prescribed precision criterion ε_f:

$$\frac{|\, f^\alpha(k+1) - f^\alpha(k)\,|}{f^\alpha(k+1)} < \varepsilon_f \quad \forall \alpha. \tag{22}$$

Finally, from the converged contact forces, the particle velocities $\{\vec{U}^i\}$ can be computed by means of the equations of dynamics and used to update particle positions.

This iterative process is generally robust and efficient. It is equivalent to a nonlinear Gauss-Seidel method. The evolution of the contact variables during the iteration process is smooth and gradually converges to the final solution. Information needed to update contact variables is treated locally and no large matrices are manipulated during iterations. The conjugate gradient method can also be used to find the solution [123]. The method is unconditionally stable due to its implicit time-stepping scheme. Hence, no damping parameters at any level are needed. Furthermore, since small elastic strains and characteristic times are not introduced, the time step τ can be much larger than in the conventional DEM algorithm.

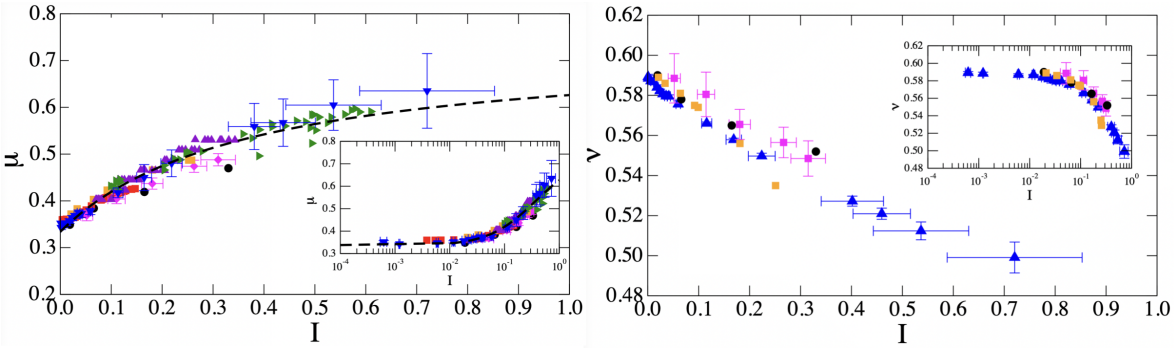

Figure 11: *Macroscopic friction coefficient μ_{eff} and packing fraction ν as a function of inertial number I. The CDM data are in blue triangles and pink diamonds. The experimental data are in green and purple triangles. All other symbols are DEM simulations. The dashed line is an analytical fit [7].*

The CDM has been partially compared with the common DEM for granular flows in 2D and 3D. Figure 11 shows the macroscopic friction coefficient μ_{eff} and packing fraction ν as function of the inertial number for granular flows composed of spherical particles and sheared in a confined geometry with increasing shear rate and constant pressure [7]. The inertial number is $I = \dot{\gamma} d \sqrt{\rho / p}$, where $\dot{\gamma}$ is the shear rate, ρ is particle density, and p is confining pressure. We see that the CDM data are in close agreement with both experimental and conventional DEM data within statistical precision shown as error bars. It has also been checked that the force distributions in static packings calculated in the same conditions by both CDM and DEM are quite similar [125].

The CDM is a method for the calculation of contact forces and velocities in multicontact systems independently of the nature of the solid bodies. Although the formulation briefly outlined in this section assumes rigid particles, CDM can be applied to both deformable and undeformable particles [103]. It can therefore be qualified as a method based on *hard contacts and soft particles* in contrast to the conventional DEM, which assumes *soft contacts and hard particles*. It is also noteworthy that a strong point of CDM is that key features of contact interactions such as normal force positivity, Coulomb friction law, and restitution coefficients are implemented in a straightforward manner whereas in the conventional DEM they are indirect and involve parameters that need special calibration.

2.4 Cohesive contacts

Cohesive contacts have been at the focus of extensive cross-disciplinary research for a long time, but during the last two decades the need for accurate and adequate cohesive force laws in DEM simulations has motivated new developments. These efforts represent a twofold motivation: 1) Capturing the

underlying physics of adhesion and solid bonding for viscoelastic and elastoplastic particles and quantifying the effects of surface roughness (the physical model material), and 2) Developing operational models to allow for calibration and reduce computational cost while keeping relevant ingredients (the DEM numerical material). As in other sections, our aim is not to review these developments, but to bring out a clear orientation for future progress.

Cohesive interactions have three different origins:

1. Forces acting between the mass centers of particles (e.g. colloidal forces for small particles or magnetic forces),

2. Short-range forces acting at the contact zone (e.g. chemo-physical forces),

3. Binding material partially filling the pore space (e.g. liquid bridges and cementing materials).

As we go from the first type to the third type, the action of cohesion involves more degrees of freedom: axial (along the contact normal), shear, rolling, and twisting. In all cases, the mechanical effect of cohesion deeply depends also on surface roughness, contact stiffness, plastic behavior, and viscous dissipation.

It is also essential to distinguish *active* cohesion from *passive* cohesion. This is illustrated in Fig. 12 in the simple case of a linear elastic repulsion together with a constant cohesive force $-f_c$. In the active case, the force $-f_c$ is part of the contact force and the total force is $f_n = -k_n\delta_n - f_c$. When two particles touch (at $\delta_n = 0$), the cohesive force is spontaneously activated and the balance between elastic repulsion and cohesive force occurs for an overlap $-\delta_c = -f_c/k_n$. If a dissipative force is added, the equilibrium is reached in finite time and it is stable. When the two particles are pulled apart, the force becomes tensile and decreases down to $-f_c$ at $\delta_n = 0$, where the contact breaks. The adhesion energy $f_c^2/2k_n$ is lost (dissipated) upon contact rupture. The phenomenology of active cohesion induced by surface energy is much more complex in real contacts and will be briefly considered later. In the passive case, the total force is zero at contact $\delta_n = 0$ and the cohesive tensile force is activated only when the two particles are pulled apart down to the pullout force $-f_c$ for a gap equal to δ_c.

Although the two cohesion laws seem similar up to a translation δ_c, there is a major difference: the contact area and elastic energy in equilibrium are nonzero in the active case and zero in the passive case. Hence, the friction force is zero in the passive case while it can be mobilized to μf_c in the active case. In fact, passive cohesion is more conveniently described in terms of a *tensile strength*, which is $-f_c$, as well as a *shear strength*. Like the normal force, the shear force is zero in the absence of external loading unless a shearing action is applied, and the contact breaks in shear when the force threshold in shear, which may depend on the tensile strength, is reached. This type of cohesion is generally irreversible and used in DEM simulations of cementitious and sintered materials. The macroscopic behavior (stress-strain behavior, elastic moduli, yield surface) of such cohesive aggregates under static and dynamic loading is a consequence of the granular microstructure and the cohesive strength of contacts.

The most general framework to describe the strength of a contact governed by passive cohesion is the contact *yield surface* or strength envelop [36, 65]. The force variables at the contact point are the normal force f_n, shear force f_t, rolling moment M_r, and twisting moment M_t. The yield function $\zeta(f_n, f_t, M_r, M_t)$ is defined such that the cohesive bond breaks for $\zeta \geq 0$. Fig. 13 shows an example of a yield surface matching well the behavior of epoxy resin. Several authors have used yield envelop derived from the beam theory, which is plausible if the geometry of the solid bridge can be

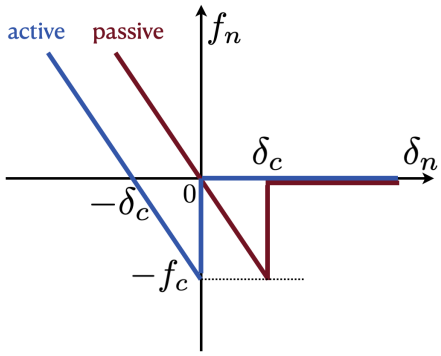

Figure 12: *Passive elasto-cohesive force law versus active elasto-cohesive force law. Note that overlap δ_n is on the left side (negative sign) and gap $-\delta_n$ is on the right side.*

approximated by a cylindrical neck [19]. Depending on the binding material, the behavior can be purely elastic or elasto-plastic for $\zeta < 0$ (before contact failure). It depends on the properties of the bond and particles. They are expressed as force-displacement functions.

In general, the yield surface reflects the fracture energy. For example, for linear springs the function $\zeta = f_n^2/2k_n + f_t^2/2k_t + (M_r^2/2k_r) + (M_t^2/2k_s) - G_c$, where G_c is the fracture energy, describes contact failure once the elastic energy overcomes the fracture energy of the bond. For a contact described by a single spring-like component of stiffness k the breakage can be equivalently described by a debonding force f_c or by a fracture energy $G_c = f_c^2/2k$ with the important difference that in the latter case the effect of stiffness k is included in the yield criterion. When the contact model involves several components, according to fracture mechanics the contact rupture must be formulated in terms of the total elastic energy, which controls the propagation of cracks inside the bond, and the fracture energy G_c or toughness of the bond.

The stiffness parameters depend on the elastic moduli and geometries of the particles and the bond. Their combined effect can be modeled in two limits as parallel or serial sum of the elastic moduli. Alternatively, they can be calibrated using experimental measurements along simple strain paths. In the limit where the particles are much more rigid than the bond and the latter has a thickness h and a length L, the normal stiffness is $\simeq LE/h$ where E is the Young modulus of the bond [65]. In addition to stiffness, the force law can also involve plastic deformations and viscous terms as in the case of cohesionless contacts. Another aspect regarding bonded contacts is that breakage may occur either inside the bond or at the particle-bond surface. The strength of the bond (yield surface) may well be controlled by the adherence of the bond to the particle surface, wherein the fracture energy includes the surface energy [139, 141, 1, 80]. The formulation of solid bond in terms of a yield surface and a force law assumes that the volume of the cementing material is small compared to that of pores between particles. For larger volumes, the binding material must be described as a continuum coupled with the particles. The overall tensile strength of a cemented aggregate is a consequence of the force chains across the particles and their contacts as well as stress concentration by the pores, as in other types of porous materials, and it depends on the amount of the binding material in the pore space [139, 141, 1].

Active cohesion is mainly represented by surface adhesion induced by van der Waals or chemical interactions, with its two well-known limits: 1) DMT limit, relevant for elastically hard solids with weak or long-ranged adhesive interaction and 2) JKR limit, relevant for elastically soft solids with

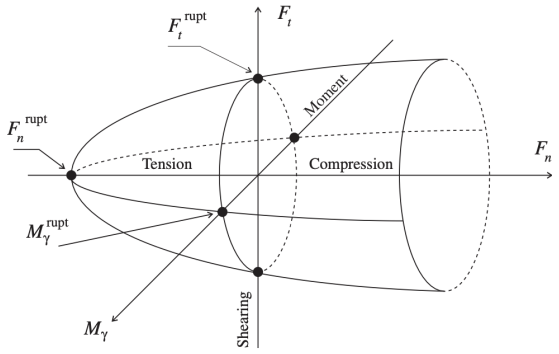

Figure 13: An example of contact yield surface in the space of contact actions between two cylinders glued by epoxy resin. Rupture occurs when the yield surface is reached along any loading path [36].

strong or short-ranged adhesive interaction [111]. For a contact between two particles of radii R, a dimensionless *Tabor number* is defined as follows:

$$\mu_T = \frac{\sigma_a}{\sigma_c} = \left(\frac{R\gamma^2}{E^2 d_c^3}\right)^{1/3} = \frac{d_T}{d_c}, \tag{23}$$

where $\gamma = \gamma_1 + \gamma_2 - \gamma_{12}$ is the work of adhesion, d_c is the decay length of the interaction potential, $\sigma_a \simeq \Delta\gamma/d_c$ is the adhesive stress, and $\sigma_c \simeq (\gamma E^2/R)^{1/3}$ is the stress in the contact region. The DMT and JKR limits correspond to $\mu_T \ll 1$ and $\mu_T \gg 1$, or, equivalently, $d_T \ll d_c$ and $d_T \gg d_c$, respectively. In the JKR limit the length d_T is of the order of the height of the neck which is formed at the contact line.

The adhesion is influenced by surface roughness: If the roughness amplitude is much larger than d_c and the solids are stiff, no macroscopic adhesion is observed between two particles. In most real surfaces, the roughness involves many length scales and therefore contacts occurs between asperities with many different radii of curvature. At low magnifications, only long-wavelength roughness is observed and the asperity radius of curvature may be macroscopic. At high magnification, nanoscale roughness prevails with asperities which may have radius of curvature in the nm range. Thus adhesion is JKR-like at long length scales and DMT-like at short length scales.

The collision dynamics of adhesive viscoelastic spherical particles has been studied and partially validated by experiments [17]. Most contact models assume that contact forces of various origins are additive. However, by considering stress distribution in the contact region, it was shown that for JKR adhesion the total force can not be expressed as a sum of elastic, adhesive and viscous forces. Indeed, a visco-adhesive cross term appears in the expression of the dissipative force and reduces dissipation [17, 138]. The JKR adhesion leads to the formation of a neck during the separation of two particles, which for rigid particles in DEM corresponds to the breakage of the contact for a positive overlap (gap). The pull-off force is $f_c = 3\pi R\gamma/2$ (vs. $2\pi R\gamma$ in DMT).

Besides the pull-off force, which depends on surface energy and particle size, surface adhesion has two major effects on the collision dynamics in a granular material:

1. Adhesive collisions are more dissipative than purely viscoelastic ones. This is reflected in the values of the normal restitution coefficient e_n. An adhesive collision is always dissipative even for massive particles. The coefficient of restitution increases with decreasing impact velocity

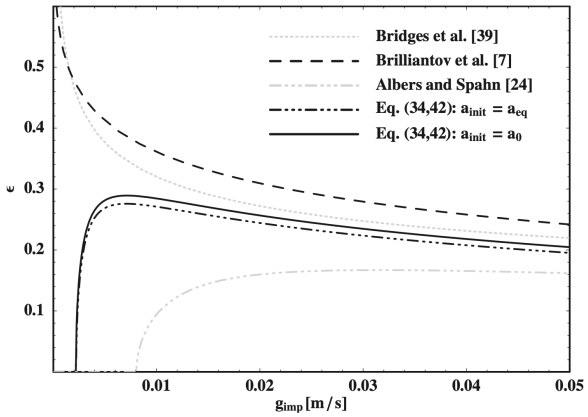

Figure 14: The coefficient of restitution as a function of impact velocity according to a visco-plastic force law with JKR adhesion. The adhesion is zero in the two upper curves and nonzero in the three lower ones [17].

until reaching a maximum value e_n^{max}. For even lower impact velocity, e_n declines rapidly and vanishes below a certain speed v_s (sticking speed); see Fig. 14.

2. Below v_s, particles stick together ($e_n = 0$) instead of bouncing. The sticking velocity increases with γ, and declines as the particle mass or the Young modulus increases. This implies that slow and small particles can aggregate in larger clusters and small particles can stick to a surface.

The three parameters f_c, e_n^{max}, and v_s are material parameters that depend on the particle mass and size, surface energy, contact stiffness, and contact viscosities.

Similar qualitative behavior is found for adhesive linear (Hookean) viscoelastic force law [99, 73]. Given the short range of van der Waals interaction, the adhesion force can be set equal to a constant force f_c:

$$f_c = \frac{HR^*}{6h_0^2}, \tag{24}$$

where h_0 is the roughness amplitude and H is the Hamaker constant. The corresponding surface energy can be evaluated by identifying this expression of f_c with the JKR pull-off force $3\pi R\gamma/2$, whence

$$\gamma = \frac{H}{9\pi h_0^2}. \tag{25}$$

The linear model leads to a simple expression of the sticking velocity [73]:

$$v_s = \frac{f_c}{\sqrt{m^* k_n}} \tilde{v}_s(\gamma), \tag{26}$$

where $\tilde{v}_s(\gamma)$ is an increasing dimensionless function of γ and m^* is the reduced mass. This equation implies a decrease of the sticking velocity with increasing stiffness and mass.

DEM Simulations show that the sticking velocity controls to a large extent the fluidization behavior of powders. In particular, the effects of adhesion force are remarkably enhanced in cases of relatively low stiffness due to a larger value of v_s. For example, in powders with a large value of surface energy, no fluidization occurs at small contact stiffness whereas full fluidization is observed for large contact stiffness [99]. In the same way, while the distribution of bubble sizes is insensitive to contact stiffness

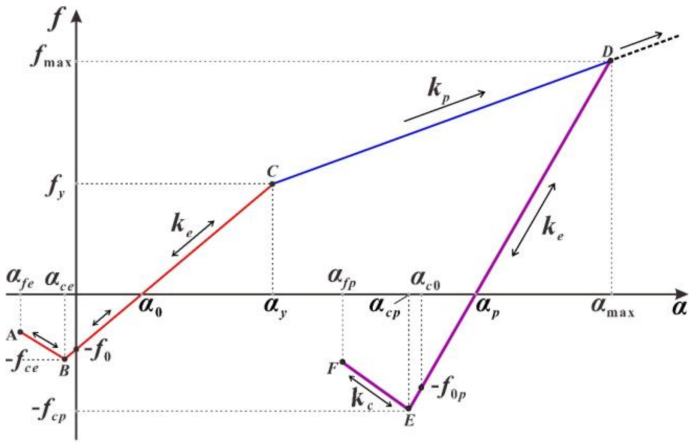

Figure 15: *Diagram of an adhesive elasto-plastic law: piece-wise linear relationship between normal force f_n (here f) and overlap $\alpha = -\delta_n$ [102].*

in the cohesionless case, it strongly depends on contact stiffness in the presence of adhesive forces. The lowering of stiffness is often used in DEM simulations to allow for larger time step. According to equation (26), for cohesive materials the adhesion force f_c must be rescaled with $\sqrt{k_n}$ to avoid the effect of stiffness on the overall behavior [55]. Note that the damping term scales in a similar fashion with stiffness. For contact viscosity $\eta = 2\alpha\sqrt{m^* k_n}$, if η is fixed, then α declines as $k_n^{-1/2}$ and e_n increases. In DEM simulations of collisional systems (granular gas), a linear model can not be calibrated to yield the experimental values of e_n^{max}, v_s and f_c at the same time unless particle density is modified.

Adhesive elasto-plastic contact laws have also been developed for application in DEM and mainly applied to binary collisions [90, 110, 102]. An example is shown in Fig. 15 [102], which is a linear model based on an elaborate nonlinear model. Such a model, albeit simplified for application in DEM, recovers most relevant properties expected from a dissipative contact as well as features that are specific to plastic contacts such as the increase of adhesion force with plastic deformation due to the increase of contact area. During the loading stage, the normal contact force f drops to $-f_0$ as soon as a contact is established. Then, it increases linearly with the normal overlap α, with a slope given by elastic stiffness k_e. During the unloading stage, the contact force is non-zero even for a gap ($\alpha < 0$) as further work is required to separate the cohesive contact. The contact breaks at α_{fe} with contact force of $-5f_{ce}/9$. If the maximum load exceeds the yield force f_y, a plastically-deformed domain is formed in the contact area, resulting in plastic deformation before the end of the loading process. Upon loading, f increases linearly with the normal overlap with a slope representing the plastic stiffness k_p. Upon unloading, f initially decreases linearly with the elastic stiffness k_e until it reaches the point E ($\alpha = \alpha_{cp}$, $f = -f_{cp}$), where the maximum pull-off force f_{cp} is obtained. Then, f increases with a stiffness k_c until it reaches the point F ($\alpha = \alpha_{fp}$, $f = -5f_{cp}/9$), where the contact is lost. The plastic deformation is memorized and during the reloading stage, the contact is re-established at $\alpha = \alpha_{c0}$ with an initial value of the force $-f_{0p}$ ($= -8f_{cp}/9$). With an increase in normal overlap during a reloading stage, the contact is initially elastic with a stiffness k_e until f reaches the point D ($\alpha = \alpha_{max}$), where the maximum normal force in previous loading stage is reached, and then plastic deformation begins with the plastic stiffness k_p. Before plastic yield (line BC), k_e is a constant and does not vary with normal overlap, but after yield k_e increases with the normal overlap as in Hertz contact.

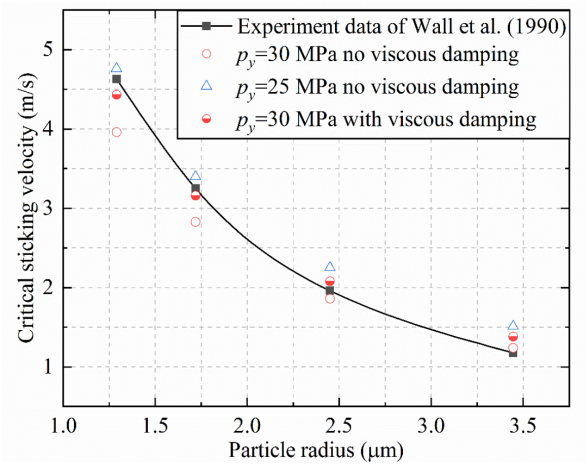

Figure 16: *Evolution of sticking velocity with particle size predicted by adhesive elasto-plastic contact model calibrated and compared with experiments for different parameter values [102].*

The key parameters of the model are the yield point (f_y, α_y), stiffness (k_e, k_c, k_p) and pull-off force (f_{cp}) and they are calibrated from the work of deformation (areas under the curve). The model predicts the coefficient of restitution as a function of impact velocity, the sticking velocity, and the evolution of adhesion with plastic deformation. As an illustration, Fig. 16 displays the sticking velocity as a function of particle radius for a system calibrated from experimental data. The sticking velocity declines with increasing size and varies with the damping parameter.

The application of elasto-plastic models to binary collisions is legitimate as the collision occurs in one time and we may assume that successive collisions do not occur at the same location on the surface of a particle, i.e. the memory of plastic deformation is not used for the new collisions of the same particle. Obviously, the memory of plastic yield is encoded at the impact points located on the surfaces of colliding particles and it does not make much sense to attribute the memory to a pair of particles without specifying the impact point. Such models can also be applied to solid bonds governed by passive cohesion since the contact point does not roll and slide unless the bond breaks. In all other cases, whenever persistent contacts roll and slide, adhesive and nonadhesive elasto-plastic models are physically unacceptable. Even in a granular gas, the memory of plastic deformations can not be objectively tracked due to collisional sticking and aggregation.

There is still a broad scope for the development of cohesive contacts in DEM. There is a lack of both rigorous and simplified models for the tangential, rolling and twisting adhesion. The calibration of adhesive linear visco-elastic models requires further work. Passive cohesion models with yield surface and plastic deformations have not been sufficiently applied for the investigation of cohesive solids. DEM simulations of wet particles (not considered here) are limited to the pendular state (binary liquid bridges). The dynamic behavior of capillary bonds (fast collisions and high shear rates) has not been considered. A dynamic liquid bridge filling model was recently developed to account for viscous flow from liquid adhering to the particles' surface into the bridge between two particles [150]. However, the distribution of liquid on the particles and their transport in the pore space and with the particles remains a huge challenge.

In CDM, adhesive contacts are simulated by allowing the normal force to take negative values on Signorini's graph down to the adhesion force $-f_c$ [120]. However, this shift alone does not predict the sticking regime, which has to be therefore implemented explicitly using the particle velocities at

the beginning of each time step. In other words, the dependence of the restitution coefficient on the impact velocity $e_n(v_n^-)$ must be explicitly built into the contact law. Such a model of adhesion has not yet been verified and validated for CDM.

2.5 Parametric randomness

For realistic simulations of a granular material not only the force laws but also the values of their parameters must be determined by means of experiments. Such measurements are generally limited in number and precision, and mean values of the parameters are estimated for use in DEM simulations [31]. However, randomness is an intrinsic feature of real-world granular materials in four respects:

1. Physical randomness: Some particle characteristics are characterized by a distribution. For example, particle fracture strength is generally well described by a Weibull distribution.

2. Particle-to-particle variability (polydispersity): The shape, size, material, and surface characteristics of the particles in a sample vary from one particle to another.

3. Surface inhomogeneity: The surface of a particle is not homogeneous and its properties (roughness, plastic state, etc) vary from one point to another.

4. Time evolution: The particle surface roughness and plastic state evolve in time either as a result of granular flow and contact histories or due to the action of chemical forces and environmental factors (humidity, precipitation, diffusion, etc).

These factors generally combine to produce a high degree of parametric randomness . For example, the adhesion force is highly dependent on the surface state and the inhomogeneity of particle surface leads also to strong variability of adhesion and restitution coefficient.

The issue is the extent to which parametric randomness impacts the collective dynamics and effective behavior of granular materials. Do monodisperse (single-valued) parameters and random or polydisperse (set-valued) parameters with distributions around those mean values lead to the same effective behavior? This issue has not yet been property addressed except for particle size distribution [146, 22]. It can be partially investigated by means of DEM simulations in which the particle or contact attributes are not equal for all particles. For example, the elastic moduli and surface roughness can be attributed from a distribution and the shear strength of a granular material can be evaluated for different values of the variance. Using the mean particle properties (single values of elastic moduli, surface roughness, etc) as input parameters despite their polydispersity assumes that a granular material is a self-averaging system. We need to analyze this effect separately for each parameter. For example, we cannot replace a polydisperse material having a broad size distribution by a monodisperse material composed of particles of the mean size determined by the same distribution. The shear strength is probably not influenced, but properties such as effective cohesion (for cohesive materials) and volume-change behavior depend on particle size distribution. Polydispersity in the shape attributes can have similar effects [104].

The polydispersity of adhesion may also strongly influence the strength of cohesive aggregates since failure properties are generally dependent on the weakest elements rather than the mean strength. For instance, a small population of strongly glued contacts inside an aggregate of weak contacts has virtually no impact on the overall cohesion of the aggregate. Regarding the friction coefficient, its polydispersity is expected to play a role in the overall behavior of a granular material in dense states because various deformation mechanisms are activated depending on the value of friction coefficient.

Typically, the contacts with a lower friction coefficient tend to slide rather than roll, decreasing thereby local dilatancy. This effect is nonlinear and its mean effect on system behavior is expected to be different from the effect of a mean friction coefficient.

Parametric polydispersity in various aspects can be measured or characterized and included in DEM despite its deterministic nature. There is essentially no difficulty in allowing the particles to carry unequal values of their attributes although it is computationally more efficient to use single parameter values for each class of particles. There is yet one issue in this respect: Many properties are contact attributes rather than particle attributes. When we use the same value of the friction coefficient for all contacts, we assume having the same type of particle. But when we have two types A and B of particles, we will have to deal with three different friction coefficients AA, BB, and AB. If the friction coefficients are generated from a distribution for N_p particles, then we need to keep in memory a table of $N_p(N_p+1)/2$ friction coefficient values. In practice, the distribution can be discretized into a lower number of classes to reduce the size of the table. This 'class representation' of polydisperse properties raises the issue of their *statistical representativity* [145, 101].

Surface inhomogeneity implies the evolution of contact attributes with time as a result of the motion of the contact point at the surface of the particles. It can be treated only if the particle surface is meshed or represented by a level set function. Then, it becomes also possible to follow the plastic deformation history at different locations of the surface of each particle. There is also no problem in allowing the particle attributes to change slowly with time. Slow variations of properties do not disturb faster collisional or inertial dynamics of the grains.

It is worth noting that physical polydispersity described in this section is an inherent *material randomness*. This must be distinguished from the aleatory or epistemic uncertainty of the monodisperse (single-valued) input parameters considered in uncertainty quantification; see section 7.3. For instance, the uncertainty in the value of friction coefficient as an input parameter of DEM simulations propagates by the numerical model to produce an uncertainty in the system response quantities such as strength or mobility. In contrast, physical polydispersity or a point-to-point randomness of friction coefficient do not propagate by the model but represent inherent input parameters of the numerical material.

3 Particle shape and contact detection

Particle shape is a primary component of realistic DEM simulations. For this reason, particle shape representation and implementation has been a hallmark of advanced DEM during the last two decades. In this section, we overview some of the major advances in this area and discuss their importance for the physics fidelity of DEM and related computational aspects.

3.1 Shape representation

A review of several methods of shape representation and contact detection can be found in [87, 44]. In most general terms and including recent developments, we can distinguish four major approaches to particle shape:

1. Meshing particle surface with polygons,
2. Clumping simple geometric primitives,
3. Analytical shape function,
4. Level-set function.

Surface meshing leads to the representation of a particle as a polyhedron. For this reason, surface meshing can also be described as *polyhedral representation* (PH-DEM). The particle shape in this representation ranges from simple regular and irregular polyhedra to arbitrary shapes with a large number of facets [6, 8, 116, 14, 40, 87, 46]; see Fig. 17. PH-DEM is particularly interesting since realistic particle shapes can be obtained by means of 3D shape digitalization technologies such as laser and computed tomography scanning. The acquired 3D shape is represented either as a discrete pixel/voxel cloud or a polygonal/triangular surface mesh. Two examples are shown in Figs. 18 and 19. Polyhedral particles can also be smoothed by means of Minkowski sum with a sphere of desired radius to reduce or remove surface roughness.

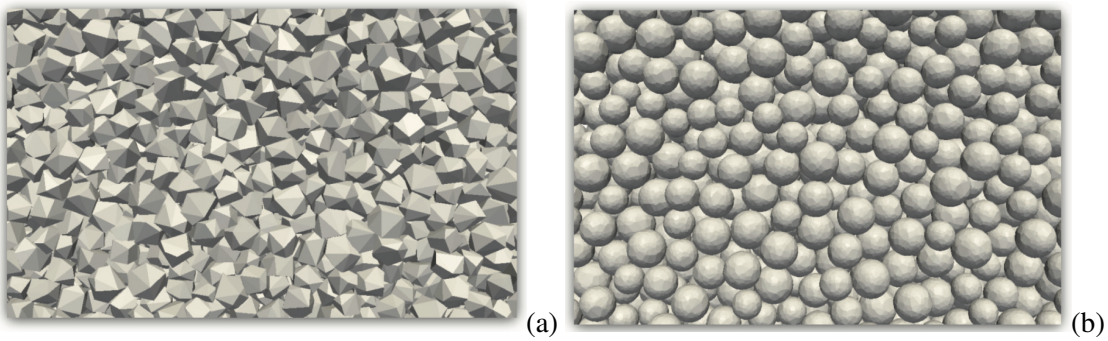
(a) (b)

Figure 17: *Snapshot of packings composed of irregular polyhedral particles of (a) 20 and (b) 596 faces [8].*

Clumping of spherical particles with or without overlaps to match complex shapes is known as *multi-sphere representation* (MS-DEM). It is straightforward and technically simple since the contacts can be detected and modeled using established sphere-sphere interactions although the computational load increases with the number of spheres. Arbitrary shapes can be built with the exclusion of sharp

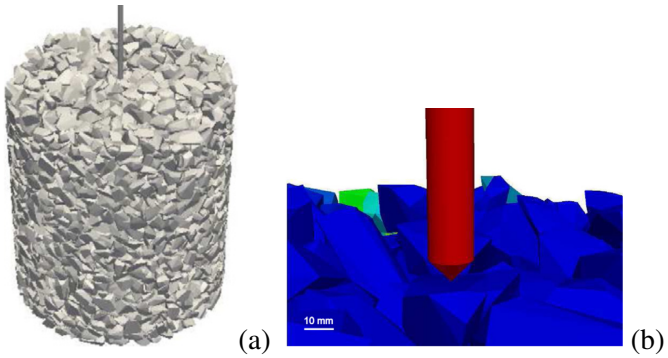

(a) (b)

Figure 18: *Assembly of 5900 ballast particles built from a library of 1000 digitalized ballast partile shapes (a); Penetration test (b) [117].*

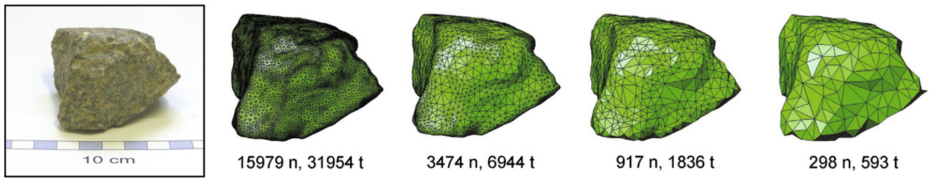

Figure 19: *Digital photograph of a granite aggregate particle and three examples of meshed representations with increasing coarseness as a function of the numbers n and t of the nodes and triangles, respectively [79].*

edges. Fast methods have been proposed to create irregular particle shapes for DEM [48]; see Fig. 20. However, overlapping spheres imply a non-uniform density inside the particles, leading to incorrect moments of inertia. Methods have been proposed to mitigate such errors. Other examples of geometric primitives that can be clumped to obtain complex shapes are points, segments, triangles, cylinders, and other simple analytical shapes. Fig. 21 shows an example of the representation of a particle as a clump of cylinders, polygons, and spheres. Particle surface can be represented as a cloud of points and other geometric primitives can be associated with these points. In fact, a polyhedral-shaped particle can also be described as a clump of polygons. The choice of the geometric primitive depends on the contact detection strategy and force laws.

Analytical representations are smooth surface functions. Examples are ellipsoids, super-ellipsoids, poly-ellipsoids, poly-superellipsoids, Fourrier series (FS) and spherical harmonics (SH). Fig. 22 shows an example of a rock particle obtained in meshed form from 3D laser scanning and represented

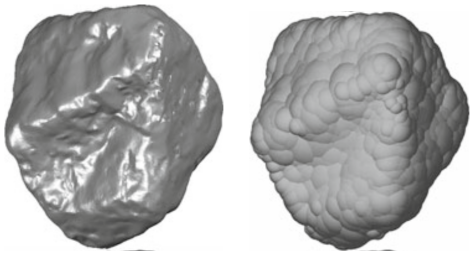

Figure 20: *Two multi-sphere clumps with low and high resolution [48].*

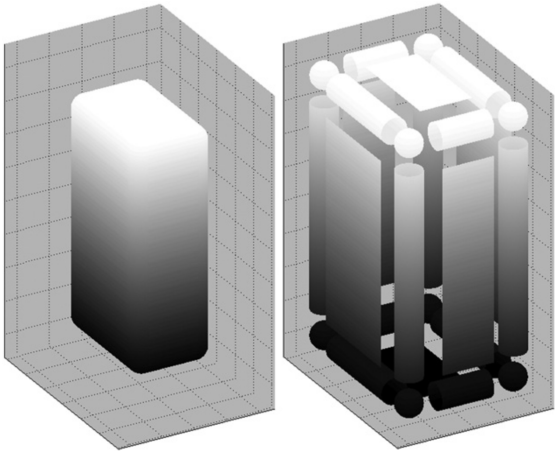

Figure 21: *A brick modeled as a clump of spheres, cylinders and rectangles [126].*

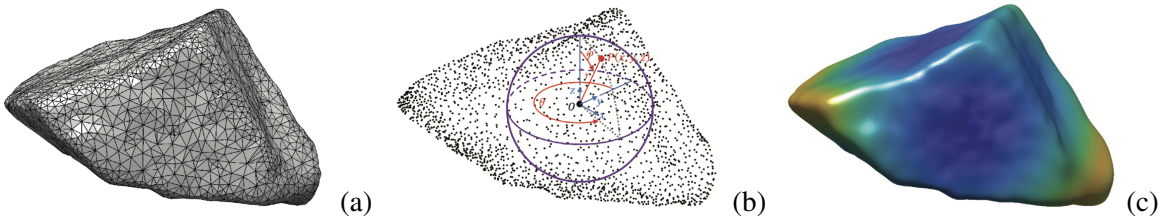

Figure 22: *(a) Triangular mesh model of a rock particle obtained by means of 3D laser scanning, (b) transformation of discrete surface vertices from Cartesian coordinates to spherical coordinates, and (c) continuous representation of the discrete particle surface using spherical harmonic function [147].*

by a spherical harmonic function [147]. Fig. 23 shows examples of superellipsoids and polysuperellipsoids [158]. When using analytical shapes, contact detection and resolution can be based either on continuous function representation or discrete function representation by discretizing the surface function into a number of points [86].

Level-set representation of particle surface relies on a signed distance function that returns the shortest distance to the surface of the particle. The zero level is the particle surface [71]. This function is actually defined in a discrete fashion, storing its values on a cartesian grid; see Fig. 24. This discrete distance field endows this method with a great versatility to mimic real shapes. This information is stored in computer memory and provides the geometric basis of contact detection and resolution. The mass, center of mass and moment of inertia can be readily calculated from the level set function. The contacts between particles are calculated by seeding a number of nodes into the surface and using a node-to-surface algorithm to calculate the distance.

3.2 Contact detection

Contact detection consumes most of the simulation time in DEM. Fig. 25 shows an example of the proportion of computation time for each DEM function during a packing simulation. We see that more than 70% of the total simulation time is used for contact detection. Together with neighbor search and contact update, contact-related computation takes more than 90% of the simulation time in

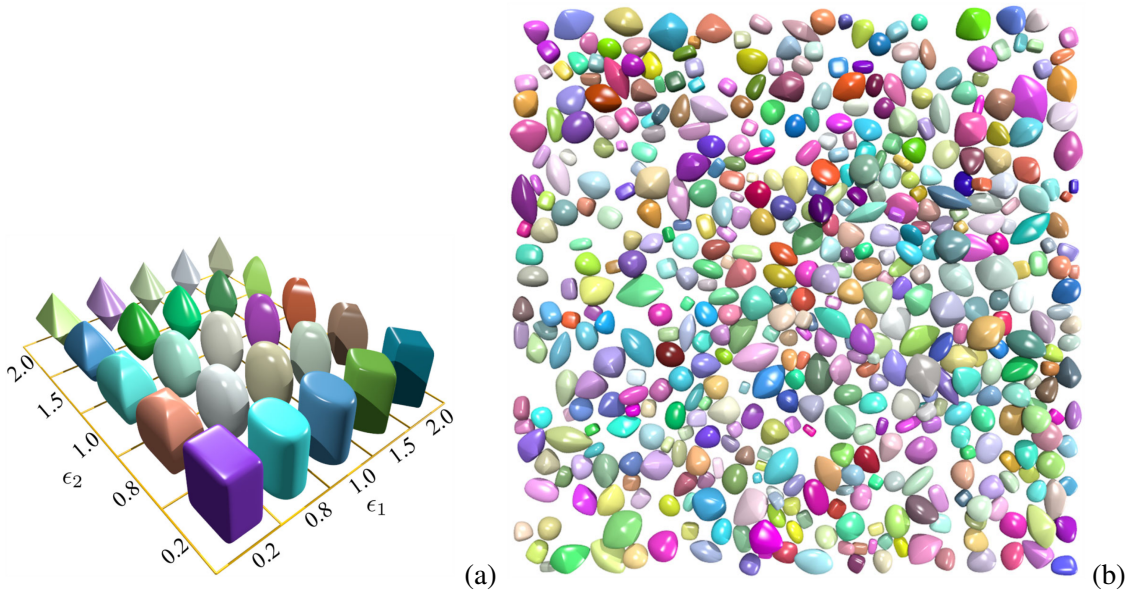

Figure 23: *(a) Examples of superellipsoids with a range of their shape parameters; (b) examples of poly-superellipsoids with random values of shape parameters [158].*

DEM [109]. Different schemes have been developed for efficient contact detection and resolution with different shape representations [14, 47, 45]. Contact resolution determines the geometric attributes of the contacts, including the contact overlap, area, and volume, normal direction, and contact point (needed as the point of application of the contact force).

The task of contact detection can be cast as a standard problem in the field of convex optimization [14]. The intersection between a pair of particles is obtained by solving a linear program and the analytic center of the linear inequalities defines the contact point. Clumped particles have the advantage of requiring low computational cost for contact detection between two primitives (more specifically when an analytical solution exists), but a large number of pairs of primitives are involved in contact detection between two particles. Nevertheless, efficient procedures can be set up to sort both particles and their primitives by means of appropriate bounding boxes (broad phase and narrow phase sorting). Genuine methods exist also for parallel computing by optimizing the data structure or by adapting the implementation to the GPU [109, 53].

In contrast to point contacts between simple analytical shapes such as spheres and ellipsoids, the features of a contact region between two aspherical shapes depends on both particle shape and its representation. For example, the contact region between two intersecting polyhedral particles is a small polyhedron to which a single contact point is often attributed together with its normal direction, volume, and surface, which are used to define the force laws. However, there are several contact types between two polyhedra: vertex-face, edge-edge, edge-face, face-face…; see Fig. 26. Thus, contact detection must also determine the contact type. The unilateral constraints associated with these contact types have not the same nature. A face-face contact is a plane that needs at least three points for its definition. Therefore, a face-face contact is equivalent to three simple contacts or unilateral constraints [121, 8]. This means that at least three contact points are necessary to represent the contact. In a similar vein, an edge-face contact needs at least two points. For this reason, edge-face and face-face contacts can be described as *double contact* and *triple contact*, respectively, whereas all other contact types are *simple contacts*. The double and triple contacts are 'natural' multiple contacts. Multiple

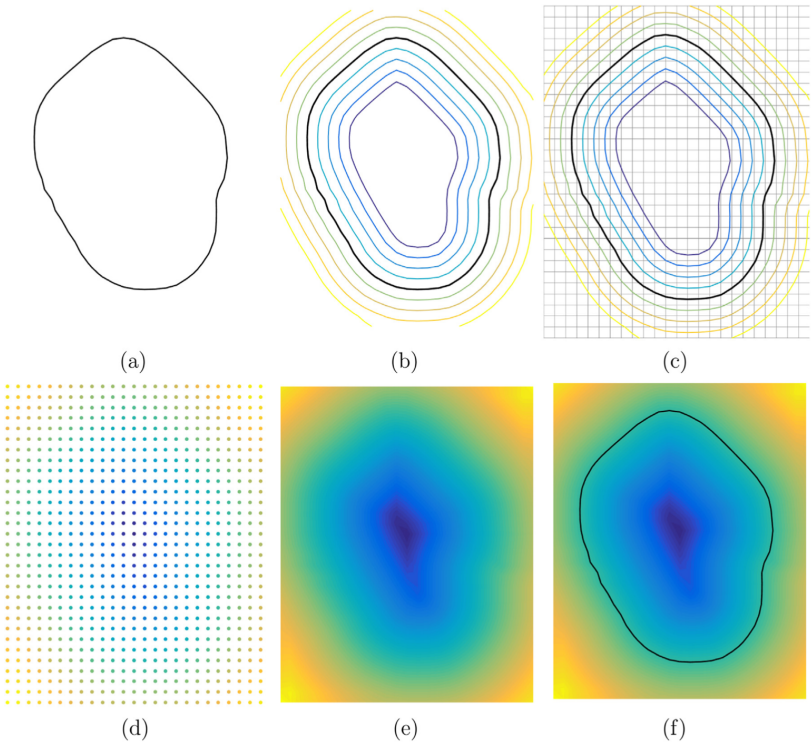

Figure 24: *Illustration of a level set function. (a) Grain particle surface. (b) Contour lines representing signed distance from surface. (c) Superimposition on grid. (d) Discretized level set function. (e) Level set function with interpolation between grid points. (f) Reconstruction of original grain surface via interpolation [70].*

contacts can also occur between sphere clumps but they are not always natural and reflect rather the clumped representation of the particle.

Complex particle shapes have often been used with unrealistic force laws, which in contrast to spherical particles cannot be calibrated through binary collisions. Binary collisions between polyhedral particles, for example, would be experimentally difficult to carry out. Very often, the normal force between polyhedral particles is assumed to be proportional to the intersecting volume. This choice is algorithmically justified but has no experimental counterpart [46]. For polyhedral particles, the force law depends on the contact type. The elastic force-displacement relation for an edge-edge contact is different from that of a face-face or vertex-face contact. For smooth analytical surfaces, the Hertz law can be used with the local radius of curvature, but the radius changes from one contact point to another. Nevertheless, the contact forces scale with the confining pressure and the main function of force laws in DEM is to penalize overlaps, on the one hand, and damp elastic waves, on the other hand. Only the overlaps are influenced by the choice of force law and their values are not significant in cohesionless granular flows. However, the behavior of cohesive granular materials depends on the contact stiffness and the overlap [100, 94].

Hence, except in fully volume-controlled shearing, where the values of contact forces depend on the choice of the force law and contact stiffness, a simple linear law based on the contact overlap or volume is not unreasonable.These contact laws must, however, satisfy two condtions: 1) The simple, double, and tripe contacts must be distinguished. Otherwise, particle rotations are not correctly cal-

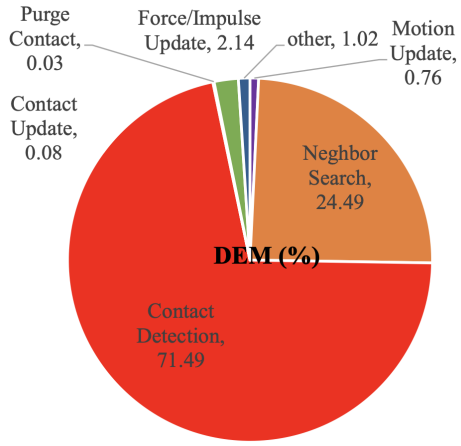

Figure 25: *Computational time for each function in DEM [109].*

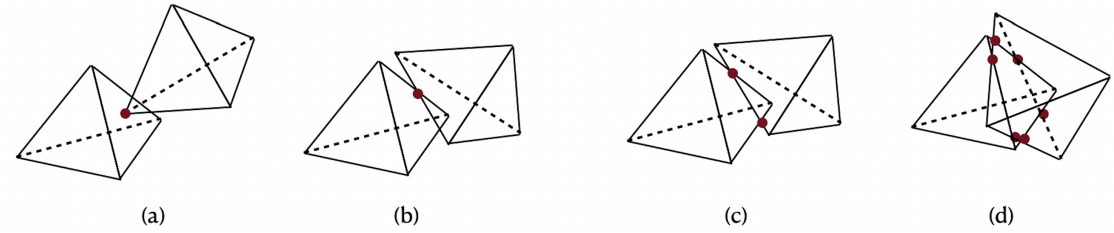

Figure 26: *Various contact types between two polyhedra: (a) and (b) simple contacts, (c) double contact, and (d) triple contact.*

culated; 2) The contact laws must be energetically consistent in the sense that elastic energy must be conserved for arbitrary relative motion between two particles in a closed loop [46, 46]. In CDM, at least three contact points are attributed to each face-face contact and at least two contact points to each edge-face contact [107, 8]. These points must be placed such that their convex hull includes the shared surface. The Signorini and Coulomb constraints are applied to each point. The contact force is the vectorial sum of the forces and their point of application is the barycenter of forces. One advantage of CDM is that, up to the identification of multiple contacts, the contact laws are independent of particle shape.

The reported simulations of realistic particle shapes with simple force laws seem to capture well the interactions of complex particle shapes in various implementations reported in the literature. Fig. 27 shows two examples of assemblies of meshed complex-shaped particles. Fig. 28 shows an assembly of particles simulated by Level-Set DEM (LS-DEM) [70]. These simulations require high computer memory and grid-resolution. Multi-sphere clumps, smooth polyhedra, and superellipsoids were compared for the same shapes, and the results for hopper flow were found to be identical for each shape and not sensitive to the details of shape representation [62]. This finding does not, however, imply that the three shape representations are equivalent in all respects but seem to indicate that particle dynamics under certain circumstances is more sensitive to general shape descriptors such as elongation and sphericity than to higher-order details of particle surface.

In fact, in all non-analytical methods of shape representation, the particle surface has some degree of bumpiness or roughness, which must be trade off with computational efficiency. In polyhedral

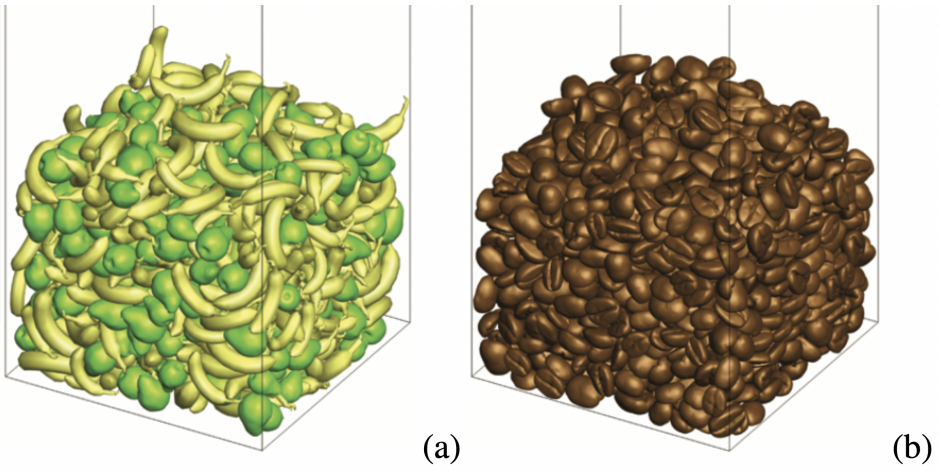

Figure 27: *Snapshots of randomly-deposited meshed complex-shaped particles simulated by PH-DEM [47].*

shape representation, the roughness depends on the inter-vertex distance. Even very small surface angularity can impact the overall behavior of granular flows. For example, as shown in Fig. 29, during triaxial compression, an assembly of irregular polyhedra made of 596 faces develops a shear strength and dilatancy that is considerably higher than that of analytical spheres [8]. It seems plausible to assume that sensitivity to shape resolution declines as packing fraction decreases. However, this point has not been checked and other mechanisms related to particle rotations and collisions may lead to high resolution-sensitive results even at lower packing fraction. Such pitfalls can be avoided by using a Minkowski sum with a radius equal to the inter-vertex distance to remove the surface roughness [45]. This is absolutely necessary when polyhedral representation is used to model smooth convex particles (and not to simulate real polyhedral particles) with adhesive forces since multiple contacts at face-face and face-edge contacts induce torque transmission. The torque is of the order of the normal force multiplied by the inter-vertex distance. It has a nonzero value when one of the forces acting on a face is tensile.

Similar considerations apply also to clumps of spherical particles. Several studies have shown that the artificial bumpiness of the surface affects granular flows [72, 11]. Furthermore, artificial multiple contact points lead to inaccurate force calculations such as overdamping and over-stiffness. With the Hertz force law, underdamping can occur, too. Several solutions have been proposed to mitigate those problems. In particular, using the largest normal force (instead of the total force or average force) to represent the force generated at a contact with multiple points happens to fixe the problems of over-stiffness and over-damping [11]. Such a procedure should not be applied to natural multiple contact points such as face-face contacts. It is therefore necessary to carefully distinguish the nature of multiple contacts. Torque transmission is another issue that is also fixed by using the maximum normal force. Finite resolution of particle shape in LS-DEM poses similar issues [38].

We see that computational modeling of particle shape has many different aspects with a broad scope of potential numerical developments and research in near future. The notion of contact and force laws need to be revisited. If it is admitted that linear force laws with contact variables that bear no experimental counterpart (such as contact volume) are adequate for complex realistic shapes, then the issues of calibration with binary collisions and sophisticated contact mechanics models developed for spherical particles must be reconsidered.

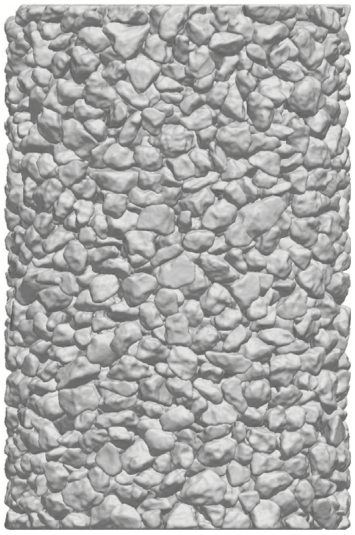

Figure 28: *Compacted assembly of realistic particle shapes simulated by LS-DEM [70].*

3.3 Shape polydispersity

For modeling real-world granular materials, it is necessary to distinguish particle shapes which can be defined through a few shape parameters from partially irregular and assymetric particle shapes that require in principle a large number of parameters. For example, the poly-superellipsoids can have a variety of shapes as displayed in Fig. 23. But, this variety of shapes is generated by tuning only 8 parameters [158]. In contrast, a real grain shape such as that shown in Fig. 22 requires either a large number of vertices as a polyhedral particle or a large number of spherical harmonic terms as an analytical particle. When a cutoff is introduced in the spherical harmonic expansion, we assume some degree of randomness or error in modeling the shape of a single grain. However, the particle-to-particle variability or polydispersity in a granular sample can be higher than the approximation error in the shape representation of each particle.

This stochastic feature of real shapes is a major ingredient of the construction of a realistic sample of particles. In fact, *shape polydispersity in a granular material is a shape parameter* at the sample scale. This concept was applied, for example, to packings of pentagons in 2D [104]. The angular positions θ^i of the five vertices i of the pentagons were defined as

$$\theta^i = \theta_0 + \frac{2\pi}{5} i \pm \delta \frac{\pi}{5} \mathbf{1}, \tag{27}$$

where $\mathbf{1}$ is a random number in the range $[0,1]$, and the parameter δ can be varied between 0 and 1. δ represents shape polydispersity or shape variability; see Fig. 30. It was found that the packing fraction increases with both size and shape polydispersity, but the effect of shape variability for all the investigated structural properties is significant only at low size polydispersity where the short-range positional and/or orientational ordering of the particles prevail.

The issue of the amount of information encoded in particle shape touches also on the theoretical modeling of granular flows. We can perform numerical simulations and establish multi-variate correlations between the flow behavior and particle shape descriptors. How many shape parameters will be necessary to exhaust all correlations? The most robust correlations involve sphericity (deviation from a spherical shape), roundness, elongation, and convexity. Although there are many other shape

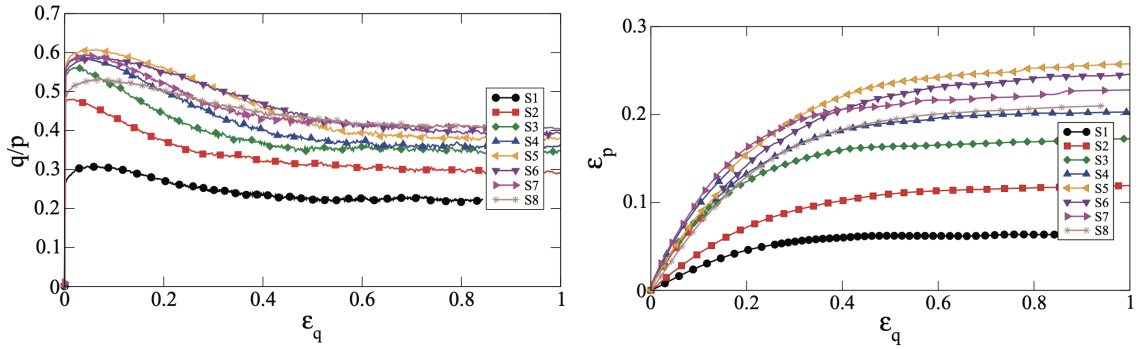

Figure 29: *(a) The evolution of stress ratio q/p, where $q = (\sigma_1 - \sigma 3)/3$ is the stress deviator and $p = (\sigma_1 + \sigma_2 + \sigma_3)/3$ is the average pressure as a function of shear strain ε_q, and (b) The evolution of volumetric strain ε_p as a function of ε_q in triaxial compression of an assembly of irregular polyhedral particles with decreasing numbers of faces. S1: analytical spheres, S2: 596 faces, S3: 176 faces, S4: 96 faces, S5: 46 faces, S6: 30 faces, S7: 20 faces, and S8: 8 faces [8].*

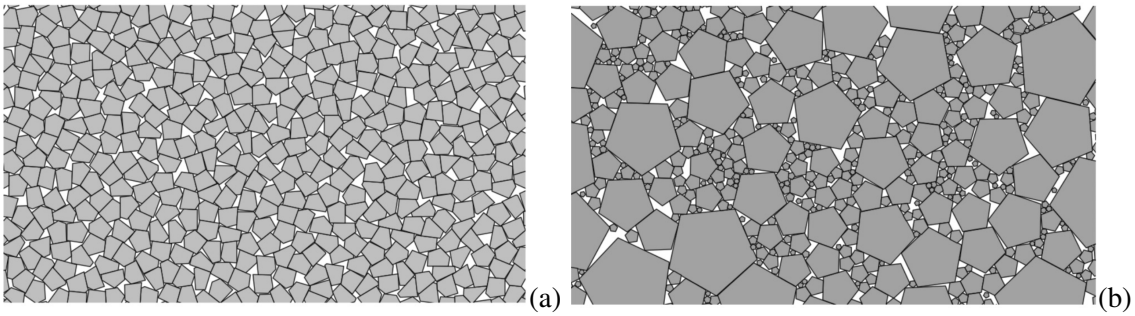

Figure 30: *(a) High shape variability $\delta = 1$ and low size polydispersity versus (b) Low shape variability $\delta = 0$ and high size polydispersity [104].*

descriptors, a combination of a few shape parameters may provide a satisfactory solution. The residual variability due to the less influent parameters can then be attributed to shape randomness. This expectation corresponds to the conventional wisdom, which suggests that the effect of some shape parameters average out due to disorder and dynamic particle fluctuations and only robust shape features scale up to the flow behavior. It seems therefore plausible to replace real particles by 'average' particles described by only a few parameters together with a shape variability or shape polydispersity parameter. It is noteworthy that, if a few shape parameters can robustly account for all shape effects, then refined shape representations in DEM will not be necessary! This is, however, only a speculation at this stage, and DEM is actually the ideal tool to investigate this issue and, to this end, high-fidelity shape representations and contact detection methods are needed.

A simple physical method for reducing the particle shape parameters to a single meaningful parameter is to relate the shape to particle dynamics. For example, it has been speculated for a long time that rolling friction can mimic the effects of aspherical shape. Rolling friction is a torque M that can be mobilized at a contact between two particles up to a maximum value $M_{max} = \mu_r \ell f_n$, where ℓ is the branch vector length joining the centers of two articles and μ_r is the rolling friction coefficient [15]. The rationale behind this hypothesis is that particle rotations are governed by tangential forces in the case of spherical or circular particles whereas in a packing of aspherical particles the normal forces

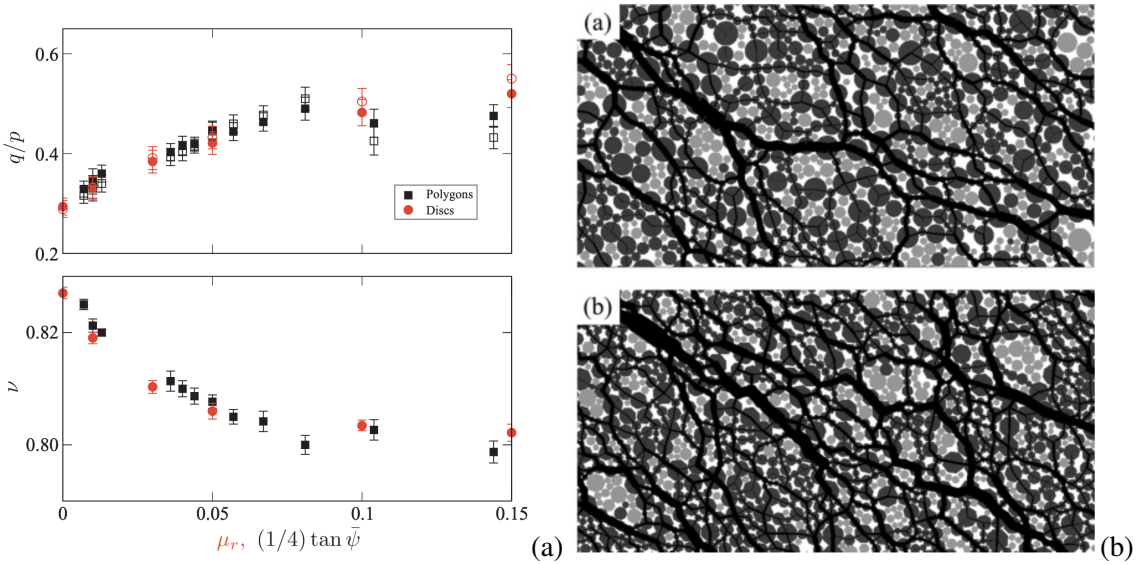

Figure 31: *(a) Stress ratio q/p and packing fraction ν in the steady shear state plotted as a function of rolling friction μ_r for disk packings and $(1/4)\tan(\pi/2n_s)$, where n_s in the number of sides, for polygon packings. (b) Force chains in the two packings for $\mu_r = 0.05$. [41].*

can also exert a nonzero moment to the particle centers of mass hindering thereby particle rotations. In simple terms, the hypothesis is that aspherical shapes introduce an angular hindrance effect that can be mimicked by rolling resistance in DEM simulations of spherical particles.

This hypothesis was rigorously checked in 2D by comparing the quasi-static rheology of assemblies composed of polygonal particles with variable number of sides with that of assemblies composed of disks with variable rolling friction [41]. By comparing DEM simulations of quasistatic shear flows of both types, it was found that, not only the shear strength and packing fraction but also the fabric and force anisotropies and the probability distribution of forces were almost identical when a packing of polygons with n_s sides was compared with a packing of disks with rolling friction $\mu_r = (1/4)\tan(\pi/2n_s)$; see Fig. 31. This mapping was obtained by requiring that the amount of energy dissipated between two particles per unit relative rotation is equal for the types of particles (assuming that the effective coefficient of restitution is zero). For large values of n_s, the equivalent rolling friction coefficient decreases slowly (as $1/n_s$). These findings suggest that rolling friction can indeed be used as a shape parameter for quasi-static flows. This mapping needs, however, to be checked in 3D, for higher inertia, and for various particle shapes. This example raises also the interesting issue of the relation between particle shape and dissipation, which has not yet been addressed on a systematic basis.

4 Breakable particles

Particle breakage with its distinct variants (attrition, chipping, erosion...) is still a huge challenge for realistic DEM simulations since it requires a model of solid particles that can break into statistically representative size classes and arbitrary shapes of fragments.

Three different modeling strategies are possible for particle fragmentation:

A Sub-particle level

1 Bonded Particle Method (BPM): Each particle is represented as a cluster of primary rigid particles linked together via bonds endowed with a yield criterion.

2 Hybrid and continuum approaches: Each particle is modeled as a discretized continuum with cohesive zones or bonds which can break and finite elements that can transform into discrete elements.

B Particle level or Particle Replacement Method (PRM): Each particle is instantaneously replaced by a collection of smaller particles whenever the energy absorbed by the particle exceeds the fracture energy of the particle.

4.1 Sub-particle models

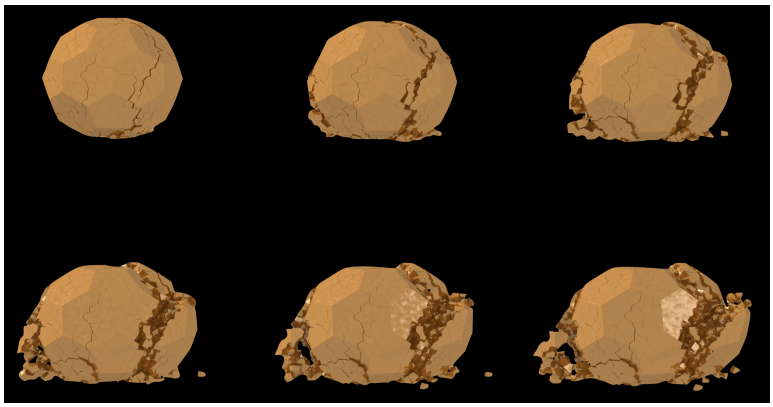

Figure 32: *Breakage of a particle impacting a rigid wall, simulated by Bonded Cell Method (BCM) [107].*

In A1, the primary particles can be spheres or polyhedra although mostly spherical primary particles have been used. A parent particle (cluster) can break to produce smaller clusters which represent its progeny; see Fig. 32. The parent particle (cluster) and the resulting fragments can have arbitrary shapes and sizes (down to the primary particle size) even when the primary particles are spherical. This simple extension of DEM for modeling particle fragmentation is known as Bonded Particle Method (BPM) and it has been used to simulate milling processes and other phenomena involving particle breakage. It is still widely used owing to its simple and flexible algorithm specially with spherical primary particles [156]; see Fig. 33 for a recent example.

The clusters composed of spherical particles are porous aggregates. If the external boundary of a cluster is used to represent the particle surface, then the total initial volume is not conserved. In

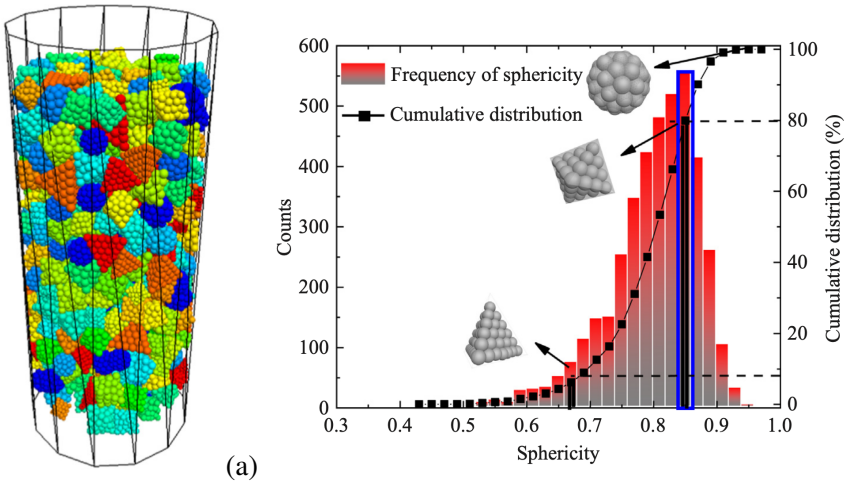

Figure 33: *(a) A sample of breakable particles of different shapes simulated by the Bonded Particle Method (BPM); (b) The cumulative distribution of shape sphericity obtained from the reference material and three model shapes with their sphericity values and frequencies [156].*

contrast, the primary polyhedra can fill the volume of a particle and no volume is lost during particle breakage. Another difference is that in a cluster of spheres the bonds are located at the contact points between primary particles and thus no natural fracture surface is associated with a broken bond although it can be defined. In clusters of polyhedra, the bonds coincide with the common surfaces between polyhedra, as shown in Fig. 34. Therefore, the breakage of a bond naturally creates a fracture surface. We distinguish the two types of clusters by referring as Bonded Cell Method (BCM) to the clustering of polyhedra. In BCM, each face-face link represents a potential crack and the fracture energy G_f is obtained by multiplying the area by surface energy [107]. More generally, depending on the material, the bonds can obey a yield criterion as those discussed in relation to passive irreversible cohesion in section 2.4. In particular, beam-like links between primary particles have been used to control the fracture modes at the interface between particles.

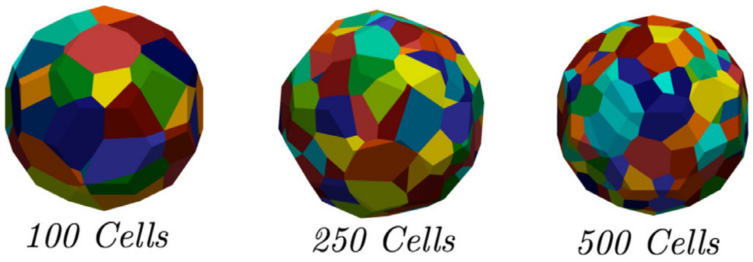

Figure 34: *Clusters of bonded polyhedra obtained by Voronoi tessellation of an icosahedron [107].*

There are several key issues related to the realism and efficiency of BPM. The first point is the high computational cost of BPM. The clusters (both parent particle and its progeny) can not represent realistic particles and give rise to fragments of arbitrary shape and a meaningful range of sizes unless they contain a large number of primary particles. The computational cost of a DEM simulation of just 10^3 particles each composed of 10^3 primary particles is the same as that of a sample of 10^6 particles. This huge cost implies that optimized DEM codes and high performance computing is necessary to

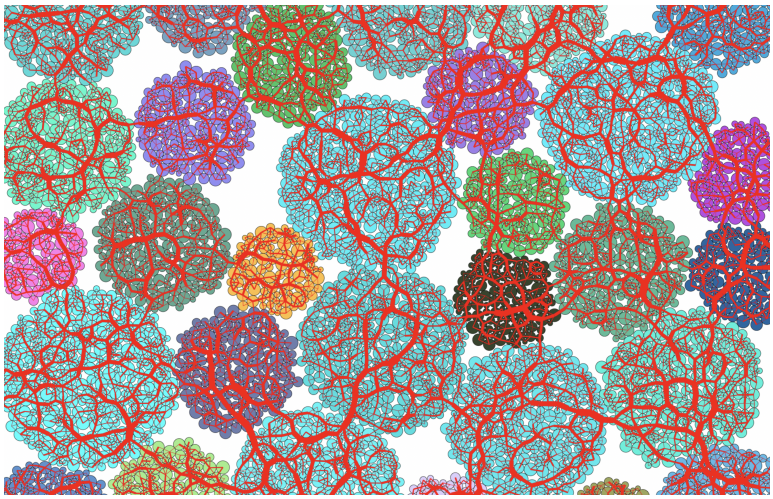

Figure 35: *Force chains in a packing of breakable particles according to BPM.*

ensure the statistical representativity of the fragments and their size and shape distributions. Note also that the size ratio between a parent cluster of 1000 primary particles and the primary particle is only 10. If the lower bound for the number of primary particles in the smallest cluster is set to 100 to avoid finite size effects, then the size reduction factor is only about 2. This means that, in a milling process for example, the early stages of comminution can be correctly simulated, but as the particle sizes are reduced, the size effects will increasingly bias the results. Fig. 36 shows an example of BCM simulations with pentagonal particles in a biaxial compression test [105]. We see that various phenomena such as particle shattering, surface breakage, damage without breakage... are well captured by the simulation but the fragment shapes after shattering are mainly controlled by the initial Voronoi tessellation.

The second point is whether a cluster can be used as a model of solid particles, which can have elasto-plastic behavior and undergo brittle or ductile fracture. Since the primary particles are bonded inside a cluster, the overall mechanical behavior of the cluster is directly controlled by that of the bonds. For example, the elastic moduli of a cluster depend on the normal contact stiffness, the average distance between primary particles, the density of bonds per unit volume, the ratio of the tangential and normal stiffnesses, and the anisotropy of the bond network. The values of the moduli cannot be exactly predicted by Effective Medium Theory because of the nonaffine displacement fields in a granular material but they can be measured by means of simple tests [74]. On the other hand, the fracture toughness of the particle depends on the debonding energy and porosity of the cluster. Finally, the strength of the cluster depends on the debonding force or yield surface, and its variability is well described by the Weibull distribution function with parameters that can be varied by adding defects in the cluster [13]. A parametric study shows that, a particle must contain at least 100 primary particles to avoid finite size effects in the particle strength [21]. Note also that, if the simulated material is not composed of particles that have a textured structure, such as layered or crystalline structure, the fragments will have shapes controlled only by the applied stress. This implies that the arrangement of particles inside the cluster must be isotropic and random or explicitly account for the texture of the real particles.

However, even with calibrated elasto-plastic parameters and toughness, the granular structure of a cluster shows up in the inhomogeneous transmission of stresses and nonaffine particle displacements,

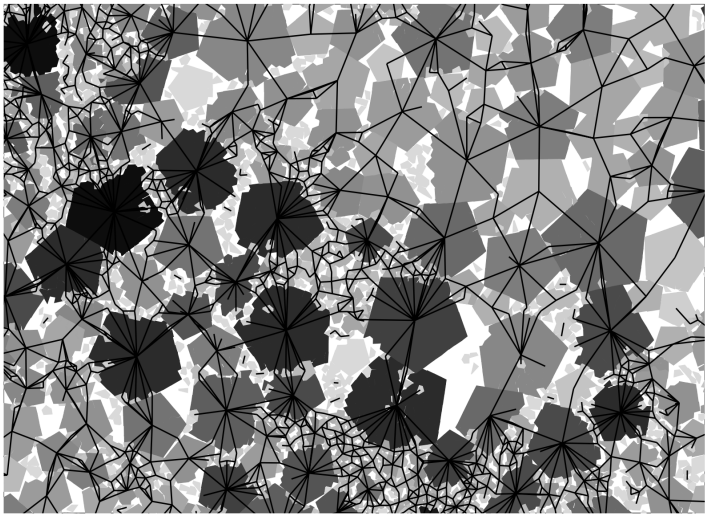

Figure 36: *Particle fragmentation in a packing of breakable pentagonal particles simulated by BCM. The lines join the centers of touching particles [105].*

which are important for the initiation and propagation of the cracks. Fig. 35 shows an example of forces in a packing of particles modeled using BPM. We can discern the force gradients inside each cluster induced by its boundary forces but they are convoluted with granular disorder and force chains. Since the clusters are expected to represent solid particles, it is more appropriate to use the local stress tensor calculated over a 'process zone' centered on a bond. A large enough number of primary particles is needed to smooth the stress field and integrate out the force chains. The concept of a 'horizon' is used for the same reason in the peridynamics method, which is a continuum approach [160, 13].

Another key point concerns the shapes of the generated fragments. In fact, the issues discussed in section 3 regarding the effects of surface roughness of the particles apply to the fragments. The surface roughness can strongly impact crack propagation and particle dynamics in the intense breakage zones. However, there is a trend to undermine force laws when dealing with particle shape and to undermine particle shape when dealing with particle breakage! This is imposed by the complexity of the problem and current computational limitations.

What one should expect from BPM is primarily the fracture behavior of a single particle in terms of strength, fracture modes, and the distribution of fragment sizes, shapes, and energies depending on the stressing energy. In experiments, mostly impact tests and diametral compression tests have been considered whilst a particle inside a granular material can break under the action of several contact forces [135]. The BPM simulations have only been partially fit to the experiments and theoretical models proposed. For example, Fig. 37(a) shows that fragment size distribution of calibrated BPM-DEM simulations poorly describes particle breakage in impact tests [67]. The problem seems to be related to finite size effects. The smallest fragment size and shape must be distinguished from the primary particle size and shape. The smallest fragment size must contain a sufficient number (at least 100) primary particles for its shape to be different from that of the primary particles and its strength properties to be well defined.

The continuum and hybrid approaches (A2) have the advantage of resolving the stress field inside each particle more accurately than BPM. The particle is discretized into finite elements which are

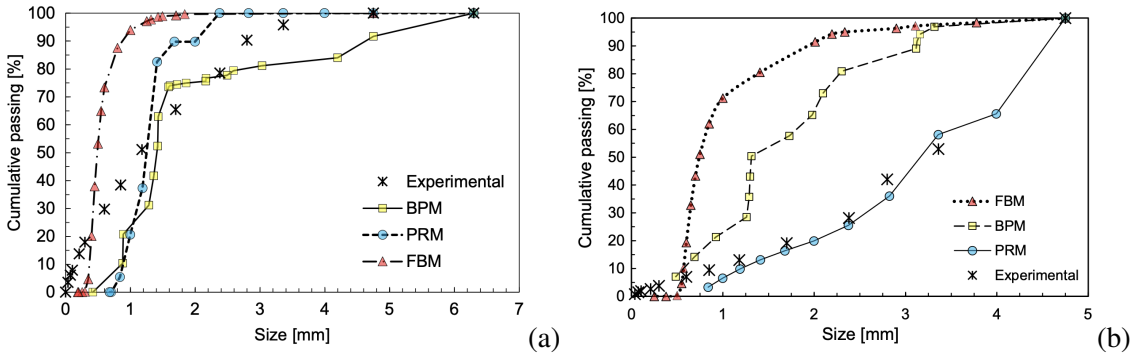

Figure 37: *(a) Comparison of the experimental and simulated progeny size distributions from impact of single copper ore particles contained in the size 6.7–4.75 mm at an impact energy of 3 J using; (b) Comparison between experimental and predicted size distributions broken out of the narrow size for a monolayer configuration from impact of a ball at an energy of 3 J on copper ore particles [67].*

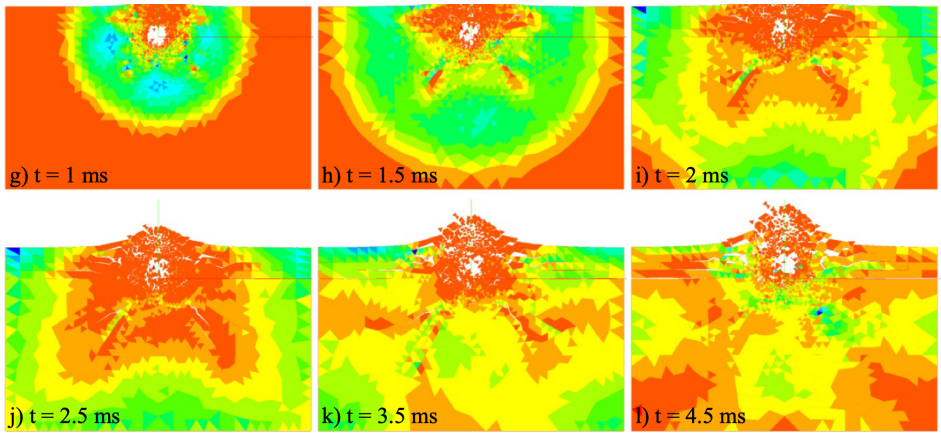

Figure 38: *Simulation of rock blast by a hybrid finite-discrete method. Color code represents vertical pressure [2].*

bonded together by joint elements. The joint between two finite elements fails according to a fracture criterion. The contacts between meshed particles can be modeled using either Lagrange multipliers or a penalty method. In the hybrid approach, when a joint breaks, the two finite elements transform into discrete (rigid) elements. In this scenario, the fragmentation is a consequence of the coalescence of the cracks across the particle [2]. Un example of hybrid finite-discrete element simulations of rock blast is displayed in Fig. 38.

Finite elements can be replaced by lattice elements or peridynamics. The Lattice Element Method (LEM) is based on the discretization of different phases of a solid on a regular or irregular lattice [144, 140, 1]. Hence, the space is represented by a grid of points (nodes) interconnected by one-dimensional elements (bonds); see Fig. 39(a). Each bond can transfer normal force, shear force and bending moment up to a threshold in force or energy, representing the cohesion of the phase or its interface with another phase. In its simplest version, the elements are linear springs characterized by a Hooke constant and a breaking threshold. Each bulk phase (particle, matrix, pores) or surface phase (interface between two bulk phases) is materialized by the bonds carrying the properties of that phase. Fig. 39(b)(c) shows examples of fracture of a 2D cemented granular material. The computational cost

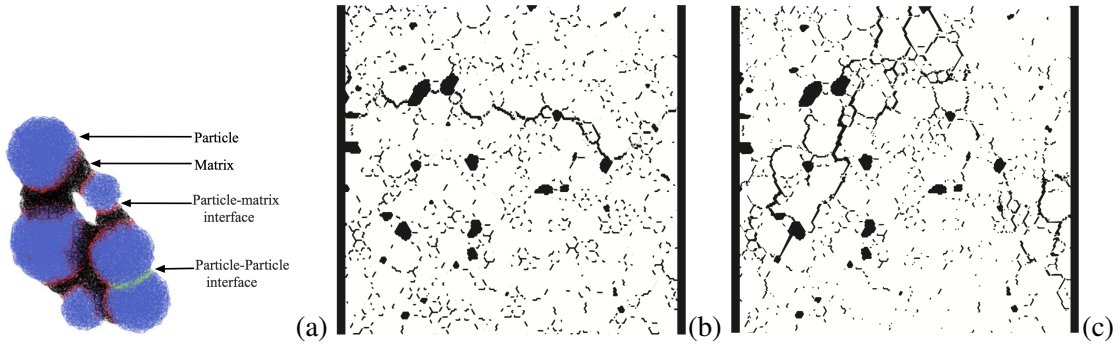

Figure 39: *Schema of lattice elements in LEM; Breakage of a cementer granular material in tension and in compression [140, 1].*

of LEM is generally low but substantially increases when the fragmentation of particles continues and the contact detection procedures are to be applied to the particles. LEM is therefore efficient for the initiation of fracture.

In the peridynamics method, the material is represented as a network of interacting nodes governed by a nonlocal (integral) formulation of the equations of dynamics inside a given 'horizon' [49]. Bond rupture events lead to damage or to fracture when a critical number of bonds is damaged. Peridynamics is computationally efficient and well suited to handle crack nucleation and propagation. Fig. 40 shows the fracture of a single particle under the action of diametral compression repeated for a random distribution of pre-cracks inside the particle.

As in the case of LEM, peridynamics can be used for continuous breakage if it is hybridized with DEM. In a hybrid approach, the breakage of individual particles is analyzed by peridynamics simulation of the particles, while the rigid body motion of particles and inter-particle interactions are modeled by DEM [160]. A fundamental requirement is that arbitrary particle shapes generated by the fragmentation process must be representable. Furthermore, the coupling needs to set how the forces are applied on the material points at the boundary of each particle, how the child particles are defined and meshed from the broken bonds, and how DEM steps and peridynamics steps are interfaced to reduce computational cost. Fig. 41 shows an example of recent application of this approach to the consolidation of sand in a box.

4.2 Particle-level models

The BPM and continuum or hybrid models can in principle be used to simulate the comminution of a large number of particles but DEM calculations are prohibitive in 3D. The particle-level strategy consists in applying fragmentation rules to the particles. This is the Particle Replacement Method (PRM) or any variant that does not require sub-particle stress fields [28, 30]. The fracture criterion must be based on a model of single particle breakage. It can be the energy absorbed by the particle during its strain history, a force threshold, the impact energy [35, 135]. It can account for the natural variability of the strength and the effect of parent particle size. The progeny particles are created with an initial overlap. When the parent particle is removed, the repulsive forces push the progeny to fill the volume left by the parent particle. To avoid initially high repulsive forces between the progeny particles, a relaxation factor can be used. The progeny size distribution corresponds to the primary breakage function.

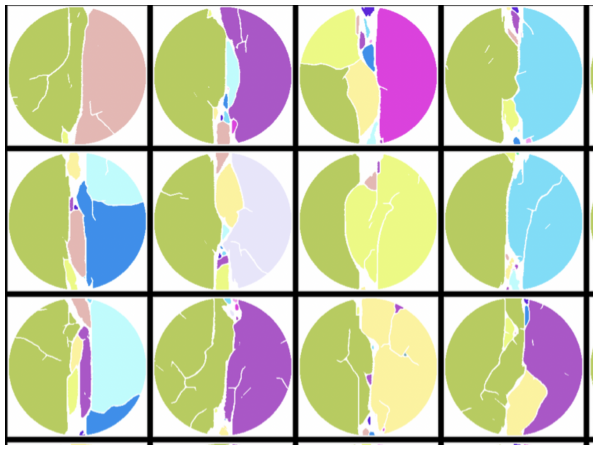

Figure 40: *Diametral compression of a single particle simulated by the bond-based Peridynamics method for different distributions of pre-cracks inside the particle [13].*

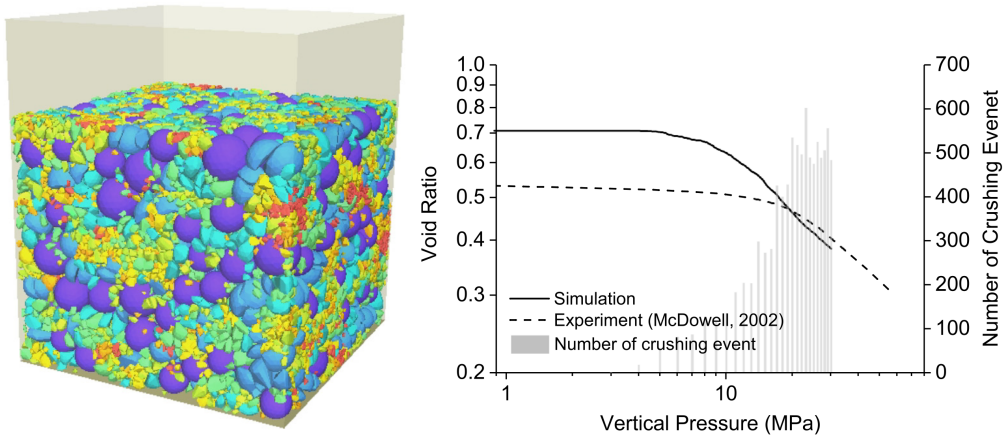

Figure 41: *(a) Snapshot of a uniaxially compacted sample by hybrid peridynamics-DEM simulation. The color indicates the number of crushing events experienced by a particle. (b) Evolution of void ratio and number of crushing events with vertical pressure [160].*

What is mostly expected from PRM? The prediction of particle size distributions and consumed energy for complex boundary conditions once the underlying rules for single particle fracture are calibrated. In other words, the added value of PRM-DEM simulations is to reflect the stress and energy distributions inside a granular flow to deliver robust prediction of particle fragmentation. The predictions in this sense are generally in good agreement with measurements [67]. An example is shown is Fig. 37(b). However, by construction, BPM cannot predict particle shapes. Although there is no difficulty in using aspherical particle shapes for replacement, but they represent model input parameters .

DEM simulation of breakable particles mirrors quite well the inherent dilemma of DEM. The breakage of a cluster of primary spherical particles is a simple extension of HS-DEM. Running simulations even with such a crude model provides many physical insights on the behavior of real processes such as grinding in ball mills. Nevertheless, such simulations do not yield quantitative predictions of the process. Advanced DEM simulations of breakable particles with sub-particle continuum degrees

of freedom account for particle shapes, complex yield criteria at the bond level, finite size effects, surface effects, but require much high computational power. PRM provides an intermediate solution. The breakage rules for different types of materials and particle shapes can be further explored to develop a particle-level approach accounting for the progeny particle shapes in addition to fracture criteria. Finally, advanced imaging techniques are increasingly available to track particle breakage and analyze the shapes and sizes of the fragments for different types of materials, making it possible to validate and improve the BPM and continuum-based models of particle breakage, which can then be used in the framework of PRM for process scale simulations [30].

5 Soft particles

By ‘soft particle’ we mean a particle whose shape can change elastically or plastically without rupture. In other words, a soft particle has *shape degrees of freedom* in volume or in surface. This is a *softness at the particle level*, contrasting the standard DEM in which the reference particle shape does not change but the softness is concentrated at the contact points (contact softness). For example, most metallic powders are composed of soft particles which may deform plastically under load without rupture. Many products in pharmaceutical and food industries are soft-particle materials. This broad class of materials may be also extended to colloidal pastes, clays, vesicles, and microgels. Soft granular materials may undergo volume change as a consequence of particle rearrangements as in hard-particle materials, but also as a result of particle shape and size change. Methods for soft particle simulations can be broadly divided into two groups based on surface deformation and volume deformation, respectively.

5.1 Surface deformation methods

A simple method to represent a soft particle is to consider its surface as a flexible membrane consisting of primary hard spherical particles connected by bonds to form a triangulated network [113]. The bonds have a bending rigidity with reference angles which define the reference particle shape. The spheres can be replaced by articulated sphero-cylinders. Furthermore, plastic deformations can be modeled by allowing the reference angles to evolve. However, the bulk constitutive behavior of the particle is not included in this approach unless the motions of the boundary points are properly coupled with the overall shape and volume change of the particle. The same approach can be used to simulate flexible elongated particles and sheets. An example is displayed in Fig. 42.

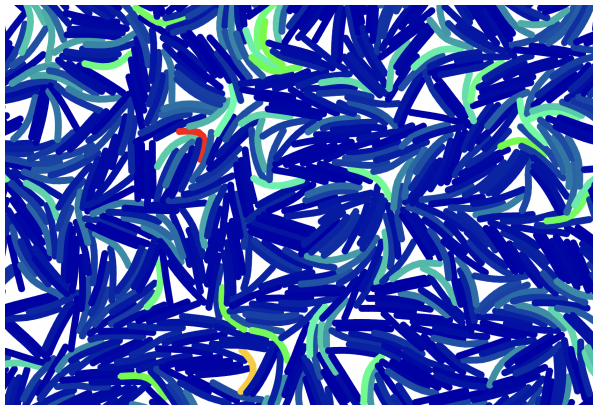

Figure 42: *Assembly of consolidated elongated clay-like particles. Each particle is composed of several spherical particles connected by linear and angular harmonic springs. Color code is proportional to strain energy.*

Another computationally cheap method was recently proposed with a consistent theoretical background based on the Virtual Element Method (VEM) [50]. This method employs polyhedral representation of particles and assumes that the strain field is uniform inside each particle. Each vertex at the particle surface is a material point with three displacement degrees of freedom. Its displacements are governed by the uniform strain tensor of the particle whereas the average stress tensor is calculated from the contact forces acting on the particle. In contrast to flexible membrane, this approach accounts

for the constitutive behavior of the particle formulated as a relation between the average strain and average stress of the particle.

Although this formulation cannot capture local stress/strain concentrations stemming from very local contact interactions between particles, for an assembly of many particles this choice predicts well the average strain level within each particle, and thus results in a good stress/strain prediction for a system of particles. Fig. 43 shows the force-displacement relation for a sphere (represented as a polyhedral particle) obtained by this method as compared to a FEM simulation. Because of uniform strain assumption, this method suits well to symmetric convex shapes. For more complex shapes, the interior of a particle can be divided into several polyhedral domains. A compressed packing of convex polyhedra is shown in Fig. 44.

The methods based on surface elements such as membranes or surface material points are interesting since they extend polyhedral shape representation to shape deformation at computationally low cost. We will refer to such methods as *Surface Deformation methods (SD-DEM)*.

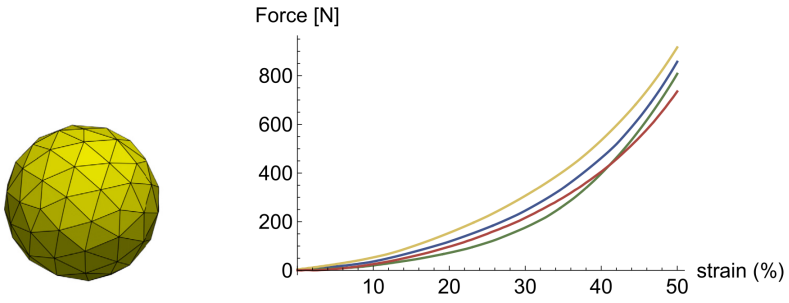

Figure 43: *Force-displacement relations for compression of a (meshed or polyhedral) sphere using Virtual Element Method (VEM) with three different values of a numerical model parameter. The reference curve corresponds to a FEM simulation of the same sphere [50].*

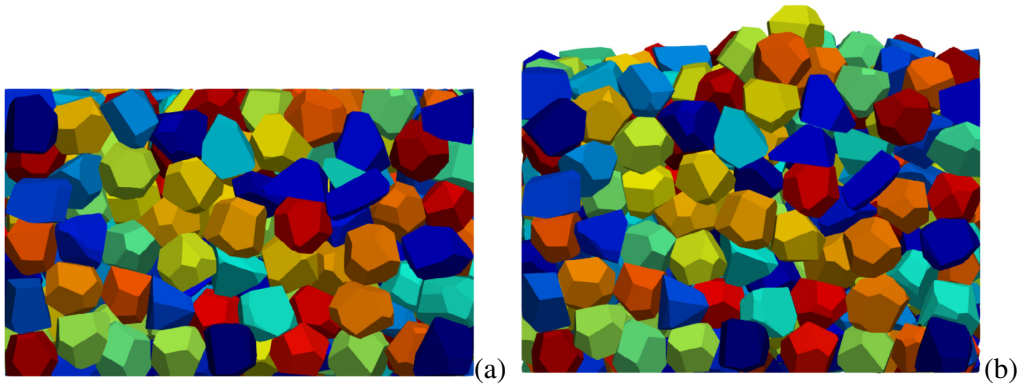

Figure 44: *Snapshots of a packing of polyhedral particles before (a) and after (b) 18% of uniaxial compression [50].*

5.2 Volume deformation methods

A granular material composed of soft particles can be simulated by handling particle deformations as a continuum field and treating frictional-cohesive contacts by means of DEM. Mesh-based FEM can be

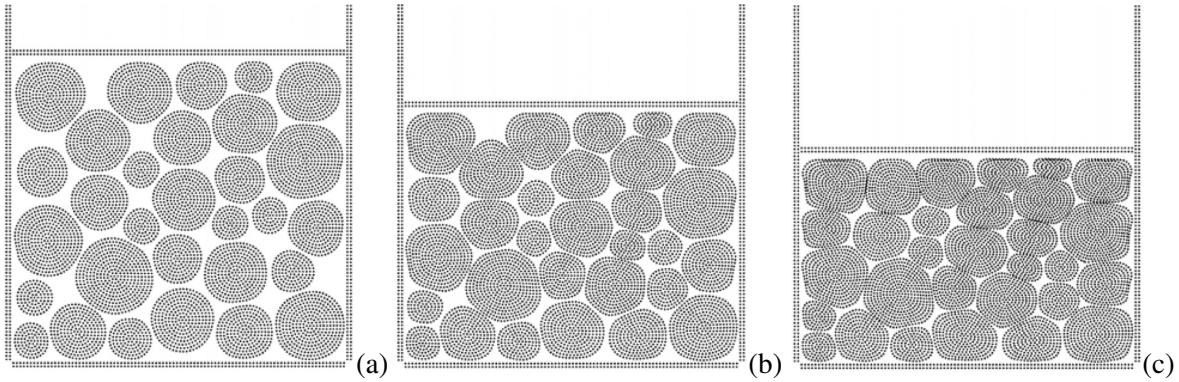

Figure 45: *Uniaxial compaction of a packing of soft elastic particles by CDM-MPM [103].*

used for the simulation of particle shape change when the deformations are not too large. Otherwise, mesh-free methods such as Material Point Method (MPM) or Smooth Particle Hydrodynamics (SPH) must be used. Figure 45 shows an example of compaction of elastic particles by a coupled CDM-MPM (CDM for contacts and MPM for particles) [103]. MPM is a mixed method combining the Eulerian and Lagrangian descriptions of the material. The Lagrangian description consists in representing each body by a collection of material points, and the Eulerian description is based on a background computational mesh. The information carried by material points is projected onto the background mesh, where equations of motion are solved. The mesh solution is then used to update the material points. MPM brings together the advantages of Eulerian and Lagrangian methods by avoiding the distortion of Lagrangian mesh and tracking the boundaries of bodies. Each particle is represented by a collection of Lagrangian material points, with assigned masses. The average motion of those points represents the particle motion whereas their relative motions capture its local deformation. A feature of this method is that the overall particle rotations do not need to be considered as they result from the displacements of material points.

The kinematic constraints and stresses arising from unilateral contacts between particles and the bulk deformations of the particles are strongly coupled. While the contacts play the role of boundary conditions for the resolution of continuum equations in each particle, the evolution of contacts is determined by particle deformations. In MPM, the use of the same set of continuous shape functions in both mappings (the mapping from material points to mesh nodes and vice versa) naturally results in sticking (no interpenetration and no slip) contact scheme and thus no interpenetration occurs. With the use of a single-valued velocity to update the positions of material points, the sticking contact between two different bodies can be handled automatically at no additional computational cost using the original MPM, and no contact surface detection is required, but the contacting objects may not separate. For this reason, it is necessary to define different body velocities at the nodes and to implement frictional contact laws independently from MPM.

The above examples show how both breakable and soft particles push the limits of DEM beyond its founding principles. This territory is fresh and still poorly explored both theoretically and computationally. We may describe it as a mixed or *hybrid continuum-discrete modeling* approach in which discrete elements (objects) carry material points governed by continuum equations instead of rigid-body motions. We propose to call it *C-DEM* with all its possible variants. This territory can be approached from the continuum side, in which case the particles are deformable but can be made rigid by using, for example, distributed Lagrange multipliers and handling the contacts as unilateral constraints. Alternatively, one may approach the problem from the DEM side by keeping discrete

elements and introducing extra material points where necessary.

A key challenge of C-DEM is its high computational cost (higher than rigid aspherical particle shapes). Nevertheless, with increasing computing power, we expect C-DEM simulations to become commonplace in near future. The focus should therefore be placed on the formulation of high-fidelity hybrid methodologies irrespective of algorithmic complexity and computational cost. The increasing complexity of DEM codes is a natural reflection of the enhanced realism of numerical materials in number of degrees of freedom, contact or particle behavior, particle shape, breakage and particle-level deformation.

6 Computational issues

The physics fidelity of the numerical material is the key to increase the realism of DEM-based models. However, physics-enhanced models require more input data and more processing time. For example, contact detection between polyhedral particles needs more algebraic operations and has therefore a higher computational cost than contact detection between spheres. At the same time, more information must be provided to describe the system. Hence, the amount of information and simulation time increase with both physics fidelity and system size (number of particles). Computational power has been a key drive of DEM during the last 40 years. Increasingly more realistic and advanced DEM simulations have become possible due to more accessible computational resources such as higher calculation speed and larger available memory. The GPU technology and parallel computing have played an essential role in this respect. Therefore, it is expected that computational power will continue to drive the future developments of DEM, enabling enhanced physics fidelity of the numerical material and larger-scale simulations.

It should also be remarked that the data structure and algorithm have to be adapted to the amount of manipulated data. For example, if the particle shapes and initial packing state are extracted from X-ray tomographic images, one needs an appropriate procedure for the representation of the image data to be used by the DEM algorithm. Hence, new algorithms must have high *data fidelity*, allowing for efficient data representation and flow. This data-driven trend is now quite common in many other areas of science and technology. In this respect, Machine Learning (ML) is among the assets which can lead to a paradigm shift in DEM.

6.1 Parallel computing

In the pursuit of computational power, DEM and its algorithms and implementations must constantly fit to the available hardware architecture. A transition was operated one decade ago with the advent of General Purpose Graphics Processing Units (GP-GPUs). GPU is a multi-threaded architecture with the ability of performing significantly more floating point operations per unit time than a CPU. However, only applications exhibiting a high degree of parallelism are suitable for GPU. Therefore GPU-based parallelization has gained popularity and several robust and scalable parallel algorithms of DEM on GPU have been developed with 100-fold speed-up factors during the past decade [54]. GPUs not only accelerate DEM simulations but also scale well with system size using spatial domain decomposition, extending DEM simulations to billion particles.

Many GPU-based DEM simulations can be found in the literature. Some examples are charge motion in tumbling mills with 10^7 spherical particles taking only 18.5 h for one full revolution [52], hopper flow of convex and non-convex polyhedral particles [54] (see Fig. 46 for comparison with experiments), Powder compaction with wide size distributions with a multi-grid neighbor searching method with more than 5×10^5 particles [59], and full-scale simulation of twin screw simulator with irregular-shaped particles (see Fig. 47) [159].

Although programming interfaces such as CUDA exist for GP-GPUs, the development of a GPU-based DEM code needs high skill and experience. Furthermore, GPUs consume high energy and involve bottlenecks in terms of memory and communication. The alternative solution consists in using large CPU clusters or supercomputers with simple OpenMP parallelization, which has the advantage of preserving the structure of the code. However, according to a current belief (Huang's law) the performance of GPUs will more than double every two years. It seems thus that investing in GPU-based DEM is a viable solution despite its high technicality.

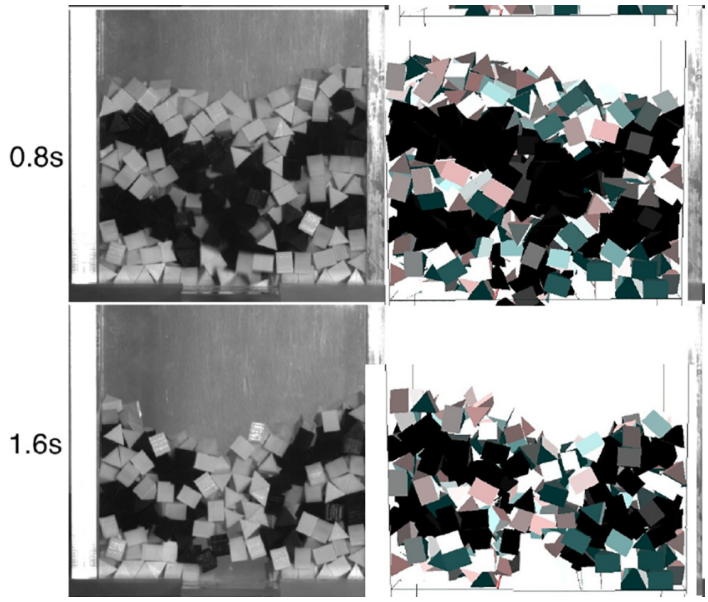

Figure 46: *Hopper discharge of polyhedral particles: experiment (left) and GPU-based simulation (right) [54].*

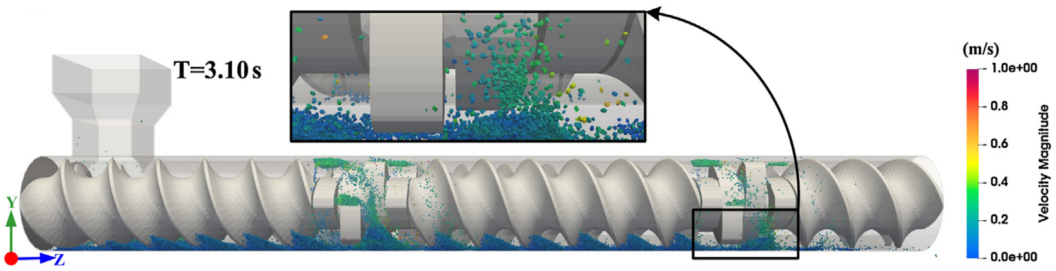

Figure 47: *Flow profiles of biluna-shaped particles in GPU-based simulation of twin screw granulator (Zheng2022).*

6.2 Particle coarsening

Particle coarsening consists in increasing the particle sizes as compared to their real sizes by a factor $\xi > 1$ while decreasing their number N_p by a factor ξ^{-3} so that the total mass or volume is conserved (by conserving solid density ρ_s). Under some conditions the particle dynamics of a large number of small particles is similar to that of a lower number of larger particles. Particle coarsening can considerably reduce computational cost. For example, for $\xi = 10$ the number of particles is reduced by a factor 10^3. Some authors use the term 'coarse-graining' which refers to a theoretical upscaling based on the replacement of a group of particles by a 'parcel' with renormalized properties. This is different from particle coarsening since the upscaled particles are rigid. In other words, the system is identical but with larger particles and rescaled parameters whereas a parcel must in principle be equivalent to a soft particle or material points obeying continuum equations; see section on multiscale modeling 6.3.

It is also important to note that particle coarsening has no meaning for the study of rheology. The simulated system in rheology is a representative volume element (RVE), which is defined by a

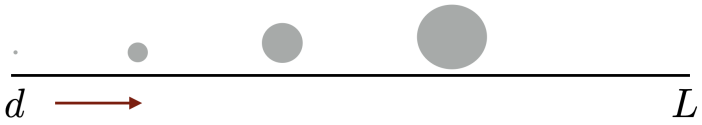

Figure 48: *Particle coarsening $d \to \xi d$ within system size L.*

minimum number of particles. Such a volume, with possibly periodic boundary conditions, represents a portion of a granular material which may contain many more particles. No macroscopic length is imposed in rheology and all length scales, including particle size d, are only internal. The finite size effects can be analyzed as a function of the ratio L_c/d, where L_c is the linear size of RVE. Particle coarsening is useful when a system-scale length L is imposed. More specifically, one should consider the smallest relevant length L_{min} of the system, which can be the thickness of a fluidized bed, the radius of a rotating drum or the width of a silo outlet. On the particle side, the largest particle size d_{max} matters. Particle coarsening can be used when $L_{min} \gg d_{max}$ so that no significant finite size effects occur when d_{max} is replaced by ξd_{max}; Fig. 48. In the case of Euler-Largange simulations of fluid-particle flows, L_{min} is the mesh size. If the coarsened particle size is close to fluid mesh size, the fluid must be coarsened.

The question is which parameters must be rescaled when d (any particle size within the particle size distribution) is replaced by ξd. To address this question, we must first decide which parameters are conserved. Since we are interested in reproducing the process with fewer and larger particles, the process-scale boundary conditions and system size L must be conserved. In the same way, material properties such as solid density ρ_s and Young's modulus E must be conserved. The role of boundary conditions and driving mechanism is to impose a velocity, a strain rate, a force or a stress on the particles. Let us consider a confining pressure p_0 and a velocity v_0 as imposed quantities which we keep constant (coarsening factor $\xi^0 = 1$). The particle mass scales as $m \sim \rho_s d^3 \sim \xi^3$. Then, forces scale as $f \sim pd^2 \sim \xi^2$ and contact normal stiffness scales as $k_n \sim Ed \sim \xi$. In the presence of cohesion with surface tension γ_s, the cohesive stress is $\sigma_c \sim \gamma_s/d$. Since the cohesive stress is conserved, we have $\gamma_s \sim \sigma_c d \sim \xi$. In the presence of gravity g, the gravity-induced stress is $\sigma_g = \rho_s g d$, implying that gravity scales as $g \sim \xi^{-1}$.

Similar coarsening factors are obtained when starting from the conservation of the restitution coefficient or requiring the conservation of the relative overlap δ_n/d [134]. CFD-DEM simulations of cohesive particle fluidization for different values of ξ show that this particle coarsening method successfully reproduces the mean slip velocity for $\xi = 4$ and bond numbers as high as 50; see Fig. 49. It is noteworthy that cohesive particles may agglomerate to form clusters that have a size comparable to L, in which case particle coarsening cannot be applied.

Despite partial verification, the above coarsening factors based on the process-scale stress and velocity cannot work in all processes. In a single-particle process, as in dilute or semi-dense systems, the inertial time $t_i \sim d/v_0$ and relaxation time under stress $t_s = d\sqrt{\rho_s/p}$ scale as ξ so that the inertial number $I = t_s/t_i$ is invariant by coarsening transformation. In a dense flow, the shear rate $\dot{\varepsilon}$ is imposed and we have $t_i \sim \dot{\varepsilon}^{-1} \sim 1$. Hence, the inertial number $I = \dot{\varepsilon} d\sqrt{\rho_s/p} \sim \xi$ is not conserved. As a result, the inertial number increases with coarsening. This is also reflected in the kinetic pressure $\sigma_i = \rho_s(\dot{\varepsilon}d)^2$, which in contrast to other stresses scales as ξ^2. This issue can, however, be mitigated by applying a scale factor to the shear rate $\dot{\varepsilon} \to \xi^{-1}\dot{\varepsilon}$.

There is yet another issue which arises in dilute systems governed mainly by binary collisions. In the coarsened system, the frequency of collisions (number of collisions per particle per unit time)

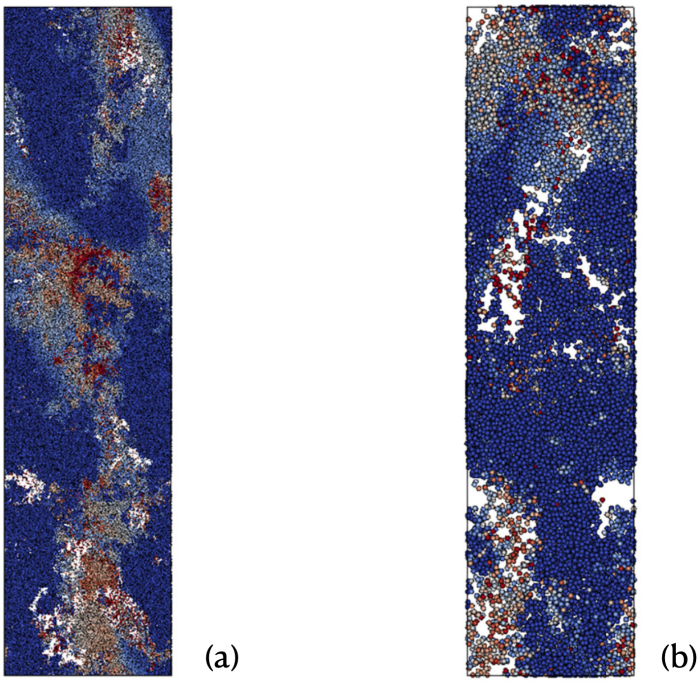

Figure 49: *Particle velocity field in a fluidized cohesive bed. Colors indicate the vertical velocity of particles. Bond number is 50. (a) The original system with 1.3 million particles; (b) The same system with coarsened particles with coarsening factor* $\xi = 4$ *[134].*

varies as $n_c \sim v_0/d \sim \xi^{-1}$. We use here d since the mean free path in the coarsened system is proportional to d for a given concentration of particles. Although the kinetic stress is conserved ($\sigma_k \sim n_c m v_0/d^2 \sim 1$), the dissipation due to inelastic collisions per unit time varies as n_c and declines therefore as ξ^{-1}. As a result, in a homogeneously cooling system, for example, the evolution of the granular temperature depends on the particle size [37]. This problem can be mitigated by decreasing the restitution coefficient e_n to compensate for the ξ^{-1} scaling of the number of collisions. Since the amount of energy dissipated in the center of mass of two particles is proportional to $1 - e_n^2$, the rescaled coefficient of restitution becomes

$$e_n'(\xi) = \sqrt{1 - \xi(1 - e_n^2)} \tag{28}$$

This solution works, however, only for $\xi < 1/(1 - e_n^2)$. There is no simple solution to the problem beyond this limit. Note also that when the binary collisions in a process are not the main origin of energy dissipation, the ξ^{-1} scaling may have lower impact on the particle dynamics.

Other particle-coarsening approaches have also been proposed, but not verified for all possible states of granular materials [23, 66, 83]. This is an important practical aspect of DEM simulations since full-scale industrial granular processes often involve more particles than what can be simulated with the current computational power. It is noteworthy that verifying a particle coarsening approach does not warrant using very large systems. The verification requires only simulations with two different particle sizes. For given coarsening rules, if the results of the two simulations are similar, then the approach is basically correct. This verification should be applied to various dense and dilute states or at least to the states which are concerned by the application of interest before application to larger scales.

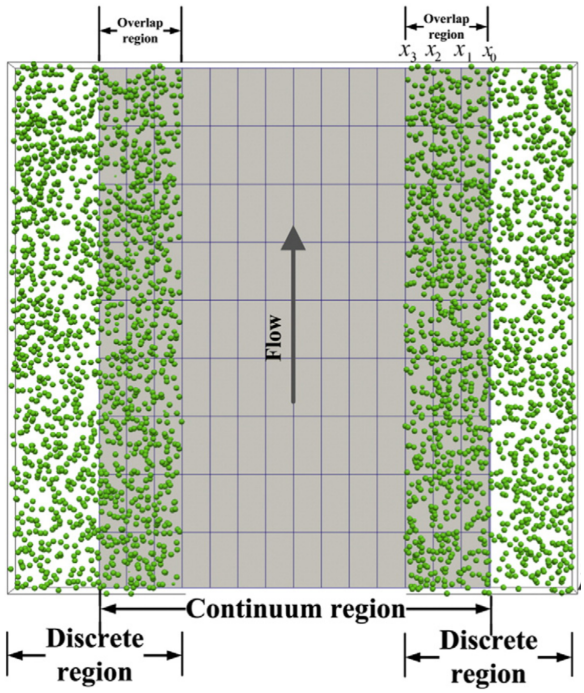

Figure 50: *Application of a concurrent multiscale approach to rapid granular flow in a channel. The simulation domain is divided into a continuum zone located at the center of the channel and two discrete zones near the two side walls. The overlap zones are used to match together the continuum and discrete zones [26].*

6.3 Multiscale simulation

Multiscale simulation methods couple together modeling elements from different scales of description. A multiscale model of granular materials simulates the dynamics of bulk material as a continuum field undergoing stress and strain at a coarse level of description, corresponding to length scales well above particle size, but zooms into particular zones of the material where particle-scale effects prevail (e.g. close to walls, at the outlet of a silo, shear bands...), and simulates those zones using DEM. Multiscale methods combine in this way the high physics fidelity and accuracy of DEM with the low computational expense of continuum methods at large scales. Note that continuum methods are computationally cheap only at large scales as compared to DEM. In contrast, the continuum approach discussed in sections 4 and 5 for sub-particle modeling of deformations and stress fields is computationally more expensive than discrete solutions.

Multiscale simulation methods can be serial, concurrent or hierarchical. The idea of the *serial multiscale approach* is to simulate the material in the 'hot' zones, where particle dynamics is necessary, by means of a DEM solver, synthetize the results into a set of relationships and parameters, and pass them up to a continuum solver for the simulation of continuum zones. A serial method is misleading when the scales are strongly coupled together. In this case, a *concurrent multiscale method* must be used by simultaneously simulating the zones obeying continuum equations and zones obeying particle dynamics. The frontiers between these zones can change in time depending on the specific particle-scale features that need to be taken into account (non-affine displacements, velocity gradients, solid fraction). Concurrent multiscale modeling is similar to the so-called sub-grid modeling, which is a

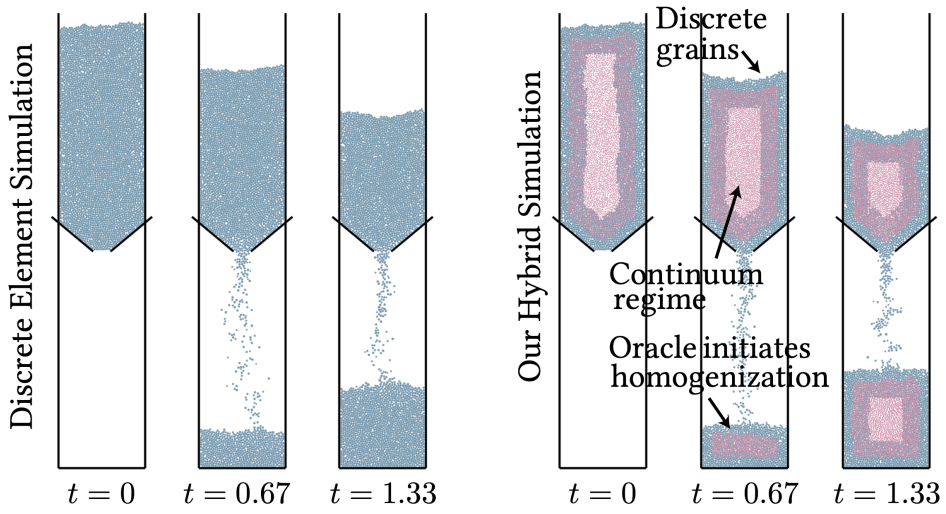

Figure 51: *Silo discharge: A silo discharges grains with a discrete method (left) and with a hybrid multiscale method (right) [153].*

ubiquitous simulation method. It refers to the representation of small-scale physical processes occurring at length scales that cannot be resolved on the grid size. These processes can be of a different physical nature as compared to the grid-scale process.

The *hierarchical multiscale approach* uses DEM at each integration point of the continuum field to compute the stresses and internal variables in response to the strain increment input from the continuum field at that point. In other words, the constitutive laws and closure equations of the continuum solver are replaced by DEM simulation. The ambition of a hierarchical multiscale approach is therefore to bypass phenomenological constitutive laws. Due to the hierarchical structure of the approach, all the information collected from DEM simulations at the integration points is put together for the computation of strains at the continuum level. Hence, no message passing is necessary between the DEM simulations performed at the grid points, a feature that allows for efficient distributed parallel computing. This approach has been used with a FEM solver to showcase several applications such as shear localization, cyclic mobility, and liquefaction in quasi-static simulations of granular materials [3, 25, 4, 56, 57, 82].

A concurrent multiscale approach was developed by coupling DEM with Navier-Stokes equation combined with kinetic theory as the continuum model, which was numerically solved using the finite difference method on a staggered grid [25]. The discrete and continuum zones were pre-defined and coupled via dynamical exchange of parameters in the intermediate overlap zones. Fig. 50 illustrates the application of this approach to rapid granular flows in a channel [26]. A more extensive and adaptive concurrent multiscale model was proposed with an elastoplastic behavior as continuum model and implemented using the material point method (MPM) [153]. A mass-splitting coupling principle was used to enforce agreement between the two simulation states in the overlap domains together with a method to dynamically partition a granular material into continuum and discrete zones. Fig. 51 displays an example of MPM-DEM simulation of silo discharge.

This adaptive MPM-DEM approach was also successfully applied for the simulation of shear localization. Starting the simulation using MPM, the onset of shear bands is monitored based on the velocity field, and the hot zones are identified for the placement of particles [24]. The DEM is used in

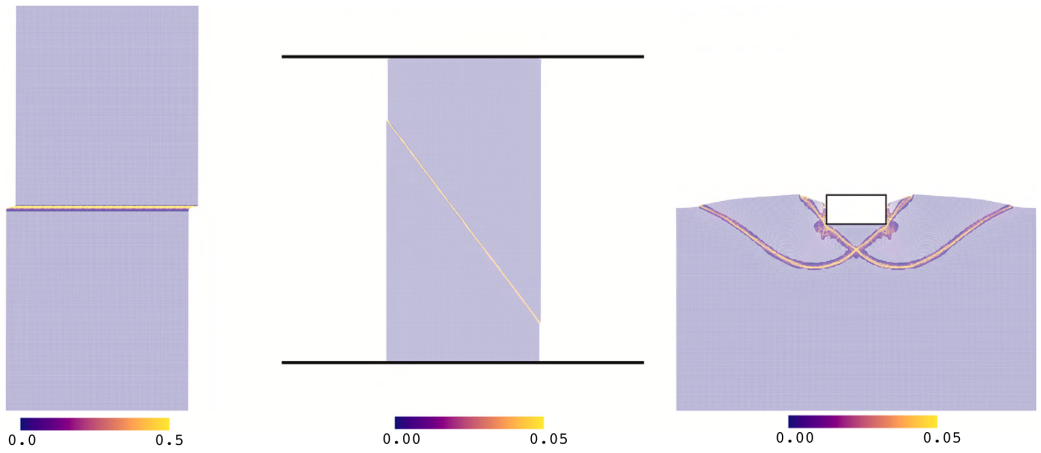

Figure 52: *Shear band formation in multiscale DEM-MPM simulations [24].*

this discrete zone while the rest of the domain is simulated with the continuum method. Fig. 52 shows examples of simulations in different geometries in which thin shear bands of well-defined thickness (a few particle diameters) have developed. Over two orders of magnitude performance speedup is obtained in these large-scale simulations compared to pure DEM simulations of the same system.

It must be underlined that this hybrid multiscale method owes fundamentally its success to the hybridization method and the approach used to match the continuum and discrete states in the overlap zones. This approach must enforce the continuity of dynamics across scales. For example, the state variables of a continuum plastic theory of granular materials reflect the contact network structure. Hence, a hot zone should be replaced by a particle assembly whose microstructure represents the state of the continuum field in that zone [24]. A possible solution consists in subjecting the particle assembly to the same strain history as the hot zone. This method ('kinematic training') is similar to the serial multiscale approach, but combined here with a concurrent method.

The multiscale continuum-discrete approach opens a broad scope for large-scale simulations of the granular processes in which the bulk behavior can be represented as a continuum field. Fluid-grain flows and homogeneous fluidized beds, for example, can be simulated by this approach. An interesting aspect of the concurrent multiscale approach is to provide a framework for quantitative trade-off between accuracy and computational efficiency through hybrid continuum and discrete simulations of granular flows. It can combine basic DEM with complex high-order (nonlocal, micropolar...) constitutive equations or, conversely, advanced DEM with basic constitutive equations. The extent of the discrete and continuum zones can also vary. Furthermore, multi-physics processes such as heat transfer and fluid flows can be coupled with DEM or continuum in the same framework. This high degree of flexibility is a real asset for smart use of DEM. In fact, when rich and validated continuum models exist, DEM must be used *only if necessary* [154, 24].

6.4 Machine Learning

While data-driven science is imposing itself as a paradigm in various fields of research, computational methods such as DEM are called to integrate with Machine Learning (ML) models and techniques. ML algorithms build a model based on sample data (training data) in order to make predictions without being explicitly programmed to do so. They are often formulated as minimization of a loss function

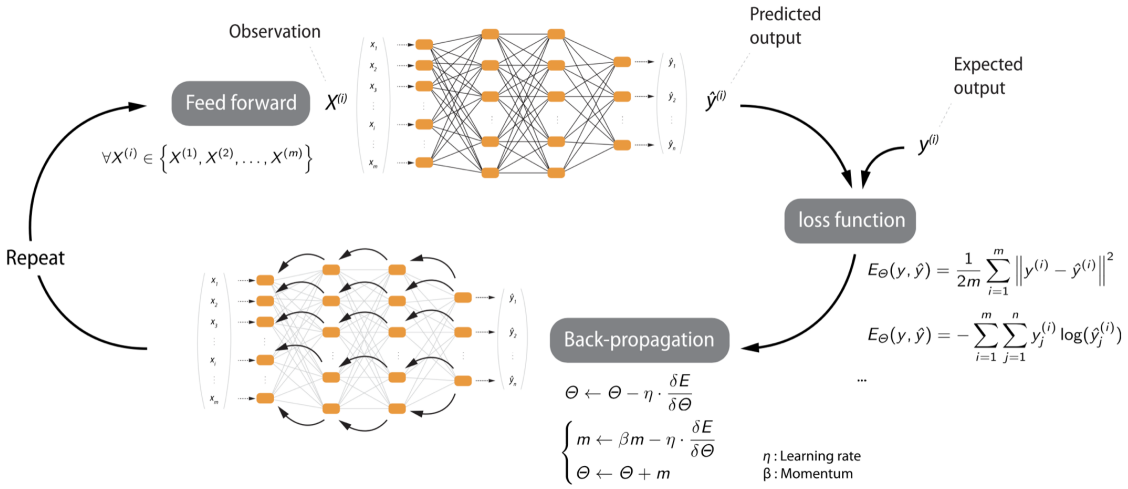

Figure 53: *Learning process on an Artificial Neural Network (ANN).*

expressing the discrepancy between the outputs of the ML model and the actual values of the target properties on the sample data. In this sense, ML is akin to mathematical optimization. Different ML models exist such as Artificial Neural Networks (ANN), decision tress, regression analysis, Bayesian networks, and genetic algorithms.

ANN is a general term encompassing different network architectures. A neuron is a mathematical expression that filters the information traveling through the net. Every neuron receives its weighted inputs from the connected neurons of the previous layer, which are normally aggregated along with a bias that scales the input to the useful range; see Fig. 53. The combined summation is delivered through a transfer function to generate the neuron output. Weighted connections modify the output as it is passed to neurons in the next layer, where the process is repeated. The weight vectors that connect the different network nodes are adjusted through the error back-propagation method. During training, these parameter values are varied to align with the measured output of a known dataset. When the network has been sufficiently trained to simulate the best response to input data, the network configuration is fixed and a test process is conducted to evaluate the performance of the model [20].

The interactions between DEM and ML intensify nowadays along three different routes:

1. ML algorithms can be trained to recognize microstructural and dynamical features (particle sizes and shapes, particle positions and velocities) from recorded data (CT images, acoustic emission,etc). Such data can be used for calibration, initiation, or validation of DEM simulations.

2. DEM simulations can provide extensive high-fidelity training datasets for ML-based characterization of real granular materials and processes.

3. ML can be used to speedup DEM algorithms for contact detection, and force or velocity calculations.

An example of direct data analysis is the use of the ML technique and the level set method to segment X-ray Computed Tomography (CT) images and reconstruct the particles. In the example shown in Fig. 54, the segmentation results were predicted by means of a trained classifier ML model that implicitly includes image features and regression functions and an edge-based level set method was

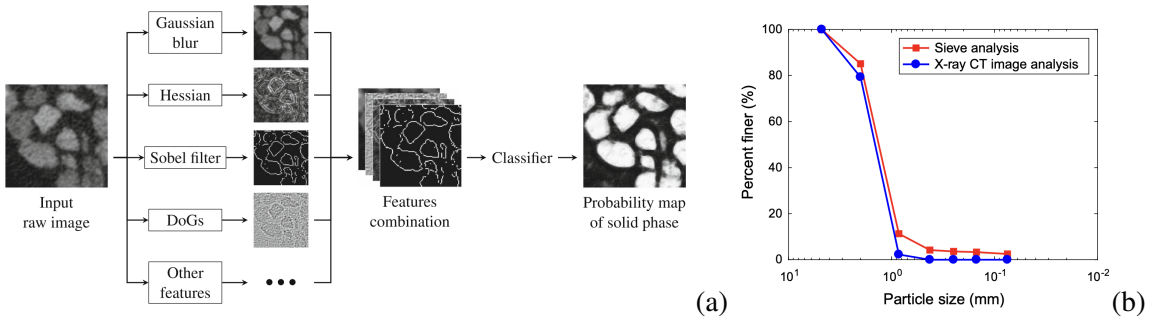

Figure 54: *(a) Combining various image features into the classifier model in ML-based image segmentation process; (b) comparison between the predicted and measured size distributions [77].*

applied to characterize the particle shapes [77]. Several features were combined to reconstruct realistic particle shapes with superior performance over the conventional watershed-based method in terms of both the pixel-based classification accuracy and the particle-based segmentation accuracy. Other examples are extraction of particle shapes or mechanical properties from realistic packing images [152, 155, 157], calibration of DEM parameters from those of the constitutive relations for rockfill simulations [92], prediction of hopper discharge rate [75], and automatic tracking of rod-like particles in dilute granular materials [115].

Another interesting application concerns the characterization of granular flows from acoustic data. For example, with an audio signal transformed into a spectrogram, convolutional and recurrent ANNs were used to estimate the amount of poured granular material [27]. Convolutional models excel in learning local hierarchical features on structured inputs (2D images, 1D audio signals…) whereas recurrent models are adapted to sequential and temporal data with variable-length inputs. The acoustic signal emitted by granular materials carries a rich signature of various flow features such as the nature of granular material, particle sizes, and flow rate. Hence, deciphering acoustic signal by means of ML models can potentially be used to estimate the values of parameters (restitution coefficients, friction coefficient, dissipation rate) needed for DEM simulations.

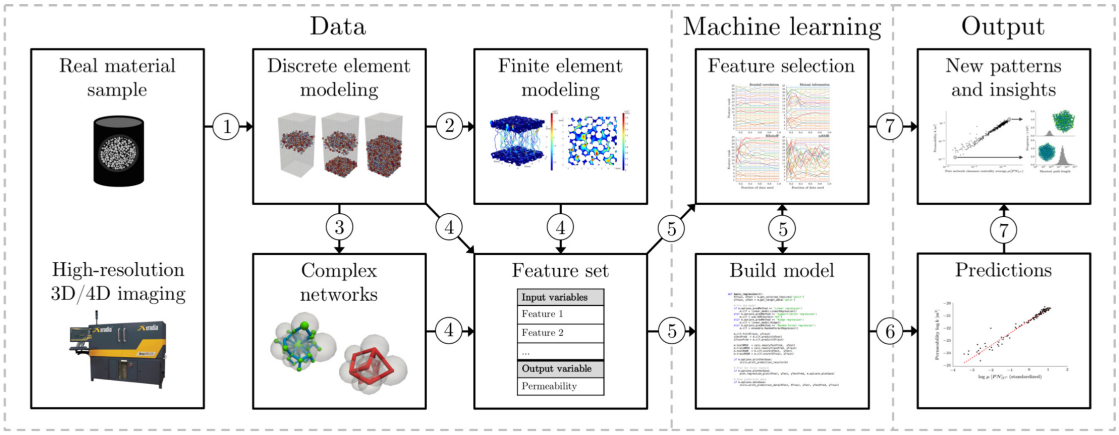

Figure 55: *Design of an ML-based algorithm for the prediction of the permeability of a granular packing [143].*

An example of using DEM to generate training data is illustrated in Fig. 55 [143]. Real sample

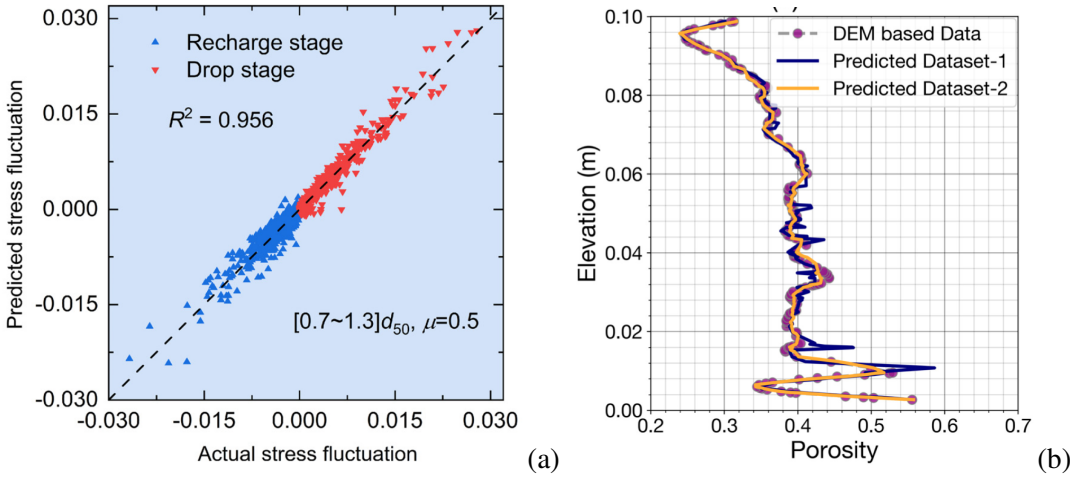

Figure 56: *(a) Stress fluctuation predicted by ML versus DEM data [93]; (b) Porosity along vertical direction predicted by ML versus DEM data [20].*

parameters, partially obtained from high resolution imaging, are used in the DEM simulation to generate realistic numerical samples (step 1). Fluid flow is simulated with a finite element method to compute the permeability (step 2). A pore network and contact network are constructed to compute multiscale complex network variables (step 3). The data comprise the physical properties at the pore and grain scale, the network variables and permeability (step 4). The resulting feature set is used for feature selection and model construction (step 5) to generate predictions (step 6). The ML framework evaluates the contribution of each feature to the overall permeability.

DEM-generated data were also used to train an ML model for liner wear of ball mills [63]. The wear parameter is controlled by independent features such as wear surface mesh resolution and location of the point considered on the wear profile, and ANN was used to establish their functional relationship. The ANN model predicted the wear with with an accuracy of 93%. This approach was also applied to a large industrial mill, and the predicted worn lifter shape compared well with real data. As another application of DEM data, ML was used to extract features from microslips in slowly sheared granular materials composed of ellipsoidal particles to macroscopic stress fluctuations [93]. It was found that the data-driven model that incorporates the information of the spatial distribution of microslips can robustly predict the magnitude of stress fluctuation; see Fig. 56(a). A similar methodology based on DEM simulations and ANN was used to predict the porosity of packings of gravel and fine sediments from particle size distributions along horizontal and vertical directions [20]; see Fig. 56(b). Particle rearrangements in assemblies of dimers and ellipses were also studied by means of the ML technique [58].

A much more direct application of ML concerns the possibility that expensive calculations of contacts, forces and velocities in DEM algorithms be replaced by an ML-enabled framework. It may even be speculated that, in near future, ML will provide adequate tools to ease algorithmic constraints on the choice of numerical materials in terms of particle shapes, contact models, breakage rules, and so on. Recent pioneering published work supports this approach through promising proof-of-concept results.

For instance, ANN models were employed to detect and resolve particle contacts in DEM from the particle geometric descriptors (position, size, shape) as inputs. Using random translation and rotation,

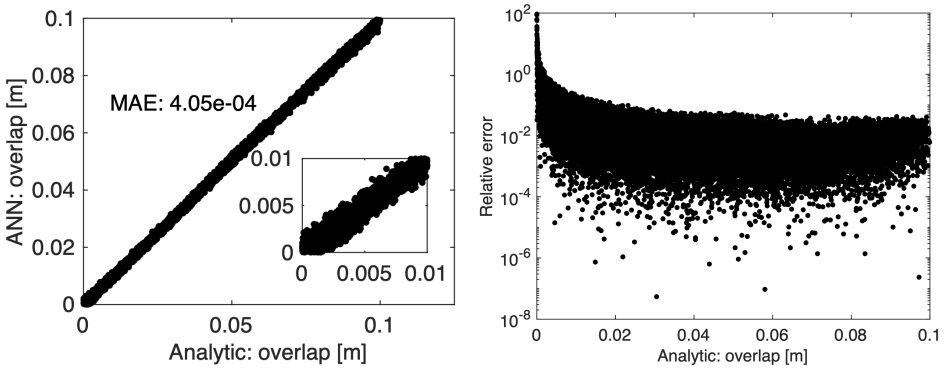

Figure 57: *Predictions of overlap lengths by means of ML (left) and their relative errors (right) [78].*

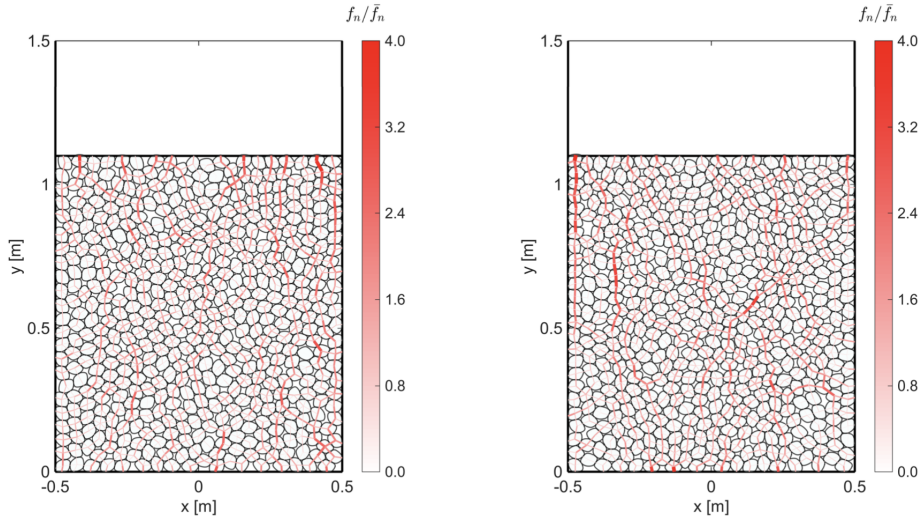

Figure 58: *A packing of irregular-shaped particles prepapred by ML-enabled DEM (left) and conventional DEM (right) [78].*

large datasets were collected for a pair of particles and used for training, validating, and evaluating the models. The classification and regression networks were able to predict the contact status with an accuracy of 99% [78]. Contact normals and positions were obtained with relative errors below 10^{-3} for elliptical particles. However, it was found that, although the absolute error on the values of overlaps are small, their relative errors can be high for small overlaps, leading to significant errors in the values of coordination number and contact forces; see Fig. 57. Nevertheless, DEM simulations based on these ML predictions of contact features were found to accurately capture the trajectory and energy evolution of individual particles. Fig. 58 displays snapshots of packings of irregular-shaped particles in 2D built by uniaxial compression simulations using DEM and ML-enabled DEM [78]. A similar approach was to applied to super-ellipsoid and particles shapes generated by spherical harmonic expansion [61].

Machine Learning with a continuous convolutional ANN was also used to accelerate DEM by replacing the time stepping scheme with a multiple-step correction of positions. In the velocity-Verlet scheme, the intermediate velocities were passed to the neural network to derive the correction terms for positions [88]. In simulations of rotating drum flow and hopper flow a speedup of 78

times was achieved compared with conventional DEM. A key to this success was the use of a loss function accounting for both individual particle positions and their center of mass and averaging over a number of frames. The superiority of such a multi-scale loss function in accuracy and stability was demonstrated for different combinations of these contributions during the training period. The speedup is a consequence of much larger time steps used in the ML-accelerated simulations, leading however to lower granular temperatures as a result of circumventing short-time fluctuations.

ML-enabled DEM has a high potential of extension to much broader scopes:

1. The ML contact detection algorithms can be trained using real particle data. A pack of N_p particles contains $N_p(N_p-1)$ pairs of particles that can be employed to train an ML algorithm for contact detection.

2. Image-based training accounts for realistic particle shapes from which the contact normals and contact positions can also be obtained by appropriate methods such as the level set and used to train an ML algorithm. We note that in DEM calculations the particle shapes are involved only through the process of the detection of contacts and definition of their positions and normals.

3. Since in conventional DEM the calculation of contact forces requires interparticle overlaps, a reasonable alternative consists in using CDM for the calculation of forces; see section 2.3. The CDM appears to be the only viable approach since the overlaps can not be extracted from experiments.

4. The contact force calculation in CDM is akin to matrix inversion which is usually solved by an iterative Gauss-Seidel method. The latter can be replaced by a conjugate gradient method and passed to an ML algorithm.

5. When working with image-based data, the loss function must be defined from macroscopic variables measured by means of extensive simulations and experiments.

6. The massive data obtained in this framework can also be used to calibrate the simulation parameters. The two steps of training and testing in the ML technique coincide with the calibration and validation steps in DEM. The back-propagation of information from experimental measurements is actually the ultimate step towards digital twins (realistic simulations) based on DEM.

7. The image data can be further extended to audio data. The sound produced by flowing granular materials can provide a means to calibrate simulation parameters if the information encoded by acoustic waves can be deciphered and correlated with physical parameters.

These scopes promise both new methods to speedup DEM simulations and a framework for treating realistic granular materials. The key element for optimal use of ML is the development of physics-based ML algorithms that assimilate particle interactions, i.e. unilateral contact and Coulomb friction, and general physical requirements such as invariances and thermodynamic constraints [69]. An effective approach consists in separating geometry from force calculations. The geometry includes contact detection and contact network characterization (given by the positions and normals of contact points). This is the most time-consuming part of DEM and for real-world materials with irregular-shaped particles can be tackled by developing adequate imaging and ML models. For an explicitly defined contact network, the position increments can be determined by searching a set of forces and velocities that fulfil both contact dynamics equations and the inequalities expressing unilateral constraint

and Coulomb friction. This task is equivalent to nonlinear optimization on a convex set for which an adequate ANN architecture must be used together with activation and loss functions that account for inequalities. Once the velocities are determined, the particle positions and rotations can be advanced. This method is unconditionally stable and large time steps can be used [121].

Another challenge of ML-enabled DEM concerns breakage rules at the particle scale, which can be learned from real experiments and included in PRM simulations of breakable particles. Indeed, the fragmentation of a particle is controlled by its internal stresses, which are fully determined by the contact forces. For a given material and distribution of the internal defects of the particle, the breakage surfaces and therefore fragment sizes and shapes are fully determined by the contact forces. Such a correlation removes the need for mesh generation or particle tessellation, and it can be learned by an adequate ML algorithm and used to accelerate DEM simulations of breakable particles.

7 Validation issues

The epistemology and reliability of computational algorithms are generally defined in terms of *verification* and *validation* [106]. “Verification deals with mathematics and addresses the correctness of the numerical solution to a given model. Most of time, this consists in comparing computed output with analytic or benchmark solutions. Validation, on the other hand, deals with physics and addresses the appropriateness of the model in reproducing experimental data. Verification can be thought of as solving the chosen equations correctly, while validation is choosing the correct equations in the first place" [127]. In application to DEM, verification is the process of ensuring that the implemented algorithm approximates well the behavior of the numerical material whereas validation ensures that the numerical material is a good enough representation of the real material.

Verification and validation are not cleanly separable. This is because the numerical material chosen to describe a granular material reflects a compromise between physics fidelity and algorithmic tractability. This choice implies that the simulation is validated (or invalidated) as a whole and not just as a validation of the numerical material. For example, simulation of a granular material composed of polyhedral particles is possible only if a reliable contact detection algorithm for polyhedral particles exists. When the simulations are validated by experiments, not only the polyhedral model of the granular material with its input parameters is validated but also the implementation of the contact detection algorithm is verified. Furthermore, most of time, success is achieved in simulation with back-and-forth between numerical material, algorithm and implementation features. Both verification and validation require also *uncertainty quantification* (UQ), which consists in evaluating all input parameter uncertainties and the resulting uncertainty in the output variables [34]. Verification, validation, and UQ are the necessary ingredients for trustworthiness of DEM simulations.

7.1 Verification

A major difficulty for the verification of DEM algorithms is that analytic models fundamentally lack for the description of multi-particle and multi-contact granular materials. Verification in DEM simulations concerns therefore in the first place the single-particle or single-collision processes. Examples are a single particle falling in a viscous fluid and collisions between two particles. Such benchmark simulations can be used to study the influence of numerical parameters such as time step or space discretization by direct comparison with analytic solutions. In contrast to what one may naively assume, single-particle and single-contact simulations can be the most sensitive tests of a DEM code, in which the results depend on the combined effects of precision, round-off errors, numerical dissipation, and other parameters. Furthermore, such tests are not trivial for complex particle shapes such as meshed or polyhedral particles and soft or breakable particles. It is noteworthy that only after such a verification the single-particle and single-contact benchmark solutions can be used for the calibration of input parameters in application to a granular process.

In multi-particle systems, qualitative verification can rely on the known qualitative trends of system response quantities or particle-scale quantities to the variation of input parameters. Since a granular material can be found in many different mesoscopic configurations, transients are not adequate for verification and the steady states must be preferred unless the preparation protocol is carefully considered. For instance, a packing of given particle shapes and sizes and prepared by isotropic compaction with zero friction is generally a reproducible state corresponding to a random close packing of highest solid fraction. Transient flows starting from this configuration (after resetting the friction coefficient) show also robust trends.

The steady states exhibit also various degrees of inhomogeneity at different scales. Such spatial inhomogeneities arise either from constitutive instabilities or as a result of boundary effects. Since they involve space-time discontinuities, their reproducibility by numerical simulations is code-sensitive. In more general terms, the nonsmooth dynamics of granular materials (due to unilateral constraints and Coulomb friction) is regularized in conventional DEM algorithms, and the degree of model softness should play a critical role in the onset of instabilities and the extent of dissipative structures such as shear bands, bubble sizes, cooling clusters, and segregation patterns. While normal contact stiffness is an obvious softness parameter, the model dissipation parameters are also important factors.

Particle-scale dynamics and microstructures also represent sensible features that can be partially verified by a DEM code. Among the most straightforward particle-scale quantities, the constraint number Z_c (number of constraints per particle) and connectivity P_c (proportion of particles with exactly c contacts) are interesting quantities to verify. Z_c is different from the coordination number Z, which is defined as the number of neighboring particles. For example, a packing of polyhedral particles with zero friction coefficient in static equilibrium is isostatic and must have $Z_c = 12$ when the confining pressure is vanishingly small. Simulations show that this value is reached only if face-face contacts are counted as three constraints, edge-face contacts as two constraints and all other contacts as one constraint. This reflects the fact that face-face and edge-face contacts represent constraints on three and two degrees of freedom, respectively. In fluidized beds and rapid flows, the number of collisions per particle per unit time is a sensitive particle-scale quantity while granular temperature and the ratio of kinetic stress to confining pressure are discriminant output data whose trends with the variation of input parameters can be verified on a qualitative basis.

7.2 Uncertainty quantification

Beyond the trends of output variables as a function of input parameters, which provide useful information on the general behavior of a DEM software, the uncertainties due to numerical approximation and input parameters must be quantified to obtain confidence intervals for the output variables. Numerical approximation errors include discretization error, iterative convergence error, round-off errors, and also errors due to finite precision and computer programming mistakes [127]. Generally, the discretization errors refer either to the equations of dynamics or spatial discretization in continuum. In granular materials, the numerical approximation errors also include the discretization of polydisperse input variables such as particle size distributions and shape polydispersity.

Uncertain input parameters are either *aleatory* or *epistemic*. Aleatory uncertainty is due to natural variability of an input parameter and can be mathematically described with a probability distribution function. Epistemic uncertainty is due to a lack of knowledge on the precise value of an input parameter and can thus be mathematically described as being of uniform probability in the interval representing its limits of measurement. The range of epistemic uncertainties can be reduced through improved measurements [34].

Attention must be paid to the fundamental difference between polydisperse input parameters discussed in section 2.5 and aleatory or epistemic uncertainty of input parameters. Although both quantities are described by their distributions, uncertainty concerns monodisperse parameters (with the same value for all particles) or the moments (mean, variance...) of polydisperse parameter distributions. For example, particle size distribution is a polydisperse input but its mean value (mean particle size) can be an aleatory uncertain input with a distribution differing from that of particle sizes. Particle size distribution is part of the numerical material whereas mean particle size variability is an uncertainty due to measurement imprecision. In the same way, size span and the lower and upper bounds of all

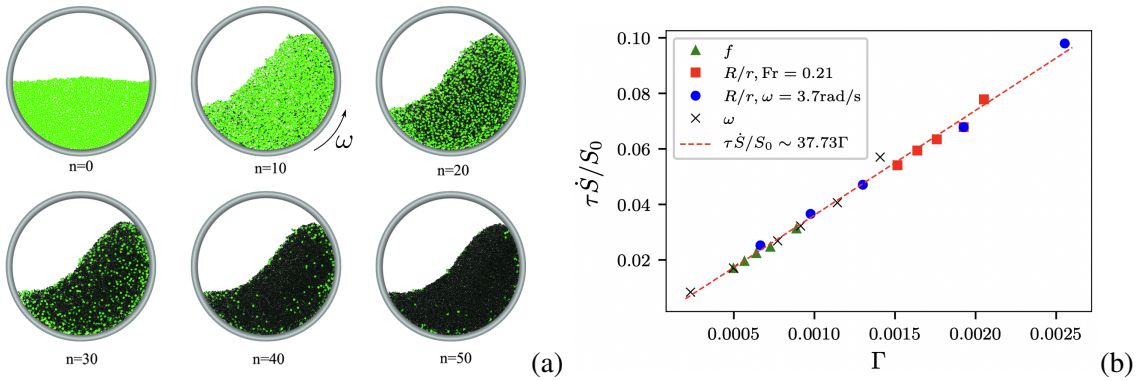

Figure 59: *(a) Snapshots of a rotating drum simulation for different numbers of rotations n. The color level is proportional to particle damage; (b) Normalized grinding rate as a function of the scaling parameter* Γ *defined by equation (29). [108].*

other parameters are mostly epistemic uncertainties.

Uncertainty quantification requires a set of simulations with different sets of the parameter values sampled in the input uncertainty space and the analysis of their combined impact on the values of selected output variables. This analysis is often called 'forward uncertainty propagation' [127, 34]. Uncertainty quantification is similar to local multivariate parametric (sensitivity) analysis. Assume that a system is described by a function $u = f(x)$, where $x = (x_1, \ldots, x_n)$ is the n-dimensional input and u is a scalar output. Let $u^* = f(x^*)$ be the solution for imput parameter x^*. Then, the sensitivity of the solution u^* with respect to x_k is estimated by the partial derivative $(\partial u/\partial x_k)_{x=x^*}$ [131]. This is a 'local' sensitivity analysis. The 'global' sensitivity analysis does not specify the input $x = x^*$, it considers the model $f(x)$ inside the n-dimensional box of input variables.

In DEM simulations, the underlying model is not a simple mathematical function, but a dynamic multi-body process combining particle interactions and equations of dynamics. Hence, for a global multivariate sensitivity analysis one has first to carry out extensive simulations to derive an expression of the output variable of interest as a function of the input parameters. For example, let us consider the grinding rate (the rate of increase of specific surface) in DEM simulations of grinding in the cascading regime in a rotating drum; see Fig. 59. 2D simulations using the bonded cell method lead to the following functional form [108]:

$$u = \tau\dot{S}/S_0 \simeq f(\Gamma) = 37.73\Gamma = 37.73\frac{1}{F}\left(\frac{R\omega^2}{g}\right)^{3/4}\left(\frac{R}{d_0}\right)^{1/4}\left(\frac{\rho_s g d_0}{C_n}\right)^{3/2}, \tag{29}$$

where $\tau\dot{S}/S_0$ is the normalized grinding rate, ω is rotation speed, R is drum radius, g is gravity, d_0 is the initial mean particle size, C_n is tensile particle strength, ρ_s is particle density, and $F = h_0/R$ is the initial normalized filling height. The reference time is

$$\tau = \frac{1}{g}\left(\frac{C_n}{\rho}\right)^{1/2}. \tag{30}$$

The function $u = f(\Gamma)$ is an approximate global model for the grinding rate obtained by varying independently most input parameters. Knowing the uncertainty in the value of the prefactor, this model makes it possible to evaluate analytically the uncertainty of grinding rate for each set of input values by simply using the partial derivatives of the function f.

Label	Model parameter			Range		
	Physical representation	Symbol	Units	Nominal	Min.	Max.
P_1	normal spring stiffness p-p (10^{P_1})	k_n	[N/m]	2.00	1.00	3.00
P_2	normal spring stiffness p-w (10^{P_2})	k_{nw}	[N/m]	2.00	1.00	3.00
P_3	friction coefficient p-p	μ	–	0.30	0.05	0.90
P_4	friction coefficient p-w	μ_w	–	0.30	0.05	0.90
P_5	normal restitution p-p	e_n	–	0.90	0.50	0.98
P_6	normal restitution p-w	e_{nw}	–	0.90	0.50	0.98
P_7	tangential-normal stiffness ratio p-p	k_t/k_n	–	0.29	0.10	0.90
P_8	tangential-normal stiffness ratio p-w	k_{tw}/k_{nw}	–	0.29	0.10	0.90
P_9	tangential-normal damping ratio p-p	η_t/η_n	–	0.50	0.10	0.90
P_{10}	tangential-normal damping ratio p-w	η_{tw}/η_{nw}	–	0.50	0.10	0.90
P_{11}	collision-DEM time-step ratio	τ_{col}/τ_{dem}	–	50	20	50
P_{12}	fluid equations tolerance ($10^{P_{12}}$)		–	−4.00	−6.00	−3.00
P_{13}	DEM-fluid grid interpolation width		[d_p]	2.00	1.00	2.50

Figure 60: *Model parameters considered for sensitivity analysis of CFD-DEM simulations of gas-solid pulsating fluidized beds. p-p and p-w represent particle-particle and particle-wall collision parameters, respectively [9].*

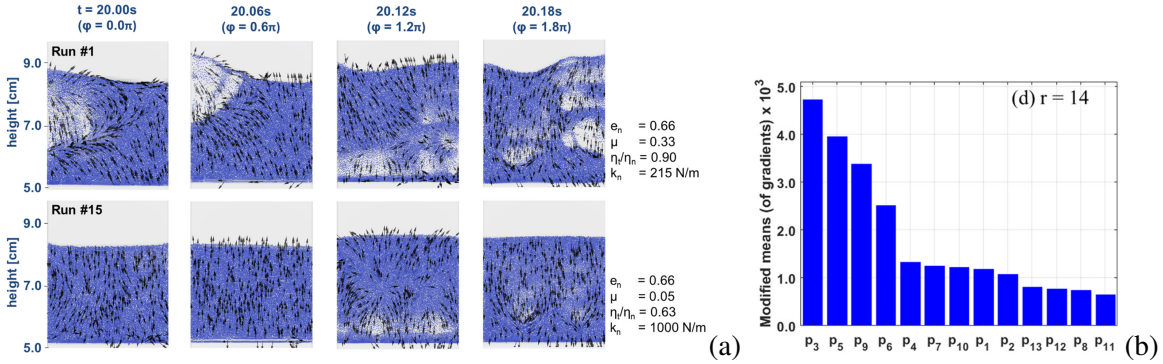

Figure 61: *Bubbling dynamics overlayed with particle velocity vectors along the central vertical slice in 3D CFD-DEM simulations. Key model parameters for each simulation are listed on the right. ϕ corresponds to phase of plenum inlet gas flow. (b) Sensitivity analysis of average bubble diameter. Input model parameters P_1 through P_{13} are ranked in order of decreasing sensitivity [9].*

When a neat functional form is not available, the partial derivatives are replaced by their discrete forms. For example, in Morris-One-At-a-Time (MOAT) screening method, the first sample is chosen randomly and each subsequent sample is picked by changing one parameter at a time (random walk), so that the elementary effect F_i of each input parameter P_i on the output y is defined as the gradient $F_i = [y(x+\Delta e_i) - y(x)]/\Delta$, where e_i is unit vector along the i^{th} direction [9]. The sensitivity is then given by the mean and standard deviation of the distribution of F_i for a number of replications. For example, this method was applied to 3D CFD-DEM simulations of a pulsating fluidized bed [9]. The bed dynamics in this system is dominated by alternating bubble rise and granular relaxation mechanisms as the superficial gas flow oscillates. The input parameters are given in Fig. 60. Snapshots of the fluidized bed and a ranking of the input parameters according to the evaluated uncertainty for each parameter are displayed in Fig. 61. In this example, the inter-particle friction P_3, normal restitution P_5, tangential-normal damping ratio P_9 and particle-wall normal restitution coefficient P_6 have the strongest influence on bubble sizes. More generally, based on more quantities of interest representing the bubble and particle dynamics, it was found that the normal spring-stiffness, normal restitution, friction and tangential damping coefficients were the key parameters impacting fluidization hydrodynamics and the influence of dissipation parameters was strongly coupled.

A rigorous framework for uncertainty quantification was applied to CFD-DEM simulations of the

Parameter	Lower bound	Base case	Upper bound	Type
HDPE particle diameter (cm)	0.898389	0.943045	0.953396	aleatory
HDPE density (g/cm^3)	0.93	0.95	0.97	epistemic
Glass particle diameter (cm)	0.270057	0.310134	0.340163	aleatory
Glass density (g/cm^3)	2.2835	2.513	2.85	epistemic
Glass-glass coeff of restitution	0.926186	0.969565	0.993185	aleatory
Glass-wall coeff of restitution	0.629237	0.954934	0.989071	aleatory
Sphericity, all particles	0.848242	0.936138	0.947962	aleatory
HDPE-glass coeff of restitution	0.741038	0.822966	0.840229	aleatory
Particle-particle coeff of friction	0.131000	0.273370	0.414350	aleatory
Particle-wall coeff of friction	0.057700	0.251369	0.382600	aleatory
Air temperature (K)	287.59	293.15	298.71	epistemic
Atmospheric pressure (psia)	12	12.15	12.45	epistemic
Viscosity (g/cm-s x 10^{-4})	1.78	1.81	1.84	known, from T
Raw flow measurement (SCFM)	3.436	3.6	3.764	indirect
Meter pressure (psig)	11.9	12.5	13.1	indirect
Gas mass rate variation (g/s)	−0.159	0	0.159	epistemic

Figure 62: *Uncertain input parameters of a fluidized bed containing a larger particle (HDPE particle) [34].*

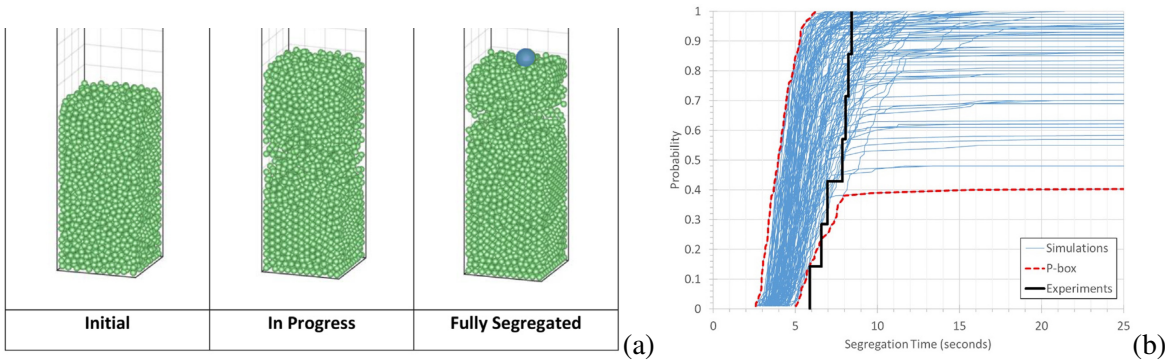

Figure 63: *(a) Snapshots of the segregation of a particle in a fluidized bed simulation; (b) Cumulative distribution function of segregation time for 127 sampled sets of values of uncertain epistemic parameters, each simulation repeated 100 times for different values of aleatory input parameters [34].*

segregation of a single large particle in a fluidized bed of smaller glass particles [34]. The base-case (most likely) values of input parameters, boundary conditions, and gas-phase flow conditions were provided by experiments. Fig. 62 summarizes the uncertain model input parameters for the fluidized bed, including the base-case value, lower bound, upper bound, and uncertainty type. The full-sampling of the uncertainty parameter space required sampling five epistemic inputs and eight aleatory inputs. As a first step, a total of $5^3 + 2 = 127$ epistemic sample points were selected, as recommended by the UQ framework, using the Latin Hypercube Sampling technique. In order to ensure the entire range of each epistemic uncertainty was sampled, the epistemic points with the lowest and highest values for an epistemic uncertainty were adjusted to match the low bound and high bound values for that uncertainty. At each of the 127 epistemic sample points, a Monte Carlo technique was then used to sample the cumulative distribution function for each aleatory input 100 times. Thus, in total, 12,700 simulations were required to complete the input propagation.

Figure 63 displays the cumulative distribution functions (CDF) of the segregation time for the 127 epistemic sample points. These results show a wide spread in the possible segregation times. Infinite segregation times are observed in simulations in which the particles do not move at all (no fluidization). The envelope representing the bounding values of the CDFs is referred to the probability-

box or *p-box*. The p-box graphically represents the full range of uncertainty in the segregation time as a result of the uncertainty in the 13 uncertain inputs. Interpreting a p-box can be challenging since it represents a collection of underlying CDFs that are each equally likely. A p-box can be read vertically to give a range of probabilities for a given outcome or horizontally to give a range of outcomes for a prescribed probability. Using the figure, one could state, for example, that the probability that the segregation time is 6 s or less is between 15% and 98% (read vertically). Likewise, one could read the p-box and infer that there is a 30% probability that the segregation time will not exceed a value between 3.5 s and 7.5 s (read horizontally).

Figure 63 also includes the CDF for the segregation time as observed in the experiments. Comparing the experimental CDF against the p-box of results suggests that there is a disparity between the simulations and experiments, with DEM simulations biased toward more rapid segregation than observed in the experiments. This disparity reveals an error in DEM modeling of the system or *model form* error. This disparity can also be related to an error in the identification of input parameter uncertainties. The large number of simulations needed to arrive at such a detailed quantification of the output uncertainty is prohibitive for the application of full-sampling method to DEM simulations of large systems. However, this methodology can be combined with sensitivity analysis to remove the least uncertain parameters from the analysis thereby reducing the number of simulations. The UQ can also be limited to the bounding values of the output variable. This boundary-sampling method attempts to identify two sets of uncertain input values for each key model output, one set that will lead to the minimum value of the key model output and one set that will lead to a maximum value of the key model output. The values for the uncertain inputs for each set are selected by noting, for each uncertain input, which values in the simple sensitivity analysis (e.g., the low-bound, base-case, or upper-bound) resulted in the lowest/highest values of the model output. The uncertain input values that resulted in the lowest values of the model output are assembled into one set, and an analogous approach is used to generate the set that should maximize the model output.

The numerical approximation errors are difficult to estimate accurately and in most cases they should be converted to and explicitly represented as epistemic uncertainties [127]. The simplest method for converting error estimates to uncertainties consists in adding the magnitude of the error estimate as uncertainty bands above and below the simulation prediction. Uncertainty due to numerical approximation error is epistemic since additional information (e.g., mesh levels, iterations, digits of precision) could be added to reduce it. When treating epistemic uncertainties as intervals, the proper mathematical method for combining uncertainties due to discretization, incomplete iteration, and round-off is to simply sum the intervals.

The foregoing example concerns only the monodisperse uncertain input data. Polydisperse input parameters can be subject to high approximation errors. For example, polydisperse particle sizes are generally represented by considering a mixture of several size classes, the particles being of the same size in each class [101, 145]. This discretization of the range of particle sizes into several classes is statistically representative only if there is a large enough number of different size classes and a large enough number of particles in each class. An optimal discretization requires both the representativity of large particles in number and the representativity of small particles in volume. Depending on the shape of the particle size distribution, a statistically representative sample may require a large number of small particles. The output parameters such as the solid fraction are sensitive to a lack of representativity. Similar remarks apply to other parameters subject to polydispersity such as friction coefficient and particle shape.

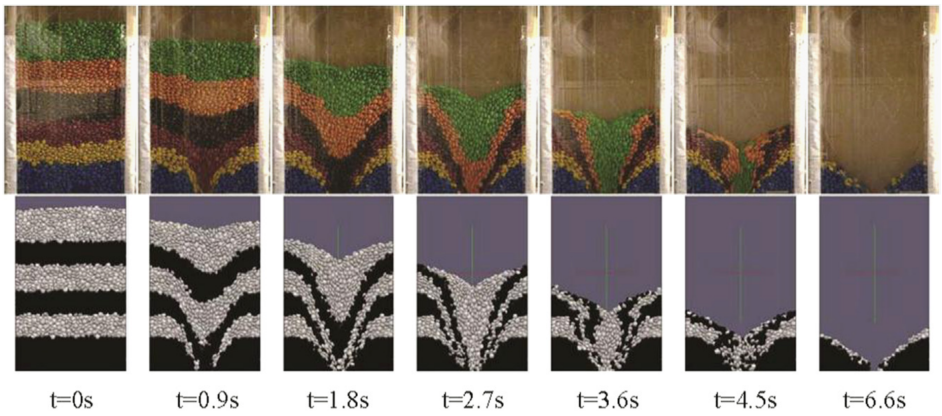

Figure 64: *Comparison of discharge flow of ellipsoidal particles between DEM simulation and experiment [81].*

7.3 Validation

In recent years, there has been a growing interest in experimental validation of DEM simulations. Many examples of direct validation by comparison of DEM simulations with experimental data can be found in the literature. In most cases, the experimental material is tailored to be a proxy of the numerical material and the calibration of input data has been based on simple experiments. In almost all such cases the comparison is successful, showing the fundamentally high fidelity of DEM simulations. For example, similar discharge rate was found between experiment and DEM simulation for ellipsoidal particles [81]; see Fig. 64. In the same way, similar bed heights were obtained for fluidized polyhedral particles [84]. However, in some cases the results are only partially validated. For example, higher strength was obtained for reduced sphericity and/or increased elongation in hopper flow but the measured strength in experiments was lower in simulations [62]. In this example, residual particle motions were reported in the particle bed, hinting to a stability problem.

A rigorous validation approach requires uncertainty quantification and adequate metrics for measuring the 'distance' between simulation output and experimental measurement. A *validation metric* requires the experimental measurements of the output variables of interest and the model prediction at the conditions used in the experimental measurements [127]. In the ideal case, the validation metric is computed using specially-tailored validation experiments; but more commonly one must use existing experimental data. A key requirement for computing the output variable of interest is that the uncertainty in all model input parameters should be carefully measured during the experiment. Once the input uncertainties have been quantified, they are used as input to the model and propagated through it to obtain the variable of interest. Depending on the nature of the model input uncertainties, the output will be a CDF, an interval, or a p-box, as illustrated above. The key point is that when they are propagated through the model, the model is expected to predict the experimentally measured variability in the output data. Any disagreement between the experimentally measured and simulated output variable is attributed to model form uncertainty, the source of which can be either physics modeling assumptions and/or imprecise knowledge of the input uncertainties.

While there are many possible validation metrics, let us consider the so-called *area validation metric*. When only aleatory uncertainties are present in the model inputs, then propagating these uncertainties through the model produces a CDF of the output variable of interest. Experimental measurements are then used to construct another empirical CDF of the same variable. The area between

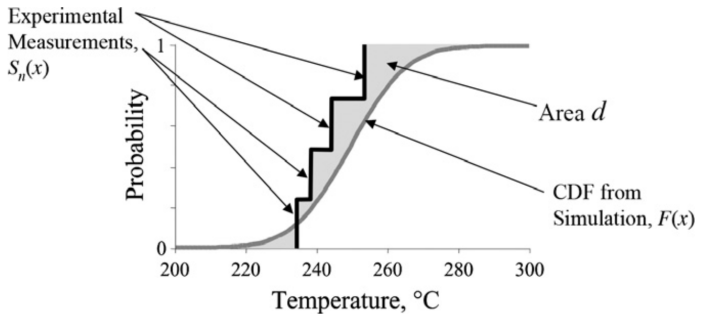

Figure 65: *Area validation metric example with four experimental measurements of the output variable of interest [127].*

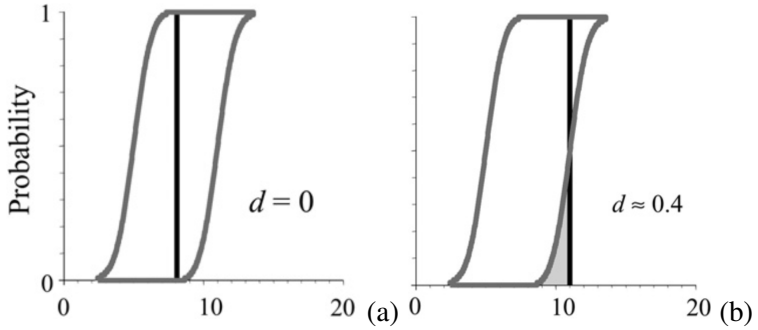

Figure 66: *Examples of area validation metric in the cases where the model prediction is a p-box and only a single experimental measurement is available [127].*

these two CDFs is referred to as the area validation metric d (also called the Minkowski L_1 norm) and is given by [127]

$$d(F,S_n) = \int_{-\infty}^{\infty} |F(x) - S_n(x)| dx, \tag{31}$$

where $F(x)$ is the CDF from the simulation, $S_n(x)$ the CDF from the experiment, and x is the output variable of interest. The area validation metric d has the same units as the variable of interest and effectively provides a measure of disagreement between the simulation and the experiment. It should be noted that the area validation metric satisfies all the conditions for a distance function on a metric space; see Fig. 65.

When little experimental information is available on needed model input parameters, these parameters should be characterized as an interval, i.e., epistemic uncertainties. This situation occurs very commonly with published experimental data and experiments that were not designed to be validation experiments. As a result, when these intervals are propagated through the model, the predicted variable of interest is represented as a p-box. The validation metric can also deal with this situation. Fig. 66 shows the case where the model prediction is a p-box and only a single experimental measurement is available. Fig. 66(a) occurs when the measurement falls entirely within the p-box and Fig. 66(b) occurs when the measurement is slightly larger than the p-box. When the experimental measurement falls entirely within the simulation's p-box, the area validation metric is zero. When a portion of the experimental measurement falls outside of the p-box, the area validation metric is nonzero. It is noteworthy that when the simulation is a p-box due to insufficient information provided by the validation experiment, the model is given more leeway in comparing with the experiment, as

is appropriate. The validation metric can be extrapolated to conditions where experimental data are not available. This extrapolation accounts only for the model form error. When the validation metric results are extrapolated to new conditions, there is a subsequent increase in the uncertainty due to the extrapolation process itself, i.e., the standard error of the regression fit increases as one moves away from the central region of the available data.

The reader is referred to the cited publications for more details on the predictive uncertainty framework. A brief reproduction of the concepts of this framework in this section was meant to underline the importance of a rigorous approach to validation in DEM simulations. In fact, uncertainty quantification and validation are necessary to assess the reliability of DEM and the trustworthiness of the softwares used for simulations. This issue is open to extensive investigation for many quantities of interest in granular materials, both at the process scale and at the mesoscopic scales. The application of the uncertainty framework can provide valuable information about the predictive power and algorithmic insufficiencies of DEM for dealing with advanced applications involving various particle shapes, particle breakage, soft particles, and ploydisperse systems (in the broad sense).

We began this report with remarks about the epistemological role and physics fidelity of DEM. Full respect of this role means *calibrating the input parameters only at the particle scale* (no adjustment from macroscopic measurements) and comparing quantitatively the output variables with experiments. Predictive uncertainty quantification provides the key tools for this task [106]. By allowing for model form uncertainty assessment, UQ prevents from inconsistent calibration of DEM parameters, i.e. multiple calibrations adjusted to different experiments, and makes it possible to focus on the predictive power of DEM. This is as much crucial for the practice of DEM and its application to real-world problems in the future as model developments to increase its physics fidelity. *The reliability of DEM as a predictive tool is best demonstrated when it fails under circumstances for which its underlying model was not designed*. For example, a DEM-based model with spherical particles *must* fail when applied to simulate a system composed of elongated particles. The concern should not therefore be about adjusting the input parameters to reproduce the real material behavior, but about the ability of measuring the 'distance' between simulation output and experimental measurement. This is an obvious fact which has been partially undermined by the increasing complexity of the numerical material and technicality of computational algorithms with a *trend to underestimate the nature of DEM as a bottom-up simulation tool*. We need therefore to re-define the metrics for an objective measurement of both the power and weaknesses of DEM.

8 Outlook: Horizons of DEM

Game-changing advances

How will dry granular modeling evolve in near future? There is no simple answer to this question. The focus of this report has been on DEM as a high-fidelity bottom-up approach which continues to occupy a central place in modeling granular materials and linking theory with experiment. We extensively underlined this particular role of DEM, sometimes taking the features of an upscaling theory and sometimes passing for numerical experiment. This duality reflects the object-based Lagrangian nature of DEM in which the simulated particles and their interactions define the input parameters and the output is the collective dynamic behavior.

Schematically, the collective dynamics arising from interactions has been at the focus of research whereas the input parameters and their impact on the dynamics and system reponse quantities have been the highest concern for real-world applications. The goal of the former is the modeling of the *generic* behavior of granular materials while the latter is interested in the *specific* features depending on the model material. The generic behavior has been a drive for the *basic DEM* developments and its extensions. The *advanced DEM* developments, on the other hand, have been driven by the need for higher physics fidelity of the numerical material and higher computational efficiency. We overviewed significant advances made in modeling contact interactions, particle shapes, breakable particles, and soft particles, as well as in computational and validation methods.

Particle shape representation and contact detection have been well developed by many independent researchers and applied to investigate real-world problems. In particular, polyhedral representation (PH-DEM) and level-set representation (LS-DEM) can be used to model arbitrary shapes extracted from 3D CT scans with corresponding contact detection methods and data structures. These robust algorithmic solutions have also opened the path to the models of particle breakage (BPM) and soft particles (SD-DEM). However, in DEM simulations using these advanced models of particle shape, contact mechanics considerations such as Hertz contact for smooth rounded particles have been replaced by penalty-based practical considerations.

DEM simulations incorporating these new algorithms require much higher computational power which has been essentially provided by parallel computing and the GPU technology. Computational efficiency can be equally used to speed up simulations, to increase the number of particles, or to increase the number of degrees of freedom per particle in hybrid models based on sub-particle continuum fields (C-DEM) for particle fragmentation and deformation. Efficient hybrid methods have also been designed for multiscale simulation in which the granular material is essentially modeled as a continuum phase field, and discrete particles replace material points only where and when particle-level resolution is necessary (shear bands, close to wall boundaries, etc).

We may qualify each major resource of DEM according to its contribution to enhance physics fidelity, highlight data fidelity, increase numerical efficiency, or enable a game-changing approach. Fig. 67 summarizes these contributions for the techniques and methods that have been mentioned in this report. ML and UQ are generic tools that can be applied with all other techniques. LS-DEM and PH-DEM are alternative high-fidelity approaches which will have a central place in future developments in application to real-shaped materials, soft particles (in association with SD-DEM), and breakable particles (in association with BCM).

Technique	Physics fidelity	Data fidelity	Efficiency	Game-changing
Multiscale hybrid			X	X
C-DEM hybrid	X			X
LS-DEM	X	X		X
PH-DEM	X	X		X
CDM	X			X
SD-DEM	X	X		X
BPM, BCM	X			
ML	X	X	X	X
UQ	X	X		
Parallel computing, GPU			X	
Particle coarsening			X	

Figure 67: *Contributions of different techniques to physics fidelity, data fidelity, and efficiency of DEM and its game-changing potential. Abbreviations: C for continuum representation of particles, LS for Level Set, PH for Polyhedral, CDM for Contact Dynamics Method, SD for Surface Deformation, BPM for Bonded Particle Method, BCM for Bonded Cell Method, ML for Machine Learning, and UQ for Uncertainty Quantification.*

Beyond hard-particle assumption

All these developments have gradually pushed the limits of DEM beyond the hard-particle assumption. Depending on how particle strains are treated, four variants of DEM can be distinguished:

1. Contact strain: In conventional DEM, the elastic or plastic strains are concentrated at the contact points between particles. The overlap distance or volume represents the normal strain component and cumulative tangential displacement represents the tangential strain component.

2. Sub-particle strain (C-DEM): The sub-particle strain in soft or breakable particles is represented as a field described by continuum equations.

3. Particle surface strain (SD-DEM): The strain is carried by material points located at the particle surface and coupled with a uniform strain field inside the particle.

4. Mesoscale strain (Hybrid Multiscale): In multiscale modeling, the strain is carried by mesoscale elements (grid level) containing a number of particles.

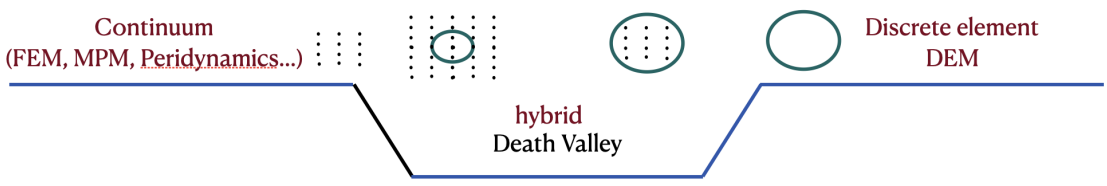

Figure 68: *The valley of hybrid methods.*

It is noteworthy that contact-level strain can in principle be used in parallel with other strains. However, when the strains are carried by the surface or volume material points, it is more consistent

to treat contacts as constraints by using the framework of the contact dynamics method (CDM). This method may be considered as an alternative approach which is able to enforce unilateral contact and Coulomb friction law based on gap distance between particles with the advantage of being independent of particle shape. This corresponds to a paradigm shift from a *hard-particle soft-contact* scheme of the conventional DEM to a *soft-particle hard-contact* scheme. In this scheme, the material behavior (elastic, plastic) is fully carried by the particles, and the conditions of impenetrability of the particles and Coulomb friction law are enforced by CDM. This shift can remove at the same time the ambiguities of the implementation of friction law and normal force positivity previously discussed. Regarding hybrid models (both multiscale and C-DEM), robust hybridization methods are needed beyond simple coupling of the velocity fields. In particular, the state variables and force fields must be matched to ensure time-space continuity of the governing equations; see Fig. 68.

Data-driven DEM

Machine Learning techniques may also deeply transform the framework and practice of DEM for the simulation of granular materials. This can prompt a shift from advanced DEM towards a *data-driven DEM*. This transformation will be a huge step towards a digital twin of granular processes by blending experimental data with discrete element modeling, calibration with validation, accuracy with computational efficiency, and flexibility with robustness. ML models may allow for thorough investigation of the dynamics of granular materials at intermediate scales between those of the particles and the process. In turn, such physical insights can be used to constrain the learning process. In this way, data-driven DEM can amplify the physics fidelity of simulations.

The relation of DEM with ML is to some extent similar to the relation between theory and DEM. In both cases, a two-way enrichment develops in time through research and practice. In this sense, ML is not fully disruptive for DEM, but opens the way to data-intensive computing. This data-driven paradigm of DEM provides a tremendous prospect although substantial developments are in order before it can be deployed in practice. In particular, ML can be used for the extraction of particle shapes and sizes as well as sample configuration from X-ray CT scans. Such data can be used to train an ML model for contact detection. Finally, ML can also be used for efficient calculation of forces and velocities, either replacing the force correction step or replacing Gauss-Seidel iterations in CDM. Fig. 69 illustrates how a series of CT scans of an evolving granular material can be used to train ML models for sample reconstruction and contact detection while CDM-calculated forces over a contact network represented as a graph make it possible to train graph-based ML models for force and velocity prediction to update particle positions. Furthermore, the predicted positions can be compared with reconstructed samples either for uncertainty quantification or for back-propagation of the information.

Besides ML, some of the methods and techniques developed in computational mechanics can potentially contribute to the development of data-driven DEM. We may define *data fidelity* as the quality of a method or technique to accurately digest or handle data extracted from real materials. For example, LS-DEM and PH-DEM present a high degree of data fidelity by representing and processing particle shape data from X-ray tomographic images. The methods capable of using efficiently those data can also be considered to have high data fidelity.

With enriched numerical material and enhanced physics-fidelity of DEM owing to these newly developed geometrical, mechanical, and computational techniques and resources, the risk of arbitrary matching of input parameters has been considerably reduced. There are, however, a multitude of sources of error which must be evaluated to quantify the uncertainty of simulation outputs. A rigor-

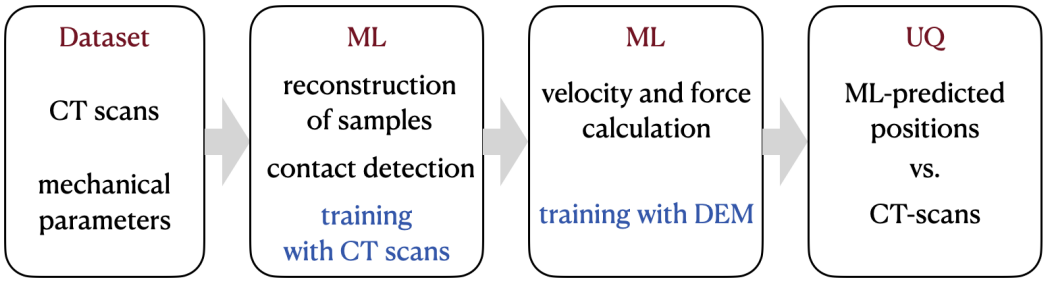

Figure 69: *X-ray CT scans and DEM used to train Machine Learning (ML) models for sample reconstruction, contact detection, and force and velocity calculation, as well as uncertainty quantification (UQ) by comparing ML predictions with the image data.*

ous uncertainty quantification (UQ) is the only way to determine the intervals of confidence in the results and to demonstrate the level of physics-fidelity and therefore reliability of a code or simulation by comparison with available experimental data. A UQ framework is most useful when applied to evaluate not only system response quantities but also particle scale quantities and their probability distributions such as the local dynamic and geometrical structures for which experimental data can be found or generated.

Most validation results published so far are not based on UQ and are limited to specific output variables. Given the systematic and approximation errors in the underlying algorithms of DEM and epistemic uncertainties of input parameters, full validation does not make sense. In principle, unless when only qualitative validation or verification is of interest, a quantitive validation method must be able to determine the degree of validation according to a *validation metric*. In this respect, the uncertainty associated with the new algorithms such as hybrid methods needs special attention since they involve new sources of uncertainty.

Concluding remarks

Discrete modeling of granular materials is about to reach *high levels of physics fidelity and data fidelity* at the cost of bypassing its own founding assumptions. The essence of this transition from basic DEM to advanced DEM and beyond, is a transition from qualitative realism to a quantitative realism of the simulation models. Thereby, advanced DEM simulations can now be compared with experiments without arbitrary adjustment of input parameters. By virtue of this higher realism, a rigorous uncertainty quantification framework can be applied to determine the intervals of confidence in the output simulation data. The newly-developed models and algorithms can also be benchmarked against real-world processes, and made available to a broader community.

Future developments will have to build on more sophisticated algorithms and data structures. In exception to the difference between the conventional DEM and CDM, all previous algorithms were essentially similar. In contrast, there is presently *a multitude of algorithms* that can be blended to build new DEM codes: LS-DEM for image-based simulations, PH-DEM and C-DEM (in association with FEM, MPM, peridynamics, and other continuum methods) for soft and breakable particles, CDM for force and velocity calculations, ML for contact detection and force calculation, BPM and PRM with enhanced breakage rules and fragment shape generation for breakable particles, and multiscale concurrent hybrid methods associating low computational cost of continuum field simulations with high physics fidelity of discrete particle simulations. A future challenge will therefore consist in *compar-*

ing different algorithms for their utility, physics fidelity, data fidelity, complexity, and performance. In all cases, parallel computing is the necessary condition to cope with higher computational cost of advanced and data-driven DEM.

As a final remark, consistent with the role of DEM as a method for discovery alongside theory and experiment, the novel algorithmic developments should not be expected to capture the rich physics of all granular materials. Most of these algorithms have been primarily developed to enrich DEM with novel ingredients (particle shape, particle softness, particle breakage, computational efficiency). There are, however, *several caveats related to contact interactions* that have strong bearing on the physics-fidelity of these algorithms and need therefore to be resolved. The implementation of the Coulomb friction law with a cumulative tangential displacement, the memory of plastic displacements in elastic-plastic normal contact models, the normal force positivity, the artificial surface roughness effects with polyhedral and level set representations, the multiple contacts between clumps, the use of overlap volume in normal force calculation for polyhedral particles, the polydisperse input parameters and their statistical representativity, and the role of contact stiffness in adhesion laws are among those issues. Hence, in spite of far-reaching developments underlying the giant step accomplished towards digital twins of granular materials, the field of discrete modeling of granular media is vast and open to numerous improvements in the future.

References

[1] R. Affes, J. Y. Delenne, Y. Monerie, F. Radjaï, and V. Topin. Tensile strength and fracture of cemented granular aggregates. *The European Physical Journal E*, 35(11):117, 2012.

[2] H. M. An, H. Y. Liu, Haoyu Han, Xin Zheng, and X. G. Wang. Hybrid finite-discrete element modelling of dynamic fracture and resultant fragment casting and muck-piling by rock blast. *Computers and Geotechnics*, 81:322–345, 2017.

[3] J. E. Andrade and X. Tu. Multiscale framework for behavior prediction in granular media. *Mechanics of Materials*, 41:652–669, 2009.

[4] J.E. Andrade, C.F. Avila, S.A. Hall, N. Lenoir, and G. Viggiani. Multiscale modeling and characterization of granular matter: From grain kinematics to continuum mechanics. *Journal of the Mechanics and Physics of Solids*, 59:237–250, 2011.

[5] Nicola Angius, Giuseppe Primiero, and Raymond Turner. The Philosophy of Computer Science. In Edward N. Zalta, editor, *The Stanford Encyclopedia of Philosophy*. Metaphysics Research Lab, Stanford University, spring 2021 edition, 2021.

[6] E. Azéma, G. Saussine, and F. Radjai. Quasistatic rheology, force transmission and fabric properties of a packing of irregular polyhedral particles. *Mechanics of Materials*, 41:729–741, 2009.

[7] Emilien Azéma and Farhang Radjai. Internal structure of inertial granular flows. *Phys. Rev. Lett.*, 112(7):078001–, February 2014.

[8] Emilien Azéma, Farhang Radjai, and Frédéric Dubois. Packings of irregular polyhedral particles: Strength, structure, and effects of angularity. *Phys. Rev. E*, 87:062203, Jun 2013.

[9] A. Bakshi, M. Shahnam, A. Gel, T. Li, C. Altantzis, W. Rogers, and A. F. Ghoniem. Comprehensive multivariate sensitivity analysis of cfd-dem simulations: Critical model parameters and their impact on fluidization hydrodynamics. *Powder Technology*, 338:519–537, 2018.

[10] G. W. Baxter and R. P. Behringer. Cellular automata models for granular flow. *Phys. Rev. A (Rapid Communication)*, 42(2):1017, 1990.

[11] Nathan Berry, Yonghao Zhang, and Sina Haeri. Contact models for the multi-sphere discrete element method. *Powder Technology*, 416:118209, 2023.

[12] C. Bizon, M. D. Shattuck, J. B. Swift, W. D. McCormick, and H. L. Swinney. Patterns in 3d vertically oscillated granular layers: Simulation and experiment. *Phys. Rev. Lett.*, 80(1):57–60, 1998.

[13] Nicolas Blanc, Xavier Frank, Farhang Radjai, Claire Mayer-Laigle, and Jean-Yves Delenne. Breakage of flawed particles by peridynamic simulations. *Computational Particle Mechanics*, 8(5):1019–1031, 2021.

[14] C. W. Boon, G. T. Houlsby, and S. Utili. A new algorithm for contact detection between convex polygonal and polyhedral particles in the discrete element method. *Computers and Geotechnics*, 44:73–82, 2012.

[15] I. Bratberg, F. Radjai, and A. Hansen. Dynamic rearrangements and packing regimes in randomly deposited two-dimensional granular beds. *Phys. Rev. E*, 66:031303–1, 2002.

[16] N. V. Brilliantov, F. Spahn, J. M. Hertzsch, and T. Pöschel. Model for collisions in granular gases. *Phys. Rev. E*, 53(5):5382, 1996.

[17] Nikolai V Brilliantov, Nicole Albers, Frank Spahn, and Thorsten Pöschel. Collision dynamics of granular particles with adhesion. *Phys Rev E Stat Nonlin Soft Matter Phys*, 76(5 Pt 1):051302, 2007.

[18] B Brogliato. *Nonsmooth mechanics*. Springer, London, 1999.

[19] Nicholas J Brown, Jian-Fei Chen, and Jin Y Ooi. A bond model for dem simulation of cementitious materials and deformable structures. *Granular Matter*, 16:299–311, 2014.

[20] Van H. Bui, Minh D. Bui, and Peter Rutschmann. Combination of discrete element method and artificial neural network for predicting porosity of gravel-bed river. *Water*, 11(7), 2019.

[21] D. Cantor, E. Azéma, P. Sornay, and F. Radjai. Three-dimensional bonded-cell model for grain fragmentation. *Computational Particle Mechanics*, 4(4):441–450, 2017.

[22] David Cantor, Emilien Azéma, Philippe Sornay, and Farhang Radjai. Rheology and structure of polydisperse three-dimensional packings of spheres. *Phys. Rev. E*, 98:052910, Nov 2018.

[23] Hanqiao Che, Dominik Werner, Jonathan Seville, Tzany Kokalova Wheldon, and Kit Windows-Yule. Evaluation of coarse-grained cfd-dem models with the validation of pept measurements. *Particuology*, 82:48–63, 2023.

[24] Peter Yichen Chen, Maytee Chantharayukhonthorn, Yonghao Yue, Eitan Grinspun, and Ken Kamrin. Hybrid discrete-continuum modeling of shear localization in granular media. *Journal of the Mechanics and Physics of Solids*, 153:104404, 2021.

[25] Xizhong Chen and Junwu Wang. Hybrid discrete-continuum model for granular flow. *Procedia Engineering*, 102:661–667, 2015.

[26] Xizhong Chen, Junwu Wang, and Jinghai Li. Multiscale modeling of rapid granular flow with a hybrid discrete-continuum method. *Powder Technology*, 304:177–185, 2016.

[27] Samuel Clarke, Travers Rhodes, Christopher G. Atkeson, and Oliver Kroemer. Learning audio feedback for estimating amount and flow of granular material. In Aude Billard, Anca Dragan, Jan Peters, and Jun Morimoto, editors, *Proceedings of The 2nd Conference on Robot Learning*, volume 87 of *Proceedings of Machine Learning Research*, pages 529–550. PMLR, 29–31 Oct 2018.

[28] P. W. Cleary. Recent advances in dem modelling of tumbling mills. *Minerals Engineering*, 14(10):1295–1319, 2001.

[29] P. W. Cleary. Review of dem for industrial applications. Technical report, International Fine Particle Research Institute, 2010.

[30] Paul W. Cleary, Gary W. Delaney, Matt D. Sinnott, Sharen J. Cummins, and Rob D. Morrison. Advanced comminution modelling: Part 1 - crushers. *Applied Mathematical Modelling*, 88:238–265, 2020.

[31] Corné J. Coetzee and Otto C. Scheffler. Review: The calibration of dem parameters for the bulk modelling of cohesive materials. *Processes*, 11(1), 2023.

[32] P. A. Cundall and O. D. L. Strack. A discrete numerical model for granular assemblies. *Géotechnique*, 29(1):47–65, 1979.

[33] Frédéric da Cruz, Sacha Emam, Michaël Prochnow, Jean-Noël Roux, and François Chevoir. Rheophysics of dense granular materials: discrete simulation of plane shear flows. *Phys. Rev. E*, 72(2 Pt 1):021309, Aug 2005.

[34] Steven R. Dahl, W. Casey Q. LaMarche, Peiyuan Liu, William D. Fullmer, and Christine M. Hrenya. Toward reducing uncertainty quantification costs in dem models of particulate flow: Testing simple, sensitivity-based, forward uncertainty propagation techniques. *Powder Technology*, 398:117136, 2022.

[35] Alan A de Arruda Tino and Luís Marcelo Tavares. Simulating breakage tests using the discrete element method with polyhedral particles. *Computational Particle Mechanics*, pages 1–13, 2022.

[36] Jean-Yves Delenne, Moulay Saïd El Youssoufi, Fabien Cherblanc, and Jean-Claude Bénet. Mechanical behaviour and failure of cohesive granular materials. *International Journal for Numerical and Analytical Methods in Geomechanics*, 28(15):1577–1594, 2004.

[37] Yann Dufresne, Micaël Boulet, and Stéphane Moreau. Energy dissipation and onset of instabilities in coarse-grained discrete element method on homogeneous cooling systems. *Physics of Fluids*, 34(3):033306, 2022.

[38] Jérôme Duriez and Stéphane Bonelli. Precision and computational costs of level set-discrete element method (ls-dem) with respect to dem. *Computers and Geotechnics*, 134:104033, 2021.

[39] Bonabeau E. Agent-based modeling: methods and techniques for simulating human systems. *Proc Natl Acad Sci U S A.*, 2002.

[40] Jan Eliáš. Simulation of railway ballast using crushable polyhedral particles. *Powder Technology*, 264:458–465, 2014.

[41] Nicolas Estrada, Emilien Azéma, Farhang Radjai, and Alfredo Taboada. Identification of rolling resistance as a shape parameter in sheared granular media. *Phys. Rev. E*, 84:011306, Jul 2011.

[42] Nicolas Estrada, Alfredo Taboada, and Farhang Radjai. Shear strength and force transmission in granular media with rolling resistance. *Phys. Rev. E*, 78, 2008.

[43] S. Fazekas, J. Török, and J. Kertész. Critical packing in granular shear bands. *Phys Rev E Stat Nonlin Soft Matter Phys*, 75(1 Pt 1):011302, Jan 2007.

[44] Y. T. Feng. Thirty years of developments in contact modelling of non-spherical particles in dem: a selective review. *Acta Mechanica Sinica*, 39(1):722343, 2023.

[45] Y. T. Feng and Yuanqiang Tan. The minkowski overlap and the energy-conserving contact model for discrete element modeling of convex nonspherical particles. *Int J Numer Methods Eng*, 122(22):6476–6496, November 2021.

[46] YT Feng. An energy-conserving contact theory for discrete element modelling of arbitrarily shaped particles: Basic framework and general contact model. *Computer Methods in Applied Mechanics and Engineering*, 373:113454, 2021.

[47] Yuntian Feng. A generic energy-conserving discrete element modeling strategy for concave particles represented by surface triangular meshes. *Int J Numer Methods Eng*, 122(10):2581–2597, May 2021.

[48] Jean-Francois Ferellec and Glenn R. McDowell. A method to model realistic particle shape and inertia in dem. *Granular Matter*, 12(5):459–467, 2010.

[49] Xavier Frank, Farhang Radjaï, Saied Nezamabadi, and Jean-Yves Delenne. Tensile strength of granular aggregates: Stress chains across particle phase versus stress concentration by pores. *Phys. Rev. E*, 102:022906, Aug 2020.

[50] Alfredo Gay Neto, Blaž Hudobivnik, Tiago Fernandes Moherdaui, and Peter Wriggers. Flexible polyhedra modeled by the virtual element method in a discrete element context. *Computer Methods in Applied Mechanics and Engineering*, 387:114163, 2021.

[51] GDR-MiDi. On dense granular flows. *Eur. Phys. J. E*, 14:341–365, 2004.

[52] Nicolin Govender, Raj K. Rajamani, Schalk Kok, and Daniel N. Wilke. Discrete element simulation of mill charge in 3d using the blaze-dem gpu framework. *Minerals Engineering*, 79:152–168, 2015.

[53] Nicolin Govender, Daniel N. Wilke, Schalk Kok, and Rosanne Els. Development of a convex polyhedral discrete element simulation framework for nvidia kepler based gpus. *Journal of Computational and Applied Mathematics*, 270:386–400, 2014.

[54] Nicolin Govender, Daniel N. Wilke, Chuan-Yu Wu, Johannes Khinast, Patrick Pizette, and Wenjie Xu. Hopper flow of irregularly shaped particles (non-convex polyhedra): Gpu-based dem simulation and experimental validation. *Chemical Engineering Science*, 188:34–51, 2018.

[55] Yile Gu, Ali Ozel, and Sankaran Sundaresan. A modified cohesion model for cfd–dem simulations of fluidization. *Powder technology*, 296:17–28, 2016.

[56] Ning Guo and Jidong Zhao. A coupled fem/dem approach for hierarchical multiscale modelling of granular media. *Int. J. Numer. Meth. Engng*, 99:789?818, 2014.

[57] Ning Guo and Jidong Zhao. Multiscale insights into classical geomechanics problems. *Int. J. Numer. Anal. Meth. Geomech.*, 40:367?390, 2016.

[58] Matt Harrington, Andrea J. Liu, and Douglas J. Durian. Machine learning characterization of structural defects in amorphous packings of dimers and ellipses. *PRE*, 99(2):022903, February 2019.

[59] Y. He, T. J. Evans, A. B. Yu, and R. Y. Yang. A gpu-based dem for modelling large scale powder compaction with wide size distributions. *Powder Technology*, 333:219–228, 2018.

[60] H. J. Herrmann and S. Luding. Modeling granular media with the computer. *Continuum Mechanics and Thermodynamics*, 10:189–231, 1998.

[61] Soohwan Hwang, Jianhua Pan, Ashin A. Sunny, and Liang-Shih Fan. A machine learning-based particle-particle collision model for non-spherical particles with arbitrary shape. *Chemical Engineering Science*, 251:117439, 2022.

[62] D. Höhner, S. Wirtz, and V. Scherer. A study on the influence of particle shape on the mechanical interactions of granular media in a hopper using the discrete element method. *Powder Technology*, 278:286–305, 2015.

[63] C. T. Jayasundara and H. P. Zhu. Predicting liner wear of ball mills using discrete element method and artificial neural network. *Chemical Engineering Research and Design*, 182:438–447, 2022.

[64] M. Jean. The non-smooth contact dynamics method. *Computer methods in applied mechanics and engineering*, 177:235–257, 1998.

[65] Mingjing Jiang, He Chen, Mauricio Tapias, Marcos Arroyo, and Rui Fang. Study of mechanical behavior and strain localization of methane hydrate bearing sediments with different saturations by a new dem model. *Computers and Geotechnics*, 57:122–138, 2014.

[66] Zhaohua Jiang, Takuya Tsuji, Kimiaki Washino, and Toshitsugu Tanaka. Influence of model particle size and spatial resolution in coarse-graining dem-cfd simulation. *Advanced Powder Technology*, 32(10):3525–3539, 2021.

[67] Narcés Jiménez-Herrera, Gabriel K. P. Barrios, and Luís Marcelo Tavares. Comparison of breakage models in dem in simulating impact on particle beds. *Advanced Powder Technology*, 29(3):692–706, 2018.

[68] K. Kamrin and G. Koval. Nonlocal constitutive relation for steady granular flow. *Phys. Rev. Lett.*, 108:178301, 2012.

[69] George Em Karniadakis, Ioannis G. Kevrekidis, Lu Lu, Paris Perdikaris, Sifan Wang, and Liu Yang. Physics-informed machine learning. *Nature Reviews Physics*, 3(6):422–440, 2021.

[70] Reid Kawamoto, Edward Andò, Gioacchino Viggiani, and José E Andrade. Level set discrete element method for three-dimensional computations with triaxial case study. *Journal of the Mechanics and Physics of Solids*, 91:1–13, 2016.

[71] Reid Kawamoto, Edward Andò, Gioacchino Viggiani, and José E Andrade. All you need is shape: Predicting shear banding in sand with ls-dem. *Journal of the Mechanics and Physics of Solids*, 111:375–392, 2018.

[72] Alireza Khazeni and Zahra Mansourpour. Influence of non-spherical shape approximation on dem simulation accuracy by multi-sphere method. *Powder Technology*, 332:265–278, 2018.

[73] Tomonari Kobayashi, Toshitsugu Tanaka, Naoki Shimada, and Toshihiro Kawaguchi. Dem–cfd analysis of fluidization behavior of geldart group a particles using a dynamic adhesion force model. *Powder technology*, 248:143–152, 2013.

[74] N. P. Kruyt and L. Rothenburg. Kinematic and static assumptions for homogenization in micromechanics of granular materials. *Mechanics of Materials*, 36(12):1157–1173, December 2004.

[75] Rishi Kumar, Sarshad Rommel, David Jauffrès, Pierre Lhuissier, and Christophe L Martin. Effect of packing characteristics on the discrete element simulation of elasticity and buckling. *International Journal of Mechanical Sciences*, 110:14–21, 2016.

[76] M. Kwapinska, G. Saage, and E. Tsotsas. Mixing of particles in rotary drums: A comparison of discrete element simulations with experimental results and penetration models for thermal processes. *Powder Technology*, 161(1):69–78, 2006.

[77] Zhengshou Lai and Qiushi Chen. Reconstructing granular particles from x-ray computed tomography using the tws machine learning tool and the level set method. *Acta Geotechnica*, 14(1):1–18, 2019.

[78] Zhengshou Lai, Qiushi Chen, and Linchong Huang. Machine-learning-enabled discrete element method: Contact detection and resolution of irregular-shaped particles. *International Journal for Numerical and Analytical Methods in Geomechanics*, 46(1):113–140, January 2022.

[79] John-Paul Latham, Antonio Munjiza, Xavier Garcia, Jiansheng Xiang, and Romain Guises. Three-dimensional particle shape acquisition and use of shape library for dem and fem/dem simulation. *Minerals Engineering*, 21(11):797–805, 2008.

[80] Hadrien Laubie, Farhang Radjaï, Roland Pellenq, and Franz-Josef Ulm. A potential-of-mean-force approach for fracture mechanics of heterogeneous materials using the lattice element method. *Journal of the Mechanics and Physics of Solids*, 105:116–130, 2017.

[81] Peiyuan Liu and Christine M. Hrenya. Challenges of dem: I. competing bottlenecks in parallelization of gas-solid flows. *Powder Technology*, 264:620–626, 2014.

[82] Peiyuan Liu, Casey Q LaMarche, Kevin M Kellogg, and Christine M Hrenya. Fine-particle defluidization: Interaction between cohesion, young's modulus and static bed height. *Chemical Engineering Science*, 145:266–278, 2016.

[83] Xiaoyu Liu, Mostafa Sulaiman, Jari Kolehmainen, Ali Ozel, and Sankaran Sundaresan. Particle-based coarse-grained approach for simulating dry powder inhaler. *International Journal of Pharmaceutics*, 606:120821, 2021.

[84] Zihan Liu, Huaqing Ma, and Yongzhi Zhao. Cfd-dem simulation of fluidization of polyhedral particles in a fluidized bed. *Energies*, 14(16), 2021.

[85] M. Y. Louge. Computer simulations of rapid granular flows of spheres interacting with a flat, frictional boundary. *Phys. Fluids*, 6(7):2253–2269, 1994.

[86] G. Lu, J. R. Third, and C. R. Müller. Critical assessment of two approaches for evaluating contacts between super-quadric shaped particles in dem simulations. *Chemical Engineering Science*, 78:226–235, 2012.

[87] G. Lu, J. R. Third, and C. R. Müller. Discrete element models for non-spherical particle systems: From theoretical developments to applications. *Chemical Engineering Science*, 127:425–465, 2015.

[88] Liqiang Lu, Xi Gao, Jean-François Dietiker, Mehrdad Shahnam, and William A. Rogers. Machine learning accelerated discrete element modeling of granular flows. *Chemical Engineering Science*, 245:116832, 2021.

[89] S. Luding, J. Duran, E. Clément, and J. Rajchenbach. Computer simulations and experiments of dry granular media: Polydisperse disks in a vertical pipe. In *Proc. of the 5th Chemical Engineering World Congress*, San Diego, 1996. AIChE.

[90] Stefan Luding. Cohesive, frictional powders: contact models for tension. *Granular matter*, 10(4):235–246, 2008.

[91] G. Lumay and N. Vandewalle. Compaction of anisotropic granular materials: experiments and simulations. *Phys Rev E Stat Nonlin Soft Matter Phys*, 70(5 Pt 1):051314, Nov 2004.

[92] Chunhui Ma, Jie Yang, Gerald Zenz, Edwin Josef Staudacher, and Lin Cheng. Calibration of the microparameters of the discrete element method using a relevance vector machine and its application to rockfill materials. *Advances in Engineering Software*, 147:102833, 2020.

[93] Gang Ma, Jiangzhou Mei, Ke Gao, Jidong Zhao, Wei Zhou, and Di Wang. Machine learning bridges microslips and slip avalanches of sheared granular gouges. *Earth and Planetary Science Letters*, 579:117366, 2022.

[94] Sandip Mandal, Maxime Nicolas, and Olivier Pouliquen. Rheology of cohesive granular media: Shear banding, hysteresis, and nonlocal effects. *Phys. Rev. X*, 11:021017, Apr 2021.

[95] S. McNamara and W. R. Young. Inelastic collapse in two dimensions. *Phys. Rev. E*, 50(1):R28–R31, 1994.

[96] J. J. Moreau. Bounded variation in time. In P.D. Panagiotopoulos and G Strang, editors, *Topics in Nonsmooth Mechanics*, pages 1–74. Bikhäuser, Basel, 1988.

[97] J.J. Moreau. *Unilateral contact and dry friction in finite freedom dynamics*, volume 302 of *International Centre for Mechanical Sciences, Courses and Lectures*. Springer, Vienna, 1988.

[98] J.J. Moreau. Some numerical methods in multibody dynamics : application to granular. *European J. Mech. A Solids*, 13:93–114, 1994.

[99] R Moreno-Atanasio, BH Xu, and M Ghadiri. Computer simulation of the effect of contact stiffness and adhesion on the fluidization behaviour of powders. *Chemical engineering science*, 62(1-2):184–194, 2007.

[100] R. Moreno-Atanasio, B.H. Xu, and M. Ghadiri. Computer simulation of the effect of contact stiffness and adhesion on the fluidization behaviour of powders. *Chemical Engineering Science*, 62(1):184–194, 2007. Fluidized Bed Applications.

[101] Patrick Mutabaruka, Mahdi Taiebat, Roland J.-M. Pellenq, and Farhang Radjai. Effects of size polydispersity on random close-packed configurations of spherical particles. *Phys. Rev. E*, 100:042906, Oct 2019.

[102] Wenguang Nan, Wei Pin Goh, and Mohammad Tarequr Rahman. Elasto-plastic and adhesive contact: An improved linear model and its application. *Powder Technology*, 407:117634, 2022.

[103] Saeid Nezamabadi, Farhang Radjai, Julien Averseng, and Jean-Yves Delenne. Implicit frictional-contact model for soft particle systems. *Journal of the Mechanics and Physics of Solids*, 83:72–87, 2015.

[104] Duc-Hanh Nguyen, Emilien Azéma, Farhang Radjai, and Philippe Sornay. Effect of size polydispersity versus particle shape in dense granular media. *Physical Review E*, 90(1):012202, 2014.

[105] Duc-Hanh Nguyen, Émilien Azéma, Philippe Sornay, and Farhang Radjaï. Rheology of granular materials composed of crushable particles. *The European Physical Journal E*, 41(4):50, 2018.

[106] William L. Oberkampf and Christopher J. Roy. *Verification and validation in scientific computing*. Cambridge University Press, 2010.

[107] Luisa Fernanda Orozco, Jean-Yves Delenne, Philippe Sornay, and Farhang Radjai. Discrete-element model for dynamic fracture of a single particle. *International Journal of Solids and Structures*, 166:47–56, 2019.

[108] Luisa Fernanda Orozco, Jean-Yves Delenne, Philippe Sornay, and Farhang Radjai. Rheology and scaling behavior of cascading granular flows in rotating drums. *Journal of Rheology*, 64(4):915–931, 07 2020.

[109] Eun Hyun Park, Volodymyr Kindratenko, and Youssef M. A. Hashash. Shared memory parallelization for high-fidelity large-scale 3d polyhedral particle simulations. *Computers and Geotechnics*, 137:104008, 2021.

[110] Massih Pasha, Selasi Dogbe, Colin Hare, Ali Hassanpour, and Mojtaba Ghadiri. A linear model of elasto-plastic and adhesive contact deformation. *Granular Matter*, 16:151–162, 2014.

[111] Bo NJ Persson and Mations Scaraggi. Theory of adhesion: Role of surface roughness. *The Journal of chemical physics*, 141(12):124701, 2014.

[112] Pierre-Emmanuel Peyneau and Jean-Noel Roux. Frictionless bead packs have macroscopic friction, but no dilatancy. *Physical Review E*, 78, 2008.

[113] Weria Pezeshkian and Siewert J. Marrink. Simulating realistic membrane shapes. *Current Opinion in Cell Biology*, 71:103–111, 2021.

[114] T. Pöschel and V. Buchholtz. Static friction phenomena in granular materials: Coulomb law vs. particle geometry. *Phys. Rev. Lett.*, 71(24):3963, 1993.

[115] Dmitry Puzyrev, Kirsten Harth, Torsten Trittel, and Ralf Stannarius. Machine learning for 3d particle tracking in granular gases. *Microgravity Science and Technology*, 32(5):897–906, 2020.

[116] Juan Carlos Quezada, Pierre Breul, Gilles Saussine, and Farhang Radjai. Stability, deformation, and variability of granular fills composed of polyhedral particles. *Phys. Rev. E*, 86:031308, Sep 2012.

[117] Juan Carlos Quezada, Pierre Breul, Gilles Saussine, and Farhang Radjai. Penetration test in coarse granular material using contact dynamics method. *Computers and Geotechnics*, 55:248–253, 2014.

[118] Radjai and Roux. Friction-induced self-organization of a one-dimensional array of particles. *Phys. Rev. E*, 51(6):6177–6187, Jun 1995.

[119] F. Radjai, L. Brendel, and S. Roux. Nonsmoothness, indeterminacy, and friction in two- dimensional arrays of rigid particle. *Phys. Rev. E*, 54(1):861, 1996.

[120] F. Radjai and F. Dubois. *Discrete-element modeling of granular materials*. ISTE, 2011.

[121] F. Radjai and V. Richefeu. Contact dynamics as a nonsmooth discrete element method. *Mechanics of Materials*, 41:715–728, 2009.

[122] F. Radjai, D. E. Wolf, M. Jean, and J.J. Moreau. Bimodal character of stress transmission in granular packings. *Phys. Rev. Letter*, 80:61–64, 1998.

[123] Mathieu Renouf and Pierre Alart. Conjugate gradient type algorithms for frictional multi-contact problems: applications to granular materials. *Computer Methods in Applied Mechanics and Engineering*, 194(18-20):2019–2041, May 2005.

[124] Vincent Richefeu, Moulay Saïd El Youssoufi, and Farhang Radjai. Shear strength properties of wet granular materials. *Phys. Rev. E*, 73(5 Pt 1):051304, May 2006.

[125] Vincent Richefeu, Moulay Said El Youssoufi, Emilien Azéma, and Farhang Radjai. Force transmission in dry and wet granular media. *Powder Technology*, 190:258–263, 2009.

[126] Vincent Richefeu, Guilhem Mollon, Dominique Daudon, and Pascal Villard. Dissipative contacts and realistic block shapes for modeling rock avalanches. *Engineering Geology*, 149-150:78–92, 2012.

[127] Christopher J. Roy and William L. Oberkampf. A comprehensive framework for verification, validation, and uncertainty quantification in scientific computing. *Computer Methods in Applied Mechanics and Engineering*, 200(25):2131–2144, 2011.

[128] J. Schäfer, S. Dippel, and D. E. Wolf. Force schemes in simulations of granular materials. *J. Phys. I France*, 6:5–20, 1996.

[129] Thomas Schwager and Thorsten Pöschel. Coefficient of restitution and linear-dashpot model revisited. *Granular Matter*, 9(6):465–469, 2007.

[130] Daniel Shiffman. *The Nature of Code: Simulating Natural Systems with Processing*. Daniel Shiffman, 2012.

[131] I. M. Sobol. Global sensitivity indices for nonlinear mathematical models and their monte carlo estimates. *Mathematics and Computers in Simulation*, 55(1):271–280, 2001.

[132] L. Staron, J.-P. Vilotte, and F. Radjai. Preavalanche instabilities in a granular pile. *Phys. Rev. Lett.*, 89:204302, 2002.

[133] Alfredo Taboada, Nicolas Estrada, and Farhang Radjaï. Additive decomposition of shear strength in cohesive granular media from grain-scale interactions. *Phys. Rev. Lett.*, 97(9):098302, Sep 2006.

[134] Josef Tausendschön, Jari Kolehmainen, Sankaran Sundaresan, and Stefan Radl. Coarse graining euler-lagrange simulations of cohesive particle fluidization. *Powder Technology*, 364:167–182, 2020.

[135] Luís Marcelo Tavares. Review and further validation of a practical single-particle breakage model:. *KONA Powder and Particle Journal*, 39:62–83, 2022.

[136] Subhash C Thakur, John P Morrissey, Jin Sun, JF Chen, and Jin Y Ooi. Micromechanical analysis of cohesive granular materials using the discrete element method with an adhesive elasto-plastic contact model. *Granular Matter*, 16:383–400, 2014.

[137] C. Thornton and C. W. Randall. Applications of theoretical contact mechanics to solid particle system simulation. In *Micromechanics of granular media*, Amsterdam, 1988. Elsevier.

[138] Colin Thornton, Sharen J Cummins, and Paul W Cleary. An investigation of the comparative behaviour of alternative contact force models during inelastic collisions. *Powder technology*, 233:30–46, 2013.

[139] V. Topin, J-Y. Delenne, F. Radjai, L. Brendel, and F. Mabille. Strength and failure of cemented granular matter. *Eur. Phys. J. E*, 23(4):413–429, Aug 2007.

[140] V. Topin, J.-Y. Delenne, F. Radjai, L. Brendel, and F. Mabille. Strength and fracture of cemented granular matter. *The European Physical Journal E*, 23:413–429, 2007.

[141] Vincent Topin, Farhang Radjai, Jean-Yves Delenne, Abdelkrim Sadoudi, and Frédéric Mabille. Wheat endosperm as a cohesive granular material. *Journal of Cereal Science*, 47(2):347–356, March 2008.

[142] S. Torquato. Nearest-neighbor statistics for packings of hard spheres and disks. *Phys. Rev. E*, 51:3170, 1995.

[143] Joost H. van der Linden, Guillermo A. Narsilio, and Antoinette Tordesillas. Machine learning framework for analysis of transport through complex networks in porous, granular media: A focus on permeability. *PRE*, 94(2):022904, August 2016.

[144] Jan G. M. VanMier, Marcel R. A. van Vliet, and Tai K. Wang. Fracture mechanisms in particle composites: statistical aspects in lattice type analysis. *Mechanics of Materials*, 34(11):705–724, November 2002.

[145] C. Voivret, F. Radjaï, J-Y. Delenne, and M. S. El Youssoufi. Space-filling properties of polydisperse granular media. *Phys Rev E Stat Nonlin Soft Matter Phys*, 76(2 Pt 1):021301, Aug 2007.

[146] C. Voivret, F. Radjai, J.-Y. Delenne, and M.S. El Youssoufi. Force transmission in polydisperse granular media. *Phys. Rev. Lett.*, 102:178001, 2009.

[147] Xiang Wang, Zhen-Yu Yin, Hao Xiong, Dong Su, and Yun-Tian Feng. A spherical-harmonic-based approach to discrete element modeling of 3d irregular particles. *Int J Numer Methods Eng*, 122(20):5626–5655, October 2021.

[148] Eric Winsberg. Computer Simulations in Science. In Edward N. Zalta and Uri Nodelman, editors, *The Stanford Encyclopedia of Philosophy*. Metaphysics Research Lab, Stanford University, Winter 2022 edition, 2022.

[149] Lingfei Wu, Peng Cui, Jian Pei, and Liang Zhao. *Graph Neural Networks: Foundations, Frontiers, and Applications*. Springer Singapore, Singapore, 2022.

[150] Mingqiu Wu, Stefan Radl, and Johannes G. Khinast. A model to predict liquid bridge formation between wet particles based on direct numerical simulations. *AIChE Journal*, 62(6):1877–1897, 2016.

[151] Z. Yan, S. K. Wilkinson, E. H. Stitt, and M. Marigo. Discrete element modelling (dem) input parameters: understanding their impact on model predictions using statistical analysis. *Computational Particle Mechanics*, 2(3):283–299, 2015.

[152] Dangfu Yang, Xiang Wang, Haoran Zhang, Zhen-yu Yin, Dong Su, and Jun Xu. A mask r-cnn based particle identification for quantitative shape evaluation of granular materials. *Powder Technology*, 392:296–305, 2021.

[153] Yonghao Yue, Breannan Smith, Peter Yichen Chen, Maytee Chantharayukhonthorn, Ken Kamrin, and Eitan Grinspun. Hybrid grains: Adaptive coupling of discrete and continuum simulations of granular media. *ACM Trans. Graph.*, 37(6), dec 2018.

[154] Yonghao Yue, Breannan Smith, Peter Yichen Chen, Maytee Chantharayukhonthorn, Ken Kamrin, and Eitan Grinspun. Hybrid grains: Adaptive coupling of discrete and continuum simulations of granular media. *ACM Transactions on Graphics (TOG)*, 37(6):1–19, 2018.

[155] Pin Zhang and Zhen-Yu Yin. A novel deep learning-based modelling strategy from image of particles to mechanical properties for granular materials with cnn and bilstm. *Computer Methods in Applied Mechanics and Engineering*, 382:113858, 2021.

[156] Tao Zhang, Chi Zhang, Jiuqun Zou, Baosheng Wang, Fangnian Song, and Weihao Yang. Dem exploration of the effect of particle shape on particle breakage in granular assemblies. *Computers and Geotechnics*, 122:103542, 2020.

[157] Yibo Zhang, Wei Zhou, Gang Ma, Ruilin Cheng, and Xiaolin Chang. The structure-property relationship of granular materials with different friction coefficients: Insight from machine learning. *Extreme Mechanics Letters*, 54:101759, 2022.

[158] Shiwei Zhao and Jidong Zhao. A poly-superellipsoid-based approach on particle morphology for dem modeling of granular media. *Int J Numer Anal Methods Geomech*, 43(13):2147–2169, September 2019.

[159] Chao Zheng, Nicolin Govender, Ling Zhang, and Chuan-Yu Wu. Gpu-enhanced dem analysis of flow behaviour of irregularly shaped particles in a full-scale twin screw granulator. *Particuology*, 61:30–40, 2022.

[160] Fan Zhu and Jidong Zhao. Modeling continuous grain crushing in granular media: A hybrid peridynamics and physics engine approach. *Computer Methods in Applied Mechanics and Engineering*, 348:334–355, 2019.